

ABSTRACT

Title of Dissertation: RELAXATION TIME FLUCTUATIONS IN
TRANSMONS WITH DIFFERENT
SUPERCONDUCTING GAPS
Kungang Li, Doctor of Philosophy, 2023

Dissertation directed by: Professor Christopher J. Lobb
Department of Physics

Professor Frederick C. Wellstood
Department of Physics

In this thesis, I discuss the fabrication and measurement of Al/AIO_x/Al transmons that have electrodes with different superconducting gaps. With gap-engineering, the tunneling of single quasiparticle from the low-gap side to the high-gap side can be suppressed, hence increasing the relaxation time T_1 . The best gap-engineered device showed T_1 exceeding 300 μ s. Large T_1 fluctuations in my devices were also observed. I proposed a mechanism for exploring the T_1 fluctuation data and discuss the possible underlying cause of the T_1 fluctuations.

I first discuss the theory of the loss in gap-engineered transmons, with a focus on the loss from non-equilibrium quasiparticles. The model yields the quasiparticle-induced loss in transmons

and its dependence on temperature. I also discuss how multiple Andreev reflection (MAR) effects might alter these conclusions, leading to a further reduction in T_1 .

I then describe the design, fabrication and basic characterization of the transmon chip SKD102, which features two transmons – one with thin-film electrodes of pure Al and another that had one electrode made from oxygen-doped Al. I next examined T_1 vs temperature and how the T_1 fluctuations depended on temperature. I compare my results to a simple model and find reasonable agreement in transmons on chip SKD102, KL103 and KL109, which had different electrode and layer configurations.

Finally, I analyze T_1 fluctuations in different devices and as a function of temperature and propose a model to explain this behavior. Over the different devices, the T_1 fluctuation magnitude roughly scaled as $T_1^{3/2}$. With increasing temperature, T_1 decreases due to a higher density of thermally generated quasiparticles. In contrast, for an individual device measured from 20mK to 250 mK, the fluctuation magnitude appears to be proportional to T_1 . I present a model of quasiparticle dissipation channels that reproduces both of these observed scaling relationships.

RELAXATION TIME FLUCTUATIONS IN TRANSMONS WITH
DIFFERENT SUPERCONDUCTING GAPS

by

Kungang Li

Dissertation submitted to the Faculty of the Graduate School of the
University of Maryland, College Park, in partial fulfillment
of the requirements for the degree of
Doctor of Philosophy
2023

Advisory Committee:

Professor Christopher J. Lobb, Chair / Co-Advisor

Professor Frederick C. Wellstood, Co-Advisor

Dr. Benjamin S. Palmer

Professor Steven M. Anlage

Professor John Cumings, Dean's Representative

© Copyright by
Kungang Li
2023

Dedication

Dedicated to my grandfather and my uncle.

Acknowledgement

Completing PhD during the pandemic was not easy. When the lab shut down three years ago, I didn't know if I could finish my studies and research at school. Fortunately, with support from my group and the school, our laboratory gradually returned to normal operations. Throughout my PhD journey at UMD, I gained more than I had ever anticipated. This remarkable experience transformed me from a novice in quantum computing into a researcher with tangible contributions. I couldn't have done it without help from many people, and I take this moment to humbly extend my deepest gratitude to each of them.

Foremost, I express my appreciation to my advisors, Prof. Christopher Lobb and Prof. Fred Wellstood. I wish to extend special thanks to Prof. Lobb for having me as his last student and for his exceptional mentorship. His unique insights into complex problems consistently provided me with invaluable guidance, and I always felt both inspired and enlightened. I am also grateful for his consistent provision of valuable advice and praise for my work, which has been a tremendous source of motivation and encouragement. I am immensely grateful to Prof. Wellstood for his excellence as a scientist and mentor. Our discussions always led to problem resolutions, and his patience in explaining intricate matters played an important role in my research. I deeply appreciate his comments on my papers and presentations. I want to thank Dr. Sudeep Dutta, who guided my research and provided extensive support throughout my PhD journey, played a critical role in ensuring the smooth operation of our laboratory, especially during the challenging times of the pandemic.

I extend my gratitude to Dr. Ben Palmer and his group, including Zach, Yi-Hsiang, Haozhi, Yizhou, and Rui, for their collaboration on various projects, insightful suggestions during group

meetings, and the use of facilities at LPS. The discussions with your group enriched my research experience significantly.

I would also like to acknowledge Prof. Steven Anlage for his service on my committee and for the opportunity to work as a Teaching Assistant during my first year. I want to thank Prof. Sarah Eno for the guidance when I was working as a Teaching Assistant for her as well. Furthermore, I am thankful to Prof. John Cumings for agreeing to serve as the Dean's representative on my committee.

My appreciation extends to the numerous individuals within the Physics Department and IPST. To Yingyue, Sungha, En-Rui, Yijia, Zhiyu, Druvit, Yi-mu, Kaixin, Shuyang, Pei-yin, and Kee, I am grateful for the countless academic and non-academic conversations. Our interactions not only enriched my academic knowledge but also provided support during challenging moments, especially during the lockdown. I want to thank Dr. Wan-Ting Liao for being an exceptional mentor and friend throughout my PhD journey. I am grateful for your invitation to your home in Boston and the invaluable guidance for PhD research. (Special thanks to Karl as well!) My appreciation also goes out to Long, Hanho, Nitish, Ray, Shukai, and Haonan from Prof. Manucharyan's group for their invaluable advice, particularly Haonan for patiently addressing my numerous questions during the first year of my PhD study. I would like to express my gratitude to Chung-Yang, Jingnan, Jerry, and Seokjin from Prof. Anlage's group for their constant support and greetings, as your lab was the closest to mine, making me feel less isolated. I extend my thanks to Martin, Maya, Zhiyin, and Kellen from Prof. Alicia's group for hosting the journal clubs and I benefitted a lot from the discussion.

I am grateful to the individuals responsible for maintaining the facilities: Dough, Brian, and Kurtis, who promptly addressed any issues and taught me how to operate AFM and PPMS;

John, Jon, Mark, and others at Fablab who guided me in using lithography and other equipment; and Wen-An for the informative short courses on SEM operation. I also want to thank

My appreciation also goes out to my friends: Jiawen, Shuang, Wei, Chuchu, Drolkar, Yucheng, and Yongle, who have been my pillars of support throughout these years. Your unwavering emotional support has been invaluable. I extend my heartfelt thanks to Brendan for his support and invaluable advice whenever I felt discouraged from work, especially in the final stages of completing my thesis. I would like to express my gratitude to Carol for being a wonderful landlord and for her support. I also experienced a significant shoulder fracture that rendered me unable to perform lab work for several months. I am immensely grateful to my advisors, friends, and family for their care and support, which allowed me to recover quickly. There are many more individuals I encountered during my time in Maryland, and I am deeply thankful to each of them, even if their names are not mentioned here.

Finally, I reserve my deepest gratitude for my parents and my entire family. While the pandemic prevented me from visiting them, they remained my unwavering source of strength. I am thankful for their support in my pursuit of doctoral degree in physics, and for their unshakable belief in me.

Table of Contents

Dedication	ii
Acknowledgement	iii
List of Tables	x
List of Figures	xi
Chapter 1 Introduction.....	1
1.1 Quantum Computing.....	1
1.2 Superconducting Qubits.....	2
1.3 Overview of Dissertation	3
Chapter 2 Theory of Transmons	5
2.1 Quantum Harmonic LC-Resonator	5
2.2 Josephson Junction.....	6
2.3 Cooper Pair Box.....	9
2.4 Transmon Qubit	12
2.5 Circuit QED System	14
2.6 Energy Relaxation and Dissipation Mechanisms	18
2.7 Dephasing Time T_ϕ	23
2.8 Coherence Time T_2	27

Chapter 3	The Superconducting Energy Gap Δ and Granular Aluminum	
	Thin Films	28
3.1	BSC Theory and Superconducting Gaps	28
3.2	Granular Aluminum Thin Films	35
Chapter 4	Theory of Quasiparticle Behavior in Junctions that Have	
	Different Gaps	38
4.1	Quasiparticles	38
4.2	Quasiparticle Relaxation and Excitation with Regions that Have Different Gaps	41
4.3	Modeling Quasiparticle Density	48
4.4	Andreev Reflection	53
Chapter 5	Transmons Design and Fabrication	72
5.1	Transmon Design	72
5.2	Cavity Design.....	76
5.3	Transmon Fabrication	76
5.4	Lift-off Procedure	84
5.5	Tunnel Junction Resistance Measurement.....	89
5.6	Oxygen Doping Tests on Al Films	89

Chapter 6	Experimental Setup.....	93
6.1	The Dilution Refrigerator Setup	93
6.2	Input and Output Microwave Lines	95
6.3	Room Temperature Electronics Setup	98
Chapter 7	Characterization of Two Transmons	102
7.1	Measurement Details	102
7.2	Cavity Characterization	104
7.3	Qubit Spectroscopy	107
7.4	Rabi Oscillations	108
7.5	Relaxation Time T_1	110
7.6	Spin Echo T_2	113
7.7	Ramsey Oscillations.....	115
7.8	Summary of Measured Parameters of the Devices	118
Chapter 8	Transmons with Gap-Engineered Electrodes:	
	T_1 Measurements and Other Results.....	120
8.1	Comparison of Low-Gap High-Gap Transmon and an Undoped Al Transmon.....	121
8.2	Temperature Dependence of T_1 for Low-Gap High-Gap Device and Nominal Al Device	122
8.3	Fabrication and Measurements of High-Gap Low-Gap Transmons	126
8.4	Fabrication and Measurements of Transmons with Trapping Layer	128

8.5 Charge Dispersion and T_1	133
8.6 Summary of All the Gap-Engineered Devices and Conclusion.....	138
Chapter 9 Analysis of Relaxation Time Fluctuations	143
9.1 T_1 Fluctuation Data	144
9.2 Model for Fluctuations in Quasiparticle Dissipation Channels	146
9.3 Ruling Out Other Sources of Fluctuations	150
9.4 Conclusion	153
Chapter 10 Conclusions	154
Bibliography.....	157

List of Tables

Table 4.1: Andreev tunneling processes.

Table 4.2: Unity Source Recursion relations for finding the electron and hole wave amplitudes.

Table 7.1: Summary of the measured parameters of transmons Q_{L1} and Q_{R1} on chip SKD102.

Table 8.1: Parameters of the transmons.

List of Figures

Figure 2.1: Illustration of an S-I-S Josephson junction.

Figure 2.2: Circuit diagram of a Cooper-Pair Box.

Figure 2.3: The first three energy levels of the cooper-pair box as a function of $n\phi$.

Figure 2.4: Circuit diagram of an isolated transmon.

Figure 2.5: Geometrical representation of Bloch Sphere.

Figure 3.1: AFM scan of 70 nm thick granular Al film showing rough surface.

Figure 4.1: Schematic view of the Al/AlO_x/Al Josephson junction.

Figure 4.2: The process of Andreev reflection.

Figure 4.3: Illustration of Andreev reflections process that occur in a model of an S-I-S tunnel junction.

Figure 4.4: I-V curve for Andreev reflection in semi-log scale.

Figure 5.1: CAD drawing of the chip design.

Figure 5.2: CAD drawing of transmon pads and the Josephson junction.

Figure 5.3: Picture of Al cavity SI-2a.

Figure 5.4: An optical photograph of the e-beam resist layers of the junction area after the development process.

Figure 5.5: Photograph of the thermal evaporator.

Figure 5.6: Double-angle evaporation fabrication procedure for building two transmons with different layer configurations on the same chip in the same pump down.

Figure 5.7: Images of chip holder and mechanical mask.

Figure 5.8: Evaporation setup inside the evaporator.

Figure 5.9: SEM and optical micrographs showing transmon junction formed using double-angle evaporation of Al.

Figure 5.10: Plot of measured film critical temperature T_C versus O_2 gas doping pressure P_{O_2} .

Figure 5.11: Plot showing measured film residual-resistance ratio RRR versus T_C .

Figure 6.1: Picture of Oxford Triton 200 dilution refrigerator.

Figure 6.2: Pictures of μ -metal and Inner A4K magnetic shields.

Figure 6.3: Schematic of refrigerator stages showing components on the input and output microwave lines.

Figure 6.4: Room temperature microwave setup for qubit measurements.

Figure 6.5: Photograph of rack with microwave pulse control and qubit readout setup.

Figure 7.1: General applied pulse sequence for qubit manipulation and state measurements.

Figure 7.2: Cavity power map $|S_{21}|^2$ of chip SKD102 in cavity SI-2a.

Figure 7.3: Line cuts through plot in Fig. 7.2 showing $|S_{21}|^2$ as a function of frequency for four applied powers P_c .

Figure 7.4: Qubit spectroscopy of the gap-engineered transmon Q_{L1} and the nominally standard transmon Q_{R1} at high qubit drive powers.

Figure 7.5: Pulse sequence for Rabi Oscillation measurements.

Figure 7.6: Rabi Oscillation decay measurements for transmons Q_{L1} and Q_{R1} with 250 kHz Rabi frequency.

Figure 7.7: Applied pulse sequence for relaxation time T_1 measurements.

Figure 7.8: Relaxation measurements for transmons Q_{L1} and Q_{R1} fit to exponential decay.

Figure 7.9: Applied pulse sequence for spin echo T_2 measurements.

Figure 7.10: Spin echo measurements for transmons Q_{L1} and Q_{R1} on chip SKD102.

Figure 7.11: Pulse sequence for Ramsey Oscillation measurements.

Figure 7.12: Measurement of the excited state population $P_{|e\rangle}$ versus Ramsey delay time Δt of Q_{R1} .

Figure 7.13: Ramsey fringe measurement results of Q_{R1} .

Figure 8.1: The T_1 vs time t measurement for transmons Q_{L1} and Q_{R1} on chip SKD102.

Figure 8.2: The T_1 vs temperature T measurement for transmons Q_{L1} and Q_{R1} on chip SKD102.

Figure 8.3: Plot of T_1 vs T for transmons Q_{L1} with fitting parameters $\Delta_1 = 225.3 \mu\text{eV}$ and

$$\Delta_2 = 230.90 \mu\text{eV} \text{ and } Q_{R1} \text{ with fitting parameters } \Delta_1 = 190.5 \mu\text{eV} \text{ and } \Delta_3 = 179.6 \mu\text{eV}.$$

Figure 8.4: Fabrication procedure for building two transmons on chip KL103.

Figure 8.5: T_1 vs time t data for the gap-engineered transmons Q_{L2} and Q_{R2} .

Figure 8.6: Fabrication procedure for building Q_{L3} and Q_{R3} on chip KL109.

Figure 8.7: SEM image of Q_{L3} junction area with triple layer structure on chip KL109.

Figure 8.8: T_1 vs time t measurements for transmons Q_{L3} and Q_{R3} with a trapping layer.

Figure 8.9: Repeated measurement of charge dispersion spectrum in transmon Q_{R3} .

Figure 8.10: The general process of getting state lifetime from delay spectrum.

Figure 8.11: Delayed spectroscopy measurement of transmon Q_{R3} versus the 2-photon transition frequency.

Figure 8.12: State lifetime measurement of $|f\rangle$ state and $|e\rangle$ state over the $|g\rangle - |f\rangle$ dispersive frequencies.

Figure 8.13: The maximum T_1 vs transmon frequency of the devices in Table 8.1.

Figure 9.1: Semi-log plots of relaxation time T_1 vs temperature T and σ_{T_1} vs T_1 for gap-engineered transmon Q_{L1} and standard transmon Q_{R1} .

Figure 9.2: Plot of σ_{T_1} vs T_1 for different transmons at the base temperature of 20 mK.

Chapter 1

Introduction

1.1 Quantum Computing

The concept of quantum computing can be traced back to the 1980s, when Richard Feynman, Paul Benioff, and Yuri Manin proposed the idea of a fully quantum model for computation. Physicist Paul Benioff pioneered the concept of quantum computing in 1980 in a paper on quantum mechanical model of the Turing machine [1]. This demonstrated reversible computing [2] was possible via the Schrödinger equation. Yuri Manin and Richard Feynman did additional research to show how a quantum computer could perform better than a classical computer for certain types of calculations [3][4]. As research into quantum computing progressed, Kazuhiro Igeta and Yoshihisa Yamamoto proposed using atoms and photons as a physical platform for building a quantum computer [5]. Their proposal sparked a frenzy of experimental activity as researchers began to investigate many possible types of qubits and the feasibility of building a working quantum computer.

In the 1990s, David Deutsch and Richard Jozsa proposed a deterministic quantum algorithm that could efficiently solve a particular computational problem that no deterministic classical algorithm could solve efficiently. They were able to demonstrate the superiority of a quantum computer over a classical computer [6]. Peter Shor's quantum algorithm [7] for prime factorization of integers was also developed in 1994, sparking a surge of interest in building physical realizations of quantum computers.

Since this early work, trapped ion [8][9], quantum dot [10], superconducting [11][12], and linear optical qubits [13], have been developed with relatively high-fidelity control and quantum error correction. Despite these and many other technological advances over the last two decades, there are still many challenges to overcome before large-scale quantum computers can be built. One of the most significant challenges is developing fault-tolerant quantum systems capable of correcting errors caused by decoherence and noise [14]-[17]. The potential of quantum computing to solve problems that are currently intractable for classical computers makes it an exciting field of research. Quantum computing has the potential to revolutionize fields such as cryptography [18], drug discovery [19], and materials science [20], and may have a significant impact on our society in the coming years.

1.2 Superconducting Qubits

A qubit is a fundamental unit of quantum information that is the quantum analog of a classical binary bit, in which information is stored in the quantum state of the system. I will also use “qubit” to define a two-level system that contains this information. While a classical bit can only be in one of two states, either 0 or 1, a qubit can be in a superposition of states, representing both 0 and 1. In addition, the state of a qubit can be entangled with the state of other qubits. Because of these quantum properties of qubits, quantum computers can perform certain types of calculations much faster than classical computers.

The coherence time of a qubit measures the lifetime of the logic state and serves as a metric for completing logic operations. Decoherence is due to two causes: energy relaxation and dephasing, which are ultimately caused by entanglement between the qubit and its environment. This entanglement causes information in the qubit to be lost to the environment [21][22].

The field of coherent quantum effects in superconducting devices began in the 1980s with the discovery of macroscopic quantum tunneling [23][24] and quantum energy levels in Josephson devices [25]. This work continued with the development of single-electron devices [26] and the Cooper-pair box [27], and the search for macroscopic quantum coherent oscillations in the rf superconducting quantum interference device (rf SQUID) [28][29]. The superconducting quantum computation began when the Cooper-pair box was shown by Nakamura *et al.* [11] to undergo coherent quantum oscillations. This served as the foundation for early superconducting qubits. However, charge qubits are sensitive to quasiparticles and charge noise, severely limiting the lifetime of the quantum states. Ultimately, this limitation was eventually overcome by making the electrostatic charging energy E_C much smaller than the Josephson energy E_J and by adding a low-loss shunting capacitance across the junction to effectively reduce loss due to the junction dielectric. This new device, called a transmon [30], achieved useful anharmonicity and was less sensitive to noise, making it a more practical option for superconducting quantum computing.

Superconducting qubits are currently among the leading candidates for building scalable quantum computers. They can be designed to have reasonably long coherence times and fast gate times and they can be produced in large quantities using standard lithographic techniques. Ongoing work to develop systems with 400 and more superconducting qubits has been reported [31] by IBM, indicating that progress toward building a practical large-scale quantum computer using superconducting qubits is being made.

1.3 Overview of Dissertation

The goal of my research is to fabricate transmon devices gap-engineered to suppress quasiparticle tunneling between the two electrodes of the junction thus enhance the relaxation time

T_1 . In this dissertation, I discuss the fabrication of gap-engineered transmons and how superconducting gap differences affect quasiparticle induced relaxation. The qubits I fabricated and measured were fixed frequency transmons. The transmons were mounted in 3D cavities to allow measurement of the qubit state and to provide isolation of the qubit from the environment. I also discuss fluctuations in the transmon relaxation time T_1 and propose a mechanism that may be the underlying cause of these fluctuations.

In Chapter 2, I introduce the quantum theory of the transmon and discuss the relaxation time T_1 . In chapter 3, I discuss the BCS theory and superconducting gaps of thin films. In Chapter 4, I explain modeling of quasiparticles induced loss in junctions that have two electrodes with different superconducting gaps. In Chapter 5, I describe the design and fabrication of the cavity and transmons. In Chapter 6, I illustrate the experimental setup I used to acquire data. My key experimental results are presented in the rest of the dissertation. Device characterization is discussed in Chapter 7. In Chapter 8, I go over the different transmon layouts I used and the corresponding relaxation time measurements. Chapter 9 demonstrates relaxation time fluctuations and a model of fluctuating dissipation channels which seems to capture some of the behaviors observed in the T_1 fluctuations. Finally, Chapter 10 summarizes the thesis and concludes with some suggestions for additional research.

Chapter 2

Theory of Transmons

In this chapter, I discuss the quantum behaviors of transmons and their applications to quantum computing. I begin with an overview of the Hamiltonian and the role of the Josephson junction - a critical component in transmon systems. I examine the energy levels and their anharmonicity, a key property of transmons. I then discuss energy relaxation and dephasing and conclude with a discussion of the parameters T_1 , T_2 , and T_ϕ .

2.1 Quantum Harmonic LC-Oscillator

The simple harmonic oscillator is one of the best-understood quantum systems in physics. This is very fortunate because a ground understanding of the quantum harmonic oscillator is helpful for understanding transmons circuit Quantum Electrodynamics (cQED) [1] and numerous other systems [2]. A simple harmonic LC-oscillator circuit can be built by connecting an inductor with inductance L across a capacitor with capacitance C . One can write the Hamiltonian for an isolated LC-oscillator as:

$$\hat{H} = \frac{\hat{Q}^2}{2C} + \frac{\hat{\Phi}^2}{2L}, \quad (2.1)$$

where \hat{Q} and $\hat{\Phi}$ are Hermitian operators for the charge on the capacitor and the flux in the inductor, respectively.

The non-Hermitian raising and lowering operators can be built as [3]:

$$\hat{a} = \sqrt{\frac{C\omega_r}{2\hbar}} \left(\hat{\Phi} + \frac{i\hat{Q}}{C\omega_r} \right) \quad (2.2a)$$

$$\hat{a}^\dagger = \sqrt{\frac{C\omega_r}{2\hbar}} \left(\hat{\Phi} - \frac{i\hat{Q}}{C\omega_r} \right), \quad (2.2b)$$

where \hat{a} is the annihilation operator, \hat{a}^\dagger is the creation operator, and $\omega_r = 1/\sqrt{LC}$ is the angular resonance frequency.

The Hamiltonian for the harmonic oscillator can then be written as:

$$\hat{H}_{QHO} = \hbar\omega_0 \left(\hat{a}^\dagger \hat{a} + \frac{1}{2} \right) = \hbar\omega_0 \left(\hat{\mathcal{N}} + \frac{1}{2} \right), \quad (2.3)$$

where $\hat{\mathcal{N}} = \hat{a}^\dagger \hat{a}$ is the photon number operator [3]. Eq. (2.3) is diagonal with eigenvalues $n=0, 1, 2, \dots$ and results in equally spaced energy levels by $\hbar\omega_0$.

If a non-linear inductor is incorporated into the LC-oscillator circuit, the system behaves like an artificial atom with unevenly spaced energy levels. Uneven level spacing is required to enable the manipulation of only two energy levels in a qubit while leaving other levels unaffected. Nonlinearity is accomplished for superconducting qubits by incorporating a Josephson junction [4], which functions as a nonlinear inductor within the circuit.

2.2 Josephson Junction

The concept of a Josephson junction (JJ) was first introduced by Brian D. Josephson in 1962 [5]. It is the essential building block of any type of superconducting qubits. One ideal for a Josephson junction is a trilayer structure that has two superconducting layers separated by a very thin insulating layer (see Fig. 2.1). For most superconducting qubits that are currently being used, the junction is made of Al/AlO_x/Al. This type of Josephson junction can be made relatively easily

and turns out to be relatively robust. Aluminum has a stable oxide layer (AlO_x). On the other hand, the superconducting transition temperature (T_c) of Al is about 1.2 K and the oxide layer can contain atomic-scale defects, called two-level systems or TLS, in the interfaces, that can be detrimental to the qubit lifetime.

Aluminum is not an obvious choice for building Josephson junctions because of its relatively low T_c . Despite having zero dc resistance at T_c , superconductors have non-zero ac losses. This is because the electrons in the superconductor are bound as Cooper pairs with a binding energy of $\Delta \cong 1.76k_B T_c$ [6]. At non-zero temperature, thermal energy can break some pairs, which generate “quasiparticles”. I provide some additional discussion of Cooper pairs and quasiparticles in Chapter 3. Quasiparticles also results in loss in a tunnel junction, which will be discussed in Chapter 4.

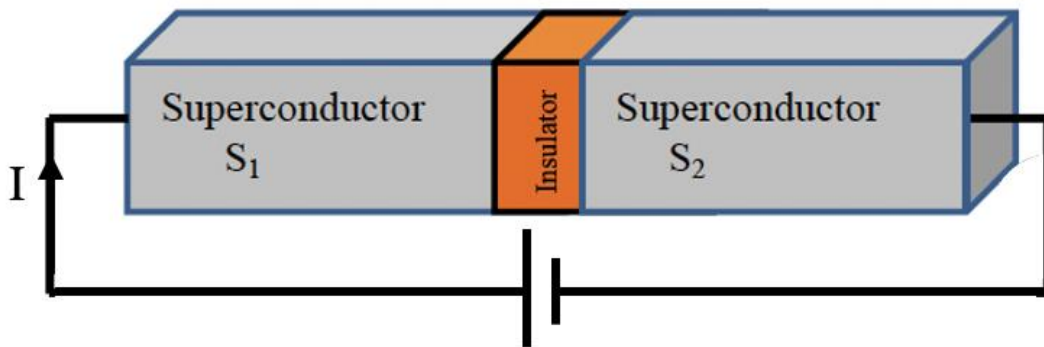


Figure 2.1: Illustration of an S-I-S Josephson junction formed by sandwiching a thin layer of insulation between two superconductors. The electrodes of the junction are connected to a voltage source V that drives current I through the junction.

The key electrical characteristic of a Josephson junction is the relationship between the phase difference ϕ across the junction, the junction current I , and the junction voltage V . They can be described by the Josephson equations [5]:

$$I = I_0 \sin \phi \quad (2.4a)$$

$$V = \phi_0 \frac{d\phi}{dt}, \quad (2.4b)$$

where $\phi_0 = \Phi_0/2\pi = \hbar/2e$ is the reduced flux quantum, Φ_0 is the flux quantum, and I_0 is the critical current. Combining Eqs. 2.4 (a) and 2.4 (b), I can write:

$$V = \frac{\phi_0}{I_0 \cos \phi} \frac{dI}{dt}. \quad (2.5)$$

This is similar to the current-voltage relation for an inductor $V = L_J * \frac{dI}{dt}$ and implies that the Josephson junction can be thought of as a non-linear inductor with inductance $L_J = \Phi_0/(2\pi I_0 \cos \phi)$.

An inductor that is carrying current I has a stored magnetic energy of $\frac{1}{2} LI^2$. Similarly, a Josephson junction with phase difference ϕ has a stored energy of $H_J = -E_J \cos \phi$, where $E_J = \Phi_0 I_0 / 2\pi$ is the Josephson energy. C_J is the capacitance between the two superconducting layers of the junction, there will also be a charging energy $H_C = 4E_C n^2$, where $n = \frac{Q}{2e}$ is the pair charge number and $E_C = e^2/(2C_J)$ is the charging energy of the junction. Connecting L_J and C_J in parallel gives us LC oscillator with angular resonant frequency:

$$\omega_p = \frac{1}{\sqrt{L_J C_J}} = \frac{1}{\hbar} \sqrt{8E_J E_C}. \quad (2.6)$$

For a Josephson junction, ω_p is called the plasma frequency and it is an important parameter. It can be shown that ω_p only depends on the transparency of the insulating layer to tunneling of pairs

and the dielectric constant but is independent of the junction area. For AlO_x insulation layers, the oxidation process is the most important factor in determining the transparency.

2.3 Cooper Pair Box

The Cooper-pair box (CPB) was the first experimentally realized superconducting qubit [7][8]. Figure 2.2 shows a circuit schematic of a CPB. A single Josephson junction J is connected in parallel to capacitance C_J . CPBs are typically biased with a gate voltage V_g , which is applied to a gate capacitance C_g and can be used to set the polarization charge on the island.

The Hamiltonian associated with a Cooper Pair Box (CPB) can be expressed as [8]

$$\hat{\mathcal{H}} = 4E_C(\hat{n} - n_g)^2 - E_J \cos \hat{\gamma}, \quad (2.7)$$

where \hat{n} is operator for excess number of Cooper pairs that tunnel onto the island, $n_g = -C_g V_g / 2e$ is the reduced gate charge, and $\hat{\gamma}$ is the operator for the superconducting phase difference across the Josephson junction. Here again E_J and E_C are the Josephson energy and the charging energy. Typically, Cooper-pair boxes have $E_J \ll E_C$. In this limit, the charge on the island serves as a sharply defined quantum number that is controlled by n_g . The operators \hat{n} and $\hat{\gamma}$ are conjugate variables and satisfy the commutation relation [3]:

$$[\hat{\gamma}, \hat{n}] = i. \quad (2.8)$$

The Hamiltonian equation (2.7) can also be expressed in the phase basis as [8]:

$$\mathcal{H}_{CPB} = 4E_C \left(-i \frac{\partial}{\partial \hat{\phi}} - n_g \right)^2 - E_J \cos \hat{\phi}. \quad (2.9)$$

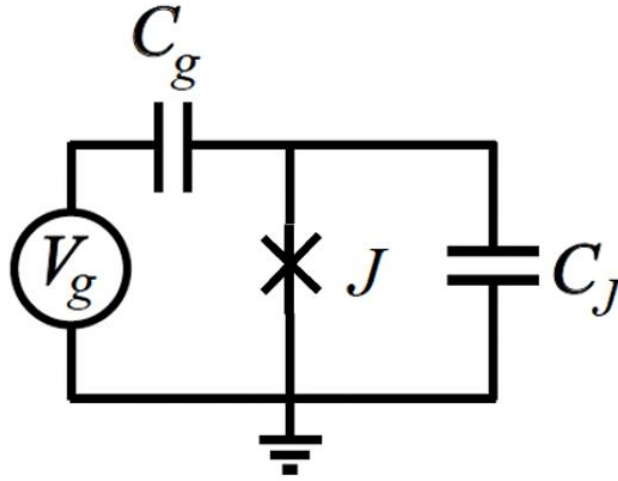


Figure 2.2: Circuit diagram of a Cooper-Pair Box

The exact solutions for the wavefunctions can be written in terms of the Mathieu functions and the energy eigenvalues are given by [9]:

$$E_m = E_C a_2[n_g + k(m, n_g)] \left(-\frac{E_J}{2E_C} \right), \quad (2.10)$$

where $m = 0, 1, 2, \dots, a_r(q)$ is the characteristic value for even Mathieu functions with characteristic exponent $r=2$ and parameter $q = n_g + k(m, n_g)$, and $k(m, n_g)$ is an integer-valued function that specifies the order of the eigenvalues. The ground and excited states of the CPB with energy E_0 and E_1 , respectively, determine the qubit transition energy.

Figure 2.3 shows E_m for $m = 0, 1, 2$ and 3 for different values of E_J/E_C , corresponding to the states $|g\rangle, |e\rangle, |f\rangle$ and $|h\rangle$ of the qubit. For the Cooper-pair box regime $E_J/E_C \ll 1$, the E_m curves depend strongly on n_g , while for $E_J/E_C \gg 1$, which is the phase qubit limit [10], the E_m are almost independent of n_g . CPB qubits are normally operated [11] at $n_g = \pm 0.5$, where E_{01} is

minimum. This operating point is commonly called the "sweet spot", because E_{01} is least affected by small fluctuations in n_g , protecting the qubit from small levels of charge noise. However, the charge noise in the CPB turned out to be so large that the coherence time was quite short, even at the sweet spot. For this reason (charge noise) the CPB is no longer considered a viable qubit candidate. This was one of the main motivations for the design of the transmon, which was proposed by Koch *et al.* [12].

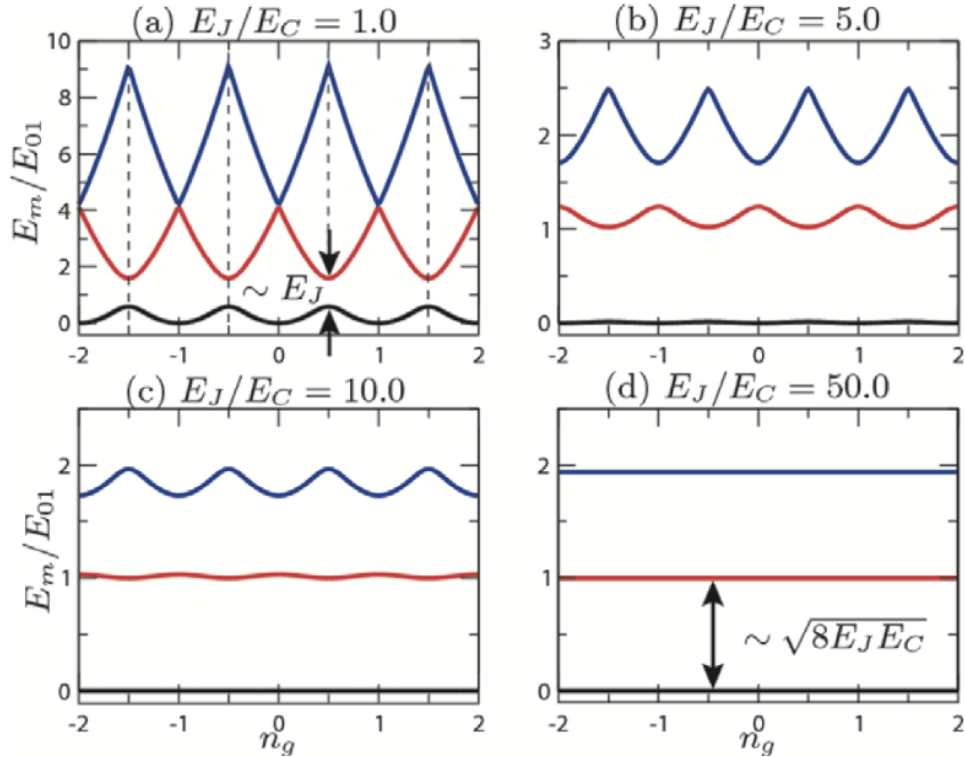


Figure 2.3: The first three energy levels of the cooper-pair box as a function of n_g , plotted for different values of E_J/E_C [13]. For all plots, the black curve corresponds to E_0 , the red curve corresponds to E_1 and the blue curve corresponds to E_2 .

2.4 Transmon Qubit

The transmon regime corresponds to $E_J \gg E_C$, which typically $E_J = 50 E_C$. In this limit, E_{01} is almost independent of n_g . To reduce loss from the junction dielectric, this limit is typically achieved by adding a low-loss shunting capacitor C_x parallel to the junction. This reduces E_C and improves T_1 (see Fig. 2.4).

I note that the Hamiltonian for the transmon is identical to that of a CPB or an un-biased phase qubit, the only difference between them is the E_J/E_C ratio. Using perturbation theory, the Hamiltonian of a transmon can be rewritten as [3]

$$\hat{\mathcal{H}} \cong \sqrt{8E_J E_C} \left(\hat{b}^\dagger \hat{b} + \frac{1}{2} \right) - E_J - \frac{E_C}{12} (\hat{b}^\dagger + \hat{b})^4. \quad (2.11)$$

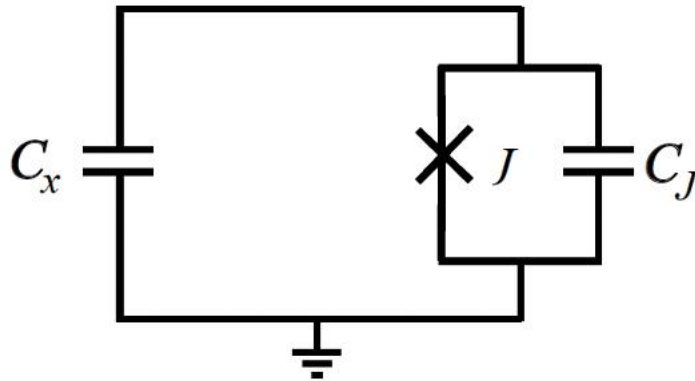


Figure 2.4: Circuit diagram of an isolated transmon.

\hat{b}^\dagger and \hat{b} are the corresponding creation and annihilation operators, respectively for excitations in the transmon, and we have only retained terms to 4th order in \hat{b}^\dagger and \hat{b} . The first term is the harmonic oscillator Hamiltonian, with spacing between levels $\sqrt{8E_J E_C}$ while the last term introduces an anharmonicity. In this approximation, the energy of the m -th level E_m is [13]

$$E_m = \sqrt{8E_J E_C} \left(j + \frac{1}{2} \right) - E_J - \frac{E_C}{4} (2m^2 + 2m + 1). \quad (2.12)$$

Thus, the transmon transition energy E_{01} is to this order:

$$E_{01} = E_1 - E_0 = \sqrt{8E_J E_C} - E_C. \quad (2.13)$$

In order to function as a qubit, the transmon levels need to be anharmonic. In other words, the next highest transition energy $E_{12} = E_2 - E_1$ must be sufficiently different from E_{01} that the lowest two energy levels ($m = 0, 1$) can be driven without producing excitations to the $m = 2$ level. The anharmonicity α is defined as:

$$\alpha = E_{12} - E_{01}. \quad (2.14)$$

From Equation (2.13), one finds [9]

$$\alpha = -E_C. \quad (2.15)$$

This negative sign of α means E_{12} is smaller than E_{01} . For $E_{01}/h \sim 3$ to 10 GHz, one typically would like $\alpha \approx -200$ MHz and this gives $20 \lesssim E_J/E_C \lesssim 200$ as an acceptable range for the transmon. It should also be noted that Eq. (2.15) is only approximate and more accurate values for E_m and α can be obtained with the Mathieu function solutions.

2.5 Circuit QED System

A transmon is often capacitively coupled to a microwave resonator to provide control and allow the state to be measured [9]. The resonator can be a planar resonator (for 2D transmons) [14][15] or a 3D cavity (for 3D transmons) [16][17]. This arrangement makes use of circuit quantum electrodynamics (cQED) techniques [2]. The cQED technique has several important benefits, including: (1) isolation of the qubit from direct coupling to the external electromagnetic environment; (2) high-power and quantum non-demolition microwave measurements (QND) [18]; and (3) potential to be used as quantum bus [19] for entangling multiple qubits.

The Jaynes-Cummings Hamiltonian was developed in 1963 by Edwin T. Jaynes and Frederick W. Cummings [20] to describe the interaction of a two-level atom with a single mode of a quantum electromagnetic field. In cQED, this approach has been generalized to model the Hamiltonian of a qubit linked to a single mode of a cavity.

For a two-level system with a transition frequency ω_q coupled to a cavity with frequency ω_r , the Jaynes-Cummings Hamiltonian is [20]

$$\hat{\mathcal{H}} = \hbar\omega_r \hat{a}^\dagger \hat{a} + \frac{\hbar\omega_q}{2} \hat{\sigma}_z + \hbar g_{ge} (\hat{a} \hat{\sigma}^+ + \hat{a}^\dagger \hat{\sigma}^-). \quad (2.16)$$

Here the coupling strength is g_{ge} , \hat{a}^\dagger is the creation operator for photons in the cavity and \hat{a} is the annihilation operator. $\hat{\sigma}_x$, $\hat{\sigma}_y$, and $\hat{\sigma}_z$ are the x -, y - and z -Pauli matrices, respectively and the raising and lowering operators σ^\pm are defined as

$$\sigma^\pm = \frac{\sigma_x \pm i\sigma_y}{2}. \quad (2.17)$$

The σ operators only act on the qubit state. Let the qubit's energy eigenstates be $|g\rangle$ and $|e\rangle$, and the resonator's energy eigenstates be the number states $|n\rangle$. The product states denoted by $|g, n\rangle$ and $|e, n\rangle$ are a natural choice for the basis of the coupled system. The coupling term in this basis

is entirely off-diagonal has the critical property of preserving the total number of excitations in the system. The matrix elements of the coupling terms are [20]:

$$\hbar g_{ge} \langle g, m | (a\sigma^+ + a^\dagger\sigma^-) | e, n \rangle = \hbar g_{ge} \sqrt{n+1} \delta_{m, n+1} \quad (2.18a)$$

$$\hbar g_{ge} \langle e, n | (a\sigma^+ + a^\dagger\sigma^-) | g, m \rangle = \hbar g_{ge} \sqrt{m+1} \delta_{n, m+1} \quad (2.18b)$$

The coupling term effectively mixes states with the same total number of excitations. It is useful to define an operator \mathcal{N} for the total number of excitations as [20]

$$\mathcal{N} = a^\dagger a + \frac{\sigma_z}{2} + \frac{1}{2}, \quad (2.19)$$

I note that with this definition, the number of excitations is zero for the ground state of the system, *i.e.*

$$\mathcal{N} |g, 0\rangle = 0. \quad (2.20)$$

Due to the structure of the Jaynes-Cummings coupling term, we can rewrite the Hamiltonian in Eq. (2.16) with a block-diagonal form in the number basis with 2×2 blocks along the diagonal:

$$\hbar \begin{bmatrix} (n-1)\omega_r + \frac{\omega_{ge}}{2} & g_{ge}\sqrt{n} \\ g_{ge}\sqrt{n} & n\omega_r - \frac{\omega_{ge}}{2} \end{bmatrix}. \quad (2.21)$$

The eigenvalues of this matrix are:

$$E_{n,\pm} = \left(n - \frac{1}{2}\right) \hbar \omega_r \pm \frac{\hbar}{2} \sqrt{\Delta^2 + 4g_{ge}^2 n}, \quad (2.22)$$

where Δ is the detuning between the qubit and resonator frequencies $\Delta \equiv \omega_{ge} - \omega_r$. The corresponding eigenvectors are given by

$$|n, +\rangle = \cos(\theta_n) |e, n-1\rangle + \sin(\theta_n) |g, n\rangle \quad (2.23a)$$

$$|n, -\rangle = -\sin(\theta_n) |e, n-1\rangle + \cos(\theta_n) |g, n\rangle. \quad (2.23b)$$

where the θ_n is given as

$$\tan(2\theta_n) = \frac{2g_{ge}\sqrt{n}}{\Delta}. \quad (2.24)$$

The ground state is $|g, 0\rangle$ with energy

$$E_0 = -\frac{\hbar\omega_{ge}}{2}. \quad (2.25)$$

The states $|n, \pm\rangle$ are the dressed states of the Jaynes-Cummings system. The uncoupled qubit and resonator 'bare states' are 'dressed' due to the coupling.

Define the critical number of photons

$$n_{\text{crit}} \equiv \frac{\Delta^2}{4g_{ge}^2}. \quad (2.26)$$

In terms of n_{crit} , we can write the energy eigenvalues as

$$E_{n,\pm} = \left(n - \frac{1}{2}\right) \hbar\omega_r \pm \frac{\hbar\Delta}{2} \left(1 + \frac{n}{n_{\text{crit}}}\right)^{\frac{1}{2}}. \quad (2.27)$$

and then we have

$$\tan 2\theta_n = \sqrt{\frac{n}{n_{\text{crit}}}}. \quad (2.28)$$

From these expressions, we see that the ratio n/n_{crit} is an important parameter in determining the eigenvalues and eigenvectors of the Hamiltonian.

The limit $n \ll n_{\text{crit}}$ is called the dispersive limit. From Eq. (2.26), we can see that this limit is more easily satisfied when $\Delta \gg g_{ge}$. In this limit, with perturbation expansion of the expressions we have:

$$E_{n,\pm} \approx \left(n - \frac{1}{2}\right) \hbar\omega_r \pm \frac{\hbar\Delta}{2} \left(1 + \frac{2g_{ge}^2 n}{\Delta^2}\right). \quad (2.29)$$

We then write the unitary transformation \mathcal{J} as

$$\mathcal{T} \approx \exp\left\{\frac{g_{ge}}{\Delta}(a\sigma^+ - a^\dagger\sigma^-)\right\}. \quad (2.30)$$

Applying this transformation, we have Hamiltonian:

$$\mathcal{T}H_{JC}\mathcal{T}^\dagger \approx \tilde{H}_{JC}^{(2)} = \hbar\omega_r a^\dagger a + \frac{\hbar\tilde{\omega}_{ge}}{2}\sigma_z + \hbar\chi(a^\dagger a)\sigma_z. \quad (2.31)$$

where $\chi = g_{ge}^2/\Delta$ is called the 'dispersive shift' of the resonator frequency and $\tilde{\omega}_{ge} = \omega_{ge} + \chi$ is the Lamb-shifted qubit frequency.

To understand how the state of a qubit can be manipulated, one needs to include in the Hamiltonian the effect of a microwave drive. Following the method of Steck [21], I consider the situation where the qubit is driven by an oscillating electric field. Suppose that the electric field is given by

$$\vec{E}(t) = \vec{\varepsilon}E_0 \cos \omega_d t \equiv \frac{1}{2}\vec{\varepsilon}E_0(e^{i\omega_d t} + e^{-i\omega_d t}), \quad (2.32)$$

where $\vec{\varepsilon}$ is the polarization vector for the field, E_0 is the amplitude of the electric field of the drive, and ω_d is the drive frequency. If the qubit has an electric dipole moment operator \hat{d} , then we can write [22]

$$\hat{d} = \langle g|\hat{d}|e\rangle(|g\rangle\langle e| + |e\rangle\langle g|) \equiv \langle g|\hat{d}|e\rangle(\sigma^- + \sigma^+). \quad (2.33)$$

The drive Hamiltonian can then be written as [22]

$$\begin{aligned} \mathcal{H}_{\text{int}} &= -\hat{d} \cdot \vec{E} \\ &= \frac{E_0}{2} \langle g|\vec{\varepsilon} \cdot \hat{d}|e\rangle(\sigma^- + \sigma^+)(e^{i\omega_d t} + e^{-i\omega_d t}) \\ &\simeq \frac{E_0}{2} \langle g|\vec{\varepsilon} \cdot \hat{d}|e\rangle(\sigma^- e^{i\omega_d t} + \sigma^+ e^{-i\omega_d t}). \end{aligned} \quad (2.34)$$

Here I have applied the rotating wave approximation (RWA) [23] to average out the fast counter-rotating terms. The Rabi frequency [24] for the atom interacting with the field can then be defined

as

$$\Omega_q = -\frac{E_0}{\hbar} \langle g | \vec{\epsilon} \cdot \vec{d} | e \rangle. \quad (2.35)$$

With this definition, the drive Hamiltonian can be written as,

$$\mathcal{H}_{\text{int}} = \frac{\hbar\Omega_q}{2} (\sigma^- e^{i\omega_d t} + \sigma^+ e^{-i\omega_d t}). \quad (2.36)$$

The drive Hamiltonian for a resonator can be obtained by replacing the qubit operators in Eq. (2.36) with the corresponding ladder operators for a resonator [25]:

$$\mathcal{H}_{\text{int}}^{(\text{res})} = \frac{\hbar\Omega_r}{2} (ae^{i\omega_d t} + a^\dagger e^{-i\omega_d t}), \quad (2.37)$$

where Ω_r is the effective Rabi drive frequency for the resonator. The driven Jaynes-Cummings Hamiltonian in the dispersive limit can then be written as,

$$\begin{aligned} \vec{\mathcal{H}} = & \hbar\omega_r a^\dagger a + \frac{\hbar}{2} (\omega_{\text{ge}} + 2\chi a^\dagger a) \sigma_z \\ & + \frac{\hbar\Omega_q}{2} (\sigma^- e^{i\omega_d t} + \sigma^+ e^{-i\omega_d t}) + \frac{\hbar\Omega_r}{2} (ae^{i\omega_d t} + a^\dagger e^{-i\omega_d t}). \end{aligned} \quad (2.38)$$

A unitary transformation to the rotating frame of the drive can be applied to remove the time dependence [26] yielding:

$$\mathcal{H} = \hbar\Delta_r a^\dagger a + \frac{\hbar}{2} (\Delta_{\text{ge}} + 2\chi a^\dagger a) \sigma_z + \frac{\hbar\Omega_q}{2} (\sigma^- + \sigma^+) + \frac{\hbar\Omega_r}{2} (a + a^\dagger), \quad (2.39)$$

where $\Delta_r = \omega_r - \omega_d$ and $\Delta_{\text{ge}} = \omega_{\text{ge}} - \omega_d$ are the detunings between the drive and the resonator or qubit respectively.

2.6 Energy Relaxation and Dissipation Mechanisms

Roughly speaking, the relaxation time T_1 measures how long it takes for the excited state to return to its undriven steady state. In the last two decades, better fabrication techniques, deeper

understanding of relaxation mechanisms and better qubit designs have led to large improvements in T_1 of superconducting qubits (from μs to ms) [27][28]. The main factors affecting T_1 are coupling to microwave mode [29], dielectric TLS loss [30] and loss due to quasiparticles. My main focus was on quasiparticle induced relaxation [31] due to non-equilibrium quasiparticles tunneling through the transmon junction.

2.6.1 Relaxation Time T_1

The precise definition of the relaxation time T_1 is that it is the time required for the qubit to return to its equilibrium thermal state after it has been excited. For non-zero temperature, this will differ from the time for the excited state to return to the ground state. In general, the relaxation rate can be written as [32]

$$\frac{1}{T_1} = \Gamma_{e \rightarrow g} + \Gamma_{g \rightarrow e}. \quad (2.40)$$

Here $\Gamma_{e \rightarrow g}$ is the rate at which the excited state $|e\rangle$ relaxes back to the ground state $|g\rangle$, and $\Gamma_{g \rightarrow e}$ is the rate at which the qubit is thermally excited from $|g\rangle$ to $|e\rangle$. The importance of T_1 arises from manipulating quantum states effectively. If the excited state decays too fast, it becomes challenging to perform many operations before quantum coherence is lost and there is an error in a computation.

It is essential to note that T_1 would not be infinite even at absolute zero temperature ($T=0$). This limitation arises due to coupling of the qubit to the electromagnetic environment and other atomic-scale quantum systems.

For a transmon, the environment's influence can be characterized by the complex admittance $Y(\omega)$. Analogous to the impedance of free space Z_0 , the reciprocal of the real part of Y quantifies the dissipation experienced by the device. Specifically, for each transmon decay

process, we can associate an admittance $Y(\omega)$ in parallel with the transmon. The transmon's characteristic decay RC time constant is then given by [33][34]

$$T_1 = \frac{C_\Sigma}{\text{Re} Y(\omega_{ge})}, \quad (2.41)$$

where $C_\Sigma = C_B + C_J$ is the total capacitance across the Josephson junction.

In practice, it is often necessary to include more than one loss mechanism and the overall relaxation rate Γ_1 is

$$\Gamma_1 = \frac{1}{T_1} = \sum_i \frac{1}{T_{1,i}}. \quad (2.42)$$

where $1/T_{1,i}$ is the relaxation rate from the i^{th} relaxation channel.

2.6.2 Purcell Effect

The Purcell effect discovered in 1946 by Edward M. Purcell [29] describes the enhancement or suppression of the spontaneous emission rate of atoms in a resonant cavity. According to Fermi's golden rule [35], the transition rate of an atom in vacuum is proportional to the density of states of the final states. Except near a cavity resonance, the density of final photon states in a cavity is much lower than the density of states in free space. For coupling of a transmon to a single-mode cavity, the Purcell effect contribution to relaxation is given by [29]

$$\frac{1}{T_{1, \text{Purcell}}} = \left(\frac{g_{ge}}{\omega_r - \omega_q} \right)^2 \kappa. \quad (2.43)$$

It should be emphasized that this formula is only applicable for $|\omega_r - \omega_q| \gg |g_{ge}|$. Due to the Purcell effect, the spontaneous emission rate of a qubit in a cavity can be increased in the case of resonance and decreased in the case of far detuning, compared to qubit in free space. The transmon relaxation in the ‘‘Purcell limit’’ will be determined by the cavity decay rate κ , and hence by the

cavity photon lifetime as well as the detuning and the coupling to the cavity. Additional Purcell contributions will typically be present as a result of the qubit's coupling to higher order cavity modes. Increasing $|\omega_r - \omega_q|$ is often the easiest way to decrease Purcell loss. However, the cavity is also used to read out the qubit state and increasing $|\omega_r - \omega_q|$ reduces the signal-to-noise ratio in the read-out. Another method to prevent qubit relaxation from the Purcell effect while preserving measurement rate is to use a Purcell filter [36], which restricts microwave transmission at the qubit frequency via bandpass filtering.

2.6.3 Two-Level Systems

TLS loss refers to dissipation caused by the interaction between the qubit and atomic-scale two-level systems (TLSs) in the surrounding dielectric materials [37]. TLSs are due to microscopic defects or impurities that can couple electrically to the qubit, resulting in relaxation and dephasing processes. Two-level systems (TLSs) may exist in Al oxide in the Josephson junction, any exposed metal surface and the substrate, as well as the substrate-metal and substrate-air interface TLS loss. It has been identified as a significant factor in limiting the T_1 of transmons [30][37][38]

The relaxation rate of a transmon due to TLS loss can be written as:

$$\frac{1}{T_1} = \frac{\omega_{ge}}{Q_{\tan \delta}} = \omega_{ge}(P_{AS} \tan \delta_{AS} + P_{SC} \tan \delta_{SC} + P_{CA} \tan \delta_{CA}). \quad (2.44)$$

Here P_k is the participation ratio, defined as the fraction of electric energy stored in the volume of region k with intrinsic quality factor Q_k and loss tangent $\tan \delta_k$ in the single photon limit. AS , SC and CA represent the interfaces between air and substrate, substrate and conductor, and conductor and air. Additionally, TLS-induced dephasing processes reduce the coherence, limiting the fidelity of quantum gate operations. A significant complication is that TLS loss depends on power and

temperature. In addition, there may be discrete, TLS's as well as a continuous background, which can affect the expected frequency dependence and temperature dependence.

2.6.4 Quasiparticle Loss

As mentioned in Section 2.3, a Cooper pair consists of two electrons with opposite momentum and spin that are bound together. A dc current carried by Cooper pairs exhibit zero resistance, a signature of the superconducting state. It takes energy $\sim 2\Delta$ to break a Cooper pair, but doing so creates excitations known as quasiparticles. Non-equilibrium quasiparticles are now a well-recognized source of relaxation in superconducting qubits [31][39]-[41]. When a quasiparticle tunnels through the junction [42], it can gain or lose some of its energy E . In particular, a quasiparticle tunneling through the junction can cause an excited qubit to decay by transferring energy $\hbar\omega_{ge}$ from the qubit to the quasiparticle. Quasiparticle tunneling can also excite a qubit from the ground-state qubit to the excited state by transferring energy $\hbar\omega_{ge}$ from the quasiparticle to the qubit.

The current noise created by quasiparticles tunneling through the junction is intrinsically related to dissipation. For conventional single-particle tunneling (no multiple Andreev reflection), the quasiparticle current noise power spectrum at frequency f_{ge} can be written as [43]

$$S_I(f_{ge}) = e(I_{L \rightarrow R} + I_{R \rightarrow L}), \quad (2.45)$$

where $f_{ge} = \omega_{ge}/2\pi$ is the qubit $|g\rangle$ to $|e\rangle$ transition frequency, $I_{L \rightarrow R}$ is the current flowing across the junction as a result of quasiparticles travelling from the left to the right electrode when there is a voltage $\hbar f_{ge}/e$ across the junction and $I_{R \rightarrow L}$ is the current generated by quasiparticles traveling from the right to the left electrode. This quasiparticle tunneling noise can induce spontaneous transitions between the qubit states $|e\rangle \leftrightarrow |g\rangle$. In Eq. (2.45), $S_I(f_{ge})$ is a double-sided quantum

noise spectrum [32] with positive frequency corresponding to the transition $|e\rangle \rightarrow |g\rangle$ and negative frequency corresponding to the transition $|g\rangle \rightarrow |e\rangle$. From Fermi's golden rule, the rate at which $|e\rangle$ relaxes back to $|g\rangle$ is [43]

$$\Gamma_{e \rightarrow g} = \left| \left\langle g \left| \sin \frac{\hat{\phi}}{2} \right| e \right\rangle \right|^2 S_I(f_{ge}) = \frac{E_c}{\hbar f_{ge} e^2} S_I(f_{ge}). \quad (2.46)$$

For negative frequencies, the noise produces excitations of the ground state of the transmon at a rate given by [43]

$$\Gamma_{g \rightarrow e} = \left| \left\langle e \left| \sin \frac{\hat{\phi}}{2} \right| g \right\rangle \right|^2 S_I(-|f_{ge}|) = \frac{E_c}{\hbar |f_{ge}| e^2} S_I(-|f_{ge}|). \quad (2.47)$$

Then the relaxation rate $\Gamma_{1,qp}$ due to quasiparticle tunneling can be written as

$$\Gamma_{1,qp} \equiv \frac{1}{T_{1,qp}} = \frac{E_c}{\hbar e^2} \left(\frac{S_I(f_{ge})}{f_{ge}} + \frac{S_I(-|f_{ge}|)}{|f_{ge}|} \right). \quad (2.48)$$

To use this expression, we must determine $S_I(f_{ge})$, which depends on the quasiparticle density and distribution. MAR (Multiple Andreev Reflections) effects may also be important, and Eq. (2.48) will then require considerable modification. More discussion about quasiparticle loss can be found in Chapter 4 where I give a detailed analysis of the situation including the temperature dependence, and when the tunnel junction has electrodes with different energy gaps.

2.7 Dephasing Time T_ϕ

The dephasing time T_ϕ quantifies the loss of phase coherence due to pure dephasing processes, *i.e.* processes that do not cause energy relaxation. Pure dephasing can be attributed to noise in transition frequency of the system. Any pure state of a quantum system with two levels can be represented as

$$|\psi(0)\rangle = \cos\left(\frac{\theta}{2}\right)|0\rangle + \sin\left(\frac{\theta}{2}\right)e^{i\phi_0}|1\rangle, \quad (2.49)$$

where $|0\rangle$ and $|1\rangle$ are the ground state and excited state of the qubit. θ_0 and ϕ_0 can be considered as polar and azimuthal angles on the Bloch sphere (see Fig. 2.5). Now, assuming that relaxation can be ignored, the time evolution of the state can be determined by applying the unitary operator on $|\psi(0)\rangle$:

$$U(t) = e^{-\frac{i\mathcal{H}t}{\hbar}}. \quad (2.50)$$

\mathcal{H} is the Hamiltonian of the system. Applying $U(t)$ to Eq. (2.49) then gives

$$\begin{aligned} |\psi(t)\rangle &= e^{-\frac{i\mathcal{H}t}{\hbar}} |\psi(0)\rangle \\ &= \cos\left(\frac{\theta}{2}\right)e^{-\frac{iE_g t}{\hbar}}|g\rangle + \sin\left(\frac{\theta}{2}\right)e^{i\left(\phi_0 - \frac{E_e t}{\hbar}\right)}|e\rangle. \end{aligned} \quad (2.51)$$

Note in Eq. (2.51) that the overall phase of $|\psi(t)\rangle$ has no physical relevance. After removing an overall complex factor, the physically equivalent state can be written as

$$|\psi(t)\rangle = \cos\left(\frac{\theta}{2}\right)|g\rangle + \sin\left(\frac{\theta}{2}\right)e^{i\left(\phi_0 - \frac{(E_e - E_g)t}{\hbar}\right)}|e\rangle. \quad (2.52)$$

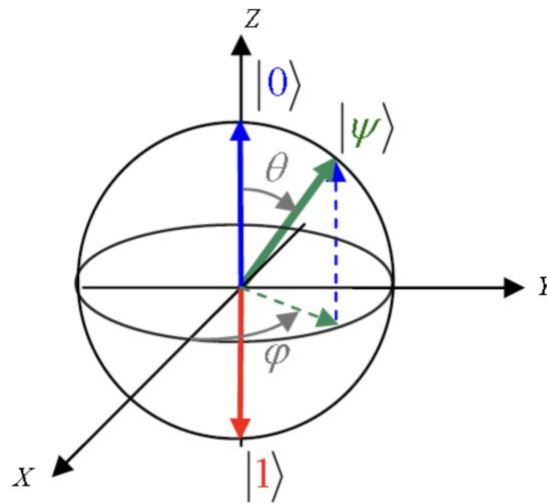


Figure 2.5: Geometrical representation of Bloch Sphere. $|\psi\rangle$ is a state in between the $|0\rangle$ and $|1\rangle$.

The g -to-e transition angular frequency is:

$$\omega_{ge} \equiv \frac{E_e - E_g}{\hbar} = \frac{E_{ge}}{\hbar}. \quad (2.53)$$

I can then write:

$$|\psi(t)\rangle = \cos\left(\frac{\theta}{2}\right)|g\rangle + \sin\left(\frac{\theta}{2}\right)e^{i(\phi_0 - \omega_{ge}t)}|e\rangle. \quad (2.54)$$

Let us now assume that the qubit transition frequency fluctuates in time as [44]

$$\omega_{ge}(t) = \langle\omega_{ge}\rangle - \delta\omega_{ge}(t), \quad (2.55)$$

where $\delta\omega_{ge}(t)$ is the fluctuation at time t . Then the phase at time t can be defined as

$$\phi(t) = \phi_0 - \langle\omega_{ge}\rangle t - \int_0^t \delta\omega_{ge}(t') dt'. \quad (2.56)$$

The correlation function $\phi(t)$ for the phase fluctuations can now be written as

$$\phi(t) \equiv \langle\delta\omega_{ge}(0)\delta\omega_{ge}(t)\rangle = \frac{1}{2\pi} \int_{-\infty}^{\infty} S_{\omega_{ge}}(\omega) e^{-i\omega t} d\omega, \quad (2.57)$$

where $S_{\omega_{ge}}(\omega)$ is the power spectrum of the frequency fluctuations.

Now consider the function

$$F(t) \equiv \left\langle e^{-i \int_0^t \delta\omega_{ge}(t') dt'} \right\rangle. \quad (2.58)$$

Using the relation $\langle e^{i\Delta\phi} \rangle = e^{-\frac{1}{2}\langle\Delta\phi^2\rangle}$ [44], then we have:

$$\begin{aligned} F(t) &= \exp\left(-\frac{1}{2} \int_0^t dt_1 \int_0^t dt_2 \langle\delta\omega_{ge}(t_1)\delta\omega_{ge}(t_2)\rangle\right) \\ &= \exp\left(-\frac{1}{4\pi} \int_{-\infty}^{\infty} d\omega S_{\omega_{ge}}(\omega) \int_0^t dt_1 \int_0^t dt_2 e^{-i\omega(t_1-t_2)}\right) \\ &= \exp\left(-\frac{|t|}{2\pi} \int_{-\infty}^{\infty} d\left(\frac{\omega t}{2}\right) S_{\omega_{ge}}(\omega) \text{sinc}^2\left(\frac{\omega t}{2}\right)\right). \end{aligned} \quad (2.59)$$

The $\text{sinc}^2(\omega t/2)$ term will give higher dephasing at lower noise frequencies. This relation can be used to examine the dephasing due to some standard types of noise [44].

Consider first Gaussian white noise, which has a uniform noise power spectral density $S_{\omega_{ge}}(\omega) = S_0$. For this case, Eq. (2.59) can be evaluated as

$$F(t) = e^{-\frac{|t|S_0}{2}}. \quad (2.60)$$

This indicates that the phase decay is exponential with dephasing time constant: $T_\phi = 2/S_0$.

Next consider the case of $1/f$ noise [44] with $S_{\omega_{ge}}(\omega) \propto 1/|\omega|$. One finds [44]:

$$F(t) \propto e^{-\frac{t^2}{2\sigma^2}}. \quad (2.61)$$

The phase decays with a Gaussian envelope.

Due to the reconfiguration of ions within the tunnel barrier, Josephson junctions may exhibit critical current fluctuations and charge noise [45]. Noise in I_0 causes fluctuations in E_J and hence fluctuations in ω_{ge} . Since $\omega_{ge} \propto \sqrt{I_c}$, the variance in ω_{ge} can be written as [46]:

$$\langle \delta\omega_{ge}^2 \rangle = \left(\frac{\partial\omega_{ge}}{\partial I_c} \right)^2 \langle \delta I_0^2 \rangle \simeq \left(\frac{\omega_{ge}}{2I_c} \right)^2 \langle \delta I_0^2 \rangle. \quad (2.62)$$

For a $1/f$ spectrum, we can apply Eq. (2.61) and show that:

$$T_\phi \propto \frac{2}{\omega_{ge}}. \quad (2.63)$$

Charge noise enters in an analogous form,

$$\langle \delta\omega_{ge}^2 \rangle = \left(\frac{\partial\omega_{ge}}{\partial n_g} \right)^2 \langle \delta n_g^2 \rangle. \quad (2.64)$$

Due to coupling between the transmon and cavity in a cQED system, fluctuations in the number of photons N in the microwave cavity also causes dephasing. If the microwave input/output lines are not properly isolated and thermalized, this can impose significant limitations on the coherence time. In particular, the transverse coupling [47] of a transmon and cavity mode induces

a 2χ shift in ω_{ge} per cavity photon. In 2006, A. A. Clerk and D. Wahyu Utami [48] demonstrated that dephasing from cavity photons could be expressed as

$$\frac{1}{T_\phi} \equiv \Gamma_\phi = \frac{\kappa}{2} \operatorname{Re} \left[\sqrt{\left(1 + \frac{2i\chi}{\kappa}\right)^2 + \frac{8i\bar{n}\chi}{\kappa}} - 1 \right], \quad (2.65)$$

where κ is the cavity decay rate, and \bar{n} is the average number of thermal photons in the cavity. In this limit $\chi \gg \kappa$, this reduced to

$$\frac{1}{T_\phi} \cong \bar{n}\kappa \quad (2.66)$$

2.8 Coherence Time T_2

A qubit that is prepared in a superposition state can decohere due to dephasing and energy relaxation processes. The coherence time T_2 is related to T_1 and T_ϕ by [49]:

$$\frac{1}{T_2} = \frac{1}{2T_1} + \frac{1}{T_\phi}. \quad (2.67)$$

This relation puts an important upper bound on T_2 given by $T_2 \ll 2T_1$.

The coherence time T_2 is also called the spin-echo time [50]. Spin-echo measurements are insensitive to first-order inhomogeneous broadening, *i.e.* spin-echo decay measurements are insensitive to minor shot-to-shot variations in energy level transition frequencies. The Ramsey coherence time, also known as the spectroscopic coherence time T_2^* , is another useful characteristic time of a qubit. The spin-echo decay time T_2 is insensitive to shot-to-shot variations (inhomogeneous broadening), whereas the Ramsey decay time T_2^* includes contributions from inhomogeneous broadening. Ramsey spectroscopy includes contributions from loss, pure dephasing, and inhomogeneous broadening. Thus, $T_2^* \leq T_2$. For a qubit that experiences low-frequency disturbances, T_2^* can be important for understanding possible causes.

Chapter 3

The Superconducting Energy Gap Δ and Granular Aluminum Thin Films

The superconducting gap Δ is often thought of as being an intrinsic property of a superconducting material. However, granular aluminum thin films exhibit a superconducting gap that depends on the size of the grains. In this chapter, I discuss the superconducting gap and the behavior of granular aluminum thin films. A major goal of my research was to produce granular Al thin films with specific gap values and then use these to build long-lived transmons (see Chapter 5).

3.1 BCS Theory and Superconducting Gaps

Bardeen, Cooper, and Schrieffer (BCS) proposed in the late 1950s [1][2], a theory that provided the first basic understanding of superconductivity. It accomplished this by offering a microscopic explanation of superconductivity based on quantum mechanics. One of the key features of the BCS theory is that the electrons form a Cooper pair [3]. The pairing involves the electrons causing a distortion of the crystal lattice by attracting nearby positive ions. This altered electrostatic environment subsequently attracts a second electron. This can be thought of as two electrons exchanging a virtual photon. The two electrons in a Cooper pair possess opposite momenta and opposite spin (s-wave pairing).

Thus, the BCS provided an explanation to how electrons can surmount the Coulomb repulsion, which normally would prevent two negatively charged electrons from binding together.

The Coulomb force between two electrons is inherently repulsive due to their negative charge. However, in the BCS theory, this repulsion is attenuated by the electrical screening within a conductor; the collective behavior of free-moving charge carriers neutralizes an external electric field within a short distance [1].

Another key feature of the BCS theory is the existence of a critical temperature T_c below which the Cooper pairs are condensed into a coherent macroscopic quantum state described by the BCS wave function. At sufficiently low temperatures, the production of Cooper pairs causes an instability in the Fermi Sea of electrons, and the Cooper pairs condense into a single ground state. The BCS ground state wavefunction is:

$$|\Psi_{\text{BCS}}\rangle = \prod_{k=k_1, k_2 \dots k_n} (u_k + v_k c_{k,\uparrow}^\dagger c_{-k,\downarrow}^\dagger) |\Phi_0\rangle, \quad (3.1)$$

where $c_{k,\uparrow}^\dagger c_{-k,\downarrow}^\dagger$ represents the pair creation operator with 0 total momentum, $|v_k|^2$ is the electron occupancy probability, $|u_k|^2 = 1 - |v_k|^2$ is the electron vacancy probability, and $|\Phi_0\rangle$ is the vacuum state (no electrons). The BCS Hamiltonian of a superconducting system is:

$$\hat{H} = \sum_{k,\sigma} (\epsilon_k - \mu) c_{k,\sigma}^\dagger c_{k,\sigma} + \sum_{k,l} V_{kl} c_{k,\uparrow}^\dagger c_{-k,\downarrow}^\dagger c_{-l,\downarrow} c_{l,\uparrow}. \quad (3.2)$$

The first term is the kinetic energy of the electrons with respect to the system's chemical potential μ . The second term represents the attractive interaction between electrons with interaction coupling strength V_{kl} .

The ground state $|\Psi_{\text{BCS}}\rangle$ given in Eq. (3.1) is a many-body state composed of a phase-coherent superposition of pairs of electrons occupying states $(k \uparrow, -k \downarrow)$. Following the discussion in Tinkham [4] due to the coherence, operators $c_{-k\downarrow} c_{k\uparrow}$ can have non zero expectation values and we can write $c_{-k\downarrow} c_{k\uparrow} = \langle c_{-k\downarrow} c_{k\uparrow} \rangle + (c_{-k\downarrow} c_{k\uparrow} - \langle c_{-k\downarrow} c_{k\uparrow} \rangle)$, where the second term can be small

[4]. Substituting this expression into the interaction term in the Hamiltonian Eq. (3.2), one finds

[4]:

$$\begin{aligned}
\hat{H} &= \sum_{k,\sigma} (\epsilon_k - \mu) c_{k,\sigma}^\dagger c_{k,\sigma} + \sum_{k,l} V_{kl} (\langle c_{k\uparrow}^\dagger c_{-k\downarrow}^\dagger \rangle \langle c_{-l\downarrow} c_{l\uparrow} \rangle + \langle c_{k\uparrow}^\dagger c_{-k\downarrow}^\dagger \rangle \langle c_{-l\downarrow} c_{l\uparrow} \rangle \\
&\quad - \langle c_{-l\downarrow} c_{l\uparrow} \rangle) + (c_{k\uparrow}^\dagger c_{-k\downarrow}^\dagger - \langle c_{k\uparrow}^\dagger c_{-k\downarrow}^\dagger \rangle) \langle c_{-l\downarrow} c_{l\uparrow} \rangle \\
&= \sum_{k,\sigma} (\epsilon_k - \mu) c_{k,\sigma}^\dagger c_{k,\sigma} + \sum_{k,l} V_{kl} (\langle c_{k\uparrow}^\dagger c_{-k\downarrow}^\dagger \rangle c_{-l\downarrow} c_{l\uparrow} + c_{k\uparrow}^\dagger c_{-k\downarrow}^\dagger \langle c_{-l\downarrow} c_{l\uparrow} \rangle \\
&\quad - \langle c_{k\uparrow}^\dagger c_{-k\downarrow}^\dagger \rangle \langle c_{-l\downarrow} c_{l\uparrow} \rangle). \tag{3.3}
\end{aligned}$$

The order parameter can now be defined as $\Delta_k = -\sum_l V_{kl} \langle c_{-l\downarrow} c_{l\uparrow} \rangle$ [4] which allows the Hamiltonian to be written as

$$\hat{H} = \sum_{k,\sigma} (\epsilon_k - \mu) c_{k,\sigma}^\dagger c_{k,\sigma} - \sum_k (\Delta_k^\dagger c_{-k\downarrow} c_{k\uparrow} + \Delta_k c_{k\uparrow}^\dagger c_{-k\downarrow}^\dagger - \Delta_k \langle c_{k\uparrow}^\dagger c_{-k\downarrow}^\dagger \rangle). \tag{3.4}$$

Equation (3.4) can then be written in matrix form [4]

$$\hat{H} = \sum_k \left[\begin{pmatrix} c_{k\uparrow}^\dagger & c_{-k\downarrow} \end{pmatrix} \begin{pmatrix} \xi_k & -\Delta_k \\ -\Delta_k^\dagger & -\xi_k \end{pmatrix} \begin{pmatrix} c_{k\uparrow} \\ c_{-k\downarrow}^\dagger \end{pmatrix} + \xi_k + \Delta_k b_k^\dagger \right]. \tag{3.5}$$

Here note that $\xi_k = \epsilon_k - \mu$ and $b_k = \langle c_{-k\downarrow} c_{k\uparrow} \rangle$. The Hamiltonian can now be diagonalized by introducing the quasiparticle operators γ_{k0} and γ_{k1}^\dagger from the Bogoliubov-Valatin transformation [5]

$$\begin{aligned}
c_{k\uparrow} &= u_k^* \gamma_{k0} + v_k \gamma_{k1}^\dagger \\
c_{-k\downarrow}^\dagger &= -v_k^* \gamma_{k0} + u_k \gamma_{k1}^\dagger, \tag{3.6}
\end{aligned}$$

Using Eq. (3.6), we rewrite the Hamiltonian as

$$\begin{aligned}
\hat{H} &= \sum_k \left[\begin{pmatrix} \gamma_{k0}^\dagger & \gamma_{k1} \end{pmatrix} \begin{pmatrix} u_k & -v_k \\ v_k^* & u_k^* \end{pmatrix} \begin{pmatrix} \xi_k & -\Delta_k \\ -\Delta_k^\dagger & -\xi_k \end{pmatrix} \begin{pmatrix} u_k^* & v_k \\ -v_k^* & u_k \end{pmatrix} \begin{pmatrix} \gamma_{k0} \\ \gamma_{k1}^\dagger \end{pmatrix} \right. \\
&\quad \left. + \xi_k + \Delta_k b_k^\dagger \right]. \tag{3.7}
\end{aligned}$$

By expanding the middle three matrices and selecting the u_k and v_k so that the coefficients of the

off-diagonal terms $\gamma_{k0}^\dagger \gamma_{k1}^\dagger$ and $\gamma_{k1} \gamma_{k0}$ vanish, we may diagonalize the Hamiltonian Eq. (3.7) in the basis. The three middle matrices from Eq. (3.7) are multiplied which yield [add ref.]

$$\begin{pmatrix} (|u_k|^2 - |v_k|^2)\xi_k + \Delta_k u_k v_k^* + \Delta_k^* u_k^* v_k & 2u_k v_k \xi_k - u_k^2 \Delta_k + v_k^2 \Delta_k^* \\ 2u_k^* v_k^* \xi_k - u_k^{*2} \Delta_k^* + v_k^{*2} \Delta_k & -(|u_k|^2 - |v_k|^2)\xi_k + \Delta_k u_k v_k^* + \Delta_k^* u_k^* v_k \end{pmatrix}. \quad (3.8)$$

The coefficients of undesired (off-diagonal) components will disappear if

$$\left(\frac{\Delta_k^* v_k}{u_k}\right)^2 + 2\xi_k \left(\frac{\Delta_k^* v_k}{u_k}\right) - |\Delta_k|^2 = 0, \quad (3.9)$$

Solving the resulting quadratic equation yields:

$$\frac{\Delta_k^* v_k}{u_k} = \sqrt{\xi_k^2 + |\Delta_k|^2} - \xi_k = E_k - \xi_k, \quad (3.10)$$

where

$$E_k = \sqrt{\xi_k^2 + |\Delta_k|^2}. \quad (3.11)$$

E_k in Eq. (3.11) is the energy of a quasiparticle with wavevector k . From this result we see that the minimum energy to excite a quasiparticle is the energy gap $|\Delta_k|$. The quantity Δ_k can also be taken as the order parameter of the system [4][6][7] and disappears when $T > T_c$.

Using $|u_k|^2 + |v_k|^2 = 1$ and Eq. (3.10), we can also write

$$|v_k|^2 = 1 - |u_k|^2 = \frac{1}{2} \left(1 - \frac{\xi_k}{E_k}\right). \quad (3.12)$$

Using this expression, the remaining diagonal terms in Hamiltonian Eq. (3.7) can be evaluated and one finds [5]:

$$\hat{H} = \sum_k E_k (\gamma_{k0}^\dagger \gamma_{k0} + \gamma_{k1}^\dagger \gamma_{k1}) + \sum_k (\xi_k + \Delta_k b_k^\dagger - E_k). \quad (3.13)$$

The last item in Eq. (3.13) is called the condensation energy [5] and is the energy difference between the superconducting state and the normal state at $T = 0$. The first term in Eq. (3.13) is excitation energy from the ground state and the excitations (quasiparticles) are created by γ_{k0} and γ_{k1}^\dagger . The excitations are also known as "Bogoliubons" or "Bogoliubov quasiparticles."

By inverting the transformation in Eq. (3.5), we get [5]:

$$\begin{aligned}\gamma_{k0}^\dagger &= u_k^* c_{k\uparrow}^\dagger - v_k^* c_{-k\downarrow} \\ \gamma_{k1}^\dagger &= u_k^* c_{-k\downarrow}^\dagger + v_k^* c_{k\uparrow}.\end{aligned}\tag{3.14}$$

$c_{-k\downarrow}$ removes an electron with $(-k \downarrow)$ from the system and this is equivalent to introducing an electron with $(k \uparrow)$. Thus γ_{k0}^\dagger effectively forms excitations with momentum k and spin \uparrow . Similarly, γ_{k1}^\dagger creates excitations with wave vector $-k$ and spin \downarrow .

Combining Eq. (3.5) with the order parameter $\Delta_k = -\sum_l V_{kl} \langle c_{l\downarrow} c_{l\uparrow} \rangle$, we can write [5]

$$\Delta_k = -\sum_l V_{kl} u_l^* v_l (1 - \langle \gamma_{l0}^\dagger \gamma_{l0} \rangle - \langle \gamma_{l1}^\dagger \gamma_{l1} \rangle).\tag{3.15}$$

At $T = 0$, there will be no quasiparticles and Eq. (3.15) reduces to [5]:

$$\Delta_k = -\sum_l V_{kl} u_l^* v_l = -\frac{1}{2} \sum_l V_{kl} \frac{|\Delta_l|}{E_l},\tag{3.16}$$

To proceed, we can assume a very simple form for the BCS interaction:

$$V_{kl} = \begin{cases} -V & \text{if } |\xi_k| < \hbar\omega \\ 0 & \text{otherwise.} \end{cases}\tag{3.19}$$

Here ω represents the Debye cutoff frequency of the lattice. This choice implies that electron-electron interaction caused by the phonons only takes place in a thin shell near the Fermi surface. With this choice, the gap does not change with the direction of k . This is the "BCS model" of the electron-phonon interaction [1][2] and it yields an isotropic or s-wave symmetric pairing.

Inserting V_{kl} from Eq. (3.17) into Eq. (3.16), we can obtain a self-consistency equation [5]

$$\Delta = \begin{cases} \frac{V}{2} \sum_{\vec{k}} \frac{\Delta}{E_k} & \text{if } |\xi_{\vec{k}}| < \hbar\omega \\ 0 & \text{otherwise.} \end{cases} \quad (3.18)$$

In Eq. (3.18), I note that the sum is only over a small shell around the Fermi energy with $|\xi_{\vec{k}}| = |\epsilon_{\vec{k}} - \mu| < \hbar\omega$. Transforming the sum over \vec{k} into an integration over energy ξ from $-\hbar\omega$ to $\hbar\omega$, equation (3.18) becomes:

$$1 = V \int_0^{\hbar\omega} \frac{1}{\sqrt{\xi^2 + \Delta^2}} D(\xi) d\xi. \quad (3.19)$$

Note that the Δ has been cancelled from both sides of Eq. (3.18) and the factor of 2 disappears because of the symmetry of the integration over ξ . Substituting $\xi = x\Delta$ and assuming that for the limited integration range the typical metal density of states $D(\xi)$ can be taken as a constant D_0 , one finds [5]:

$$1 = VD_0 \sinh^{-1} x \Big|_0^{\frac{\hbar\omega}{\Delta}} = VD_0 \sinh^{-1} \left(\frac{\hbar\omega}{\Delta} \right) \quad (3.20)$$

Rearranging this expression gives the BCS equation for the energy gap [4]

$$\Delta = \frac{\hbar\omega}{\sinh \left(\frac{1}{VD_0} \right)} \approx 2\hbar\omega e^{\frac{-1}{VD_0}}. \quad (3.21)$$

This result for Δ is only accurate in the weak-coupling regime $D_0V \ll 1$. Also, the effects produced by quasiparticles must be considered at non-zero temperatures. At temperature T , the Fermi function provides the probability of a quasiparticle excitation with energy E_k :

$$f(E_k) = \frac{1}{e^{\frac{E_k}{k_B T}} + 1}. \quad (3.24)$$

At non-zero temperatures, Eq. (3.15) becomes [5]:

$$\Delta_k = -\sum_l V_{kl} u_l^* v_l [1 - 2f(E_l)] = -\sum_l V_{kl} \frac{\Delta}{2E_l} \tanh h\left(\frac{E_l}{2k_B T}\right) \quad (3.23)$$

Using Eq. (3.17) and again assuming that Δ is independent of the k direction, one can show that [5]:

$$\frac{1}{V} = \int_0^{\hbar\omega} \frac{\tanh\left(\frac{\sqrt{\xi^2 + \Delta^2}}{2k_B T}\right)}{\sqrt{\xi^2 + \Delta^2}} D(\xi) d\xi. \quad (3.24)$$

Equation (3.24) determines the superconducting gap as a function of temperature T . The critical temperature T_c is where the gap disappears, and the material turns into a regular metal. Substituting $\Delta = 0$ and $T = T_c$ into Eq. (3.24) gives [5]:

$$1 = VD_0 \int_0^{\hbar\omega} \frac{\tanh\left(\frac{\xi}{2k_B T_c}\right)}{\xi} d\xi. \quad (3.25)$$

In the weak-coupling limit $\hbar\omega \gg 2k_B T$, this gives [5]:

$$\frac{1}{VD_0} = \left(\ln\left(\frac{\hbar\omega}{2k_B T_c}\right) - \ln 0.44 \right) \quad (3.26)$$

and thus

$$k_B T_c = 1.136 \hbar\omega e^{\frac{-1}{VD_0}}. \quad (3.27)$$

Comparing Eq. (3.21) and Eq. (3.27), we find that the superconducting gap $\Delta(0)$ at $T=0$ and the critical temperature T_c are related by

$$\frac{\Delta(0)}{k_B T_c} = \frac{2}{1.13} = 1.764. \quad (3.28)$$

Thus in conventional BCS theory there is a direct correlation between the critical temperature T_c and the superconducting gap $\Delta(0)$.

3.2 Granular Aluminum Thin Films

Granular aluminum films are made up of small aluminum grains separated by thin insulating barriers of aluminum oxide (Al_2O_3). My research made use of granular aluminum thin films because their superconducting gap can be changed by altering the grain size.

In the late 1960s, researchers discovered surprising behavior of aluminum thin films grown in low-pressure oxygen [8]. In particular, these films showed enhanced superconducting critical temperature T_C . The key to this enhancement was the small size of the grains that were produced when small amounts of oxygen were present during the growth of the film.

Granular films are best described using the Ginzburg-Landau equation. This involves the parameter kappa κ , defined as the ratio of the penetration depth λ to the coherence length ξ . The parameter κ determines whether the superconductor will be Type-I ($\kappa < \frac{1}{\sqrt{2}}$) or Type-II ($\kappa > \frac{1}{\sqrt{2}}$) [4]. Pure aluminum is a Type-I superconductor, with a Ginzburg-Landau parameter κ approximately equal to 1.5×10^{-3} , which is much less than the Type-II threshold of $1/\sqrt{2}$.

However, κ increases when disorder is introduced. The effect of disorder can be quantified using the mean free path l for the scattering from structural defects or inhomogeneities. This scattering reduces the coherence length according to [4]:

$$\frac{1}{\xi} = \frac{1}{\xi_0} + \frac{1}{l}, \quad (3.29)$$

where ξ_0 is the coherence length in the absence of disorder. In the dirty limit $l \ll \xi_0$ the coherence length ξ is approximately equal to l , and the Ginzburg-Landau parameter κ becomes approximately equal to λ/l . This means that disorder can significantly increase κ , pushing the aluminum into the realm of Type-II superconductivity. This phenomenon has particular relevance for granular aluminum films. If the size of the aluminum grains is smaller than ξ_0 , it has been argued that this effectively reduces the coherence length [4], leading to an increase in κ and Δ .

Since 1960s, granular superconductors have been studied extensively. Although various models being put forth to explain their unconventional properties [9][10], there does not seem to be any agreement on the cause of the enhancement. The oxide layers between grains are generally understood to produce a highly non-uniform structure in the aluminum film. The oxygen causes thin insulating barriers to form between the grains. These barriers somewhat isolate each grain, turning them into individual islands of superconductivity within the film. As a result of the granular structure, each of the superconducting grains within a granular aluminum film could potentially exhibit a different critical temperature. This variation would be expected due to the differences in the size and separation of the grains, and the degree of disorder within the grains, all of which can influence the superconductivity state.

By manipulating the conditions under which the granular aluminum films are fabricated, such as the deposition rate, the oxygen content, or the substrate temperature, the grain characteristics and film properties can be tuned. Figure 3.1 shows an Atomic Force Microscope (AFM) topographic surface scan image of a granular Al thin film. This film was with 70 nm thick and grown using an oxygen doping pressure of 2.5 μ Torr during the evaporation. The grain size clearly varies, which may cause local variations in the gap. Such variations could also lead to spatial variations in the non-equilibrium quasiparticle density and prevent quasiparticles diffusing. I will present detailed results on transmons fabricated from granular aluminum in Chapter 5 and Chapter 7.

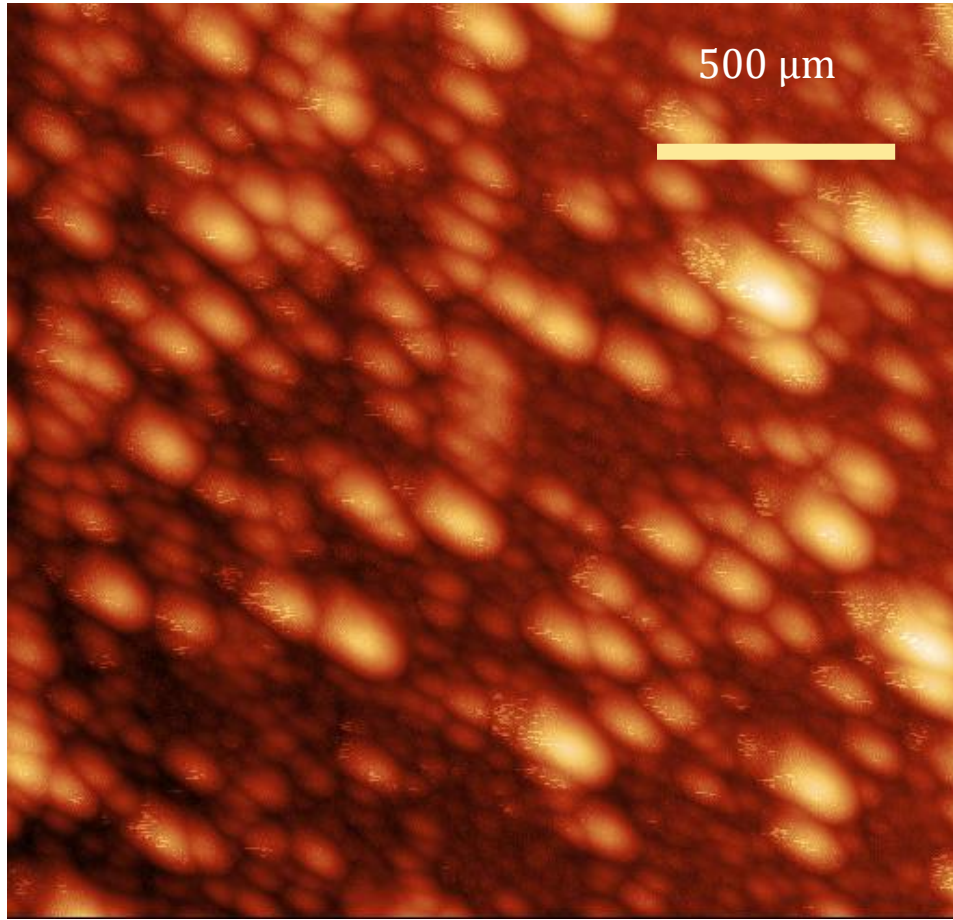


Figure 3.1: Topography of 70 nm thick granular Al film showing rough surface.

Chapter 4

Theory of Quasiparticle Behavior in Junctions that Have Different Gaps

In Chapter 2, I briefly discussed dissipation mechanisms that lead to relaxation of superconducting qubits. In this chapter, I will focus on the main topic of my research – relaxation due to quasiparticle tunneling. I will discuss theoretical modeling of quasiparticle induced loss and the behavior of non-equilibrium quasiparticles in junctions with electrodes that have different superconducting energy gaps. From the model, we find the temperature dependent density of quasiparticles and calculate the relaxation time of qubits. I will also discuss Multiple Andreev Reflection in the S-I-S junction and its impact on the relaxation of the transmon.

4.1 Quasiparticles

According to the BCS theory [1][2], superconductivity arises due to the formation of Cooper pairs [3] at low temperatures. These pairs consist of two electrons with opposite momentum and spin, which are bound together by an attractive interaction mediated by lattice vibrations (phonons). As discussed in Chapter 3, to break a Cooper pair requires a minimum energy of 2Δ , where Δ is the superconducting gap. For a superconductor in the weak-coupling BCS limit, the superconducting critical temperature T_c is related to the gap by the expression $\Delta = 1.76k_B T_c$. Pair breaking can be caused by thermal energy, a microwave drive that is sufficiently strong, optical illumination or the absorption of high energy particles such as cosmic rays.

4.1.1 Thermal Quasiparticles

The number of equilibrium thermal quasiparticles at temperature T is given by [4]

$$n_{thqp} = \int_{-\infty}^{+\infty} D(E)f(E)dE, \quad (4.1)$$

where $f(E) = 1/(e^{\frac{E-\mu}{k_B T}} + 1)$ is the Fermi distribution, μ is the chemical potential [5] and

$D(E)$ is the superconducting density states of the quasiparticles, given by

$$D(E) = \begin{cases} 2N_0 \frac{|E|}{\sqrt{E^2 - \Delta^2}}, & \text{for } |E| > \Delta \\ 0, & \text{for } |E| \leq \Delta \end{cases} \quad (4.2a)$$

$$(4.2b)$$

Here $N_0 = 3n_e/4\varepsilon_F$ is the density of states of the electrons of one spin in the normal metal, ε_F is the Fermi energy and n_e is the electron density [4]. Setting the chemical potential $\mu = 0$, the Eq.

(4.1) then gives

$$\begin{aligned} n_{thqp} &= 4N_0 \int_a^\infty \frac{E}{\sqrt{E^2 - \Delta^2}} \frac{1}{1 + e^{\frac{E}{k_B T}}} dE \\ &= 4N_0 \int_\Delta^\infty dE \frac{E}{\sqrt{E^2 - \Delta^2}} e^{-\frac{E}{k_B T}} \sum_{n=0}^{\infty} (-1)^n e^{-\frac{nE}{k_B T}}. \end{aligned} \quad (4.3)$$

In the last expression, a Taylor expansion has been used to evaluate $(1 + e^{E/k_B T})^{-1}$. In the limit

$E \sim \Delta \gg k_B T$, we get

$$\begin{aligned} n_{thqp} &\simeq 4N_0 k_B T \int_{\frac{\Delta}{k_B T}}^\infty \frac{x e^{-x}}{\sqrt{x^2 - \left(\frac{\Delta}{k_B T}\right)^2}} dx \\ &= 4N_0 k_B T e^{-\frac{\Delta}{k_B T}} \left(\int_0^\infty dy \frac{y^{\frac{1}{2}} e^{-y}}{\sqrt{y + \frac{2\Delta}{k_B T}}} + \frac{\Delta}{k_B T} \int_0^\infty dy \frac{y^{-\frac{1}{2}} e^{-y}}{\sqrt{y + \frac{2\Delta}{k_B T}}} \right). \end{aligned} \quad (4.4)$$

For $2\Delta/k_B T \gg 1$, the formula becomes [4]

$$n_{\text{thqp}} \approx \frac{4N_0(k_B T)^{\frac{3}{2}} e^{-\frac{\Delta}{k_B T}}}{\sqrt{2\Delta}} \left(\frac{\sqrt{\pi}}{2} + \frac{\Delta}{k_B T} \sqrt{\pi} \right) \quad (4.5)$$

Again, taking the limit $\Delta \gg k_B T$ gives

$$n_{\text{thqp}} = 2\sqrt{2\pi k_B T \Delta} N_0 e^{-\frac{\Delta}{k_B T}}. \quad (4.6)$$

Eq. (4.6) implies that there are practically no quasiparticles present if $T \ll \Delta/k_B$. For example, for aluminum $\Delta = 170\mu\text{eV}$ at $T = 20\text{ mK}$, one finds $n_{\text{thqp}} \sim 7 \times 10^{-37} \mu\text{m}^{-3}$.

4.1.2 Non-Equilibrium Quasiparticles

Quasiparticles may affect the performance of a wide range of superconducting devices. At small densities, one expects the effects to scale linearly with quasiparticle density. Unfortunately, it is difficult to directly measure the quasiparticle density. Instead, one is forced to use indirect measurement of quasiparticle density by measuring a property that depends on quasiparticle density, such as the relaxation time T_1 . The disadvantage of this approach is that relaxation has contributions from mechanisms that do not involve quasiparticles.

From published experiments the claimed fraction of broken Cooper pairs often falls in the range of $x_{qp} = 10^{-9}$ - 10^{-5} [5]-[9]. This is not a density, but an inferred fraction $x_{qp} = n_{\text{QP}}/n_{\text{CP}}$ which is the number of quasiparticles normalized by the number of Cooper pairs per unit volume. Most transmons are made of thin Al films and are thermally anchored to the mixing chamber of a dilution refrigerator around 20 mK. As discussed above, the expected density of thermally generated quasiparticles at such temperature is vanishingly small. For $\Delta \approx 170\mu\text{eV}$ for Al, we get $x_{qp} \approx 10^{-50}$. This is many orders of magnitude smaller than observed densities, the extra quasiparticles are called non-equilibrium quasiparticles.

Non-equilibrium quasiparticles could be caused by the absorption of infrared radiation or high frequency microwaves from higher temperature stages of the dilution refrigerator [10], photons traveling through the transmission lines [11], stray cosmic radiation [12], or background radioactivity [12]. In the steady state, the rate of excess quasiparticle creation will be balanced by recombination of the quasiparticles to Cooper pairs and trapping. Trapping can occur at normal defects and vortices. If trapping prevails over recombination, the overall quasiparticle density is simply given $n_{qp} = n_{neqp} + n_{thqp}$ [13].

In 1970, Owen and Scalapino [14] proposed a model for the distribution of non-equilibrium quasiparticles by defining an effective chemical potential μ^* in the Fermi distribution: $f(E - \mu, T) \rightarrow f(E - \mu^*, T)$. Except for this substitution, the theory is the same as the equilibrium theory. In particular, we can write

$$n_{qp} = 4N_0 \int_0^\infty D(\epsilon) \frac{d\epsilon}{1 + e^{\beta(\epsilon - \mu^*)}}, \quad (4.7)$$

where $\epsilon = \sqrt{E^2 + \Delta^2}$ and $\beta = (k_B T)^{-1}$.

In the low temperature limit when $T \ll T_c$, the non-equilibrium quasiparticle density becomes

$$n_{thqp} \simeq 2N_0 \sqrt{\frac{2\pi\Delta}{\beta}} e^{-\beta(\Delta - \mu^*)} \quad (4.8)$$

This can be solved for the effective chemical potential as a function of T and n_{neqp}

$$\mu^* \simeq k_B T * \ln \left(\frac{n_{neqp}}{2N_0 \sqrt{2\pi k_B T \Delta}} \right) + \Delta. \quad (4.9)$$

Parker proposed another model [15] where the nonequilibrium quasiparticle distribution results from an effective temperature T^* , *i.e.* $f(E, T) \rightarrow f(E, T^*)$. In this model,

$$\left(\frac{n_{qp}}{n_{thqp}}\right)^2 \cong \left(\frac{T^*}{T}\right)^3 \left(\frac{\int_{X_G^*}^{\infty} \frac{x^2 dx}{e^x - 1}}{\int_{X_G}^{\infty} \frac{x^2 dx}{e^x - 1}}\right), \quad (4.10)$$

where $X_G^* = \frac{2\Delta(T^*)}{k_B T^*}$ and $X_G = \frac{2\Delta(T)}{k_B T}$. Physically, The Parker model results in a population of “hot” quasiparticles with $T^* > T$, which the Owen and Scalapino model can give an equivalent density of “cold” quasiparticles at the ambient temperature T . Since hot and cold quasiparticles do not have the same distribution, the two models are not equivalent.

4.2 Quasiparticle Relaxation and Excitation with Regions that Have Different Gaps

From the BCS theory, one expects the density of thermal quasiparticles in a material increases when the temperature increases. From this, one would expect that the transmon relaxation time T_1 would decrease as the temperature increases. It was thus very surprising that the group of our collaborator, Rui Zhang [16], observed that some samples showed an increase in T_1 as temperature T increased from 30 to 100 mK.

In this section, this behavior is explained as arising from the behavior of non-equilibrium quasiparticles [17]-[19] when the junction electrodes have slightly different superconducting gaps. This explanation also suggests that deliberately engineering the gaps of the two electrodes may provide a way to increase the T_1 of transmon qubits.

Our transmons have two Al pads connected to the electrodes of a Josephson junction. The Al pads in combination with the junction itself give total capacitance C_Σ to the device. When properly chosen, this capacitance suppresses charge noise [20] and couples the device to the 3D superconducting Al cavity. Details of my transmon construction are covered in chapter 5.

To keep this discussion as simple as possible, I consider just the two lowest levels of the transmon and assume that the coupling strength g between the cavity and the qubit satisfied $g \ll 2\pi|f_c - f_{01}|$, where f_c is the cavity resonance frequency and f_{01} is the qubit's 0-to-1 transition frequency, this is the dispersive limit. From the discussion in section 2.6.1, the decay rate of an undriven transmon is [21]

$$1/T_1 = \Gamma_{1 \rightarrow 0} + \Gamma_{0 \rightarrow 1}, \quad (4.11)$$

where $\Gamma_{1 \rightarrow 0}$ is the rate at which the excited state relaxes back to the ground state and $\Gamma_{0 \rightarrow 1}$ is the rate at which the excited state is excited from the ground state due to energetic processes. I next assume that individual single quasiparticle tunneling through the junction is the main source causing relaxation, and in this case [22]

$$\Gamma_{1 \rightarrow 0} = \frac{E_c}{hf_{01}e^2} S_I(f_{01}), \quad (4.12)$$

where $S_I(f)$ is the current noise power spectral density of the quasiparticle tunneling current at frequency f . $S_I(f)$ is a double-sided quantum noise spectrum [21]. Positive frequencies cause downward transitions, while negative frequencies cause excitations. The upward transition rate is

$$\Gamma_{0 \rightarrow 1} = \frac{E_c}{hf_{01}e^2} S_I(-f_{01}) \quad (4.13)$$

The noise spectrum results from single quasiparticle tunneling through the junction is

$$S_I(f) = e(I_{L \rightarrow R} + I_{R \rightarrow L}). \quad (4.14)$$

Here $I_{L \rightarrow R}$ is the current from single quasiparticle tunneling from the left to the right electrode and $I_{R \rightarrow L}$ is the corresponding current from quasiparticle tunneling from the right to the left electrode at voltage $V = hf/e$. A physical picture for this behavior is that transmon relaxation results when energy hf_{01} is transferred from the transmon to quasiparticles that tunnel through the junction.

To calculate the quasiparticle currents $I_{L \rightarrow R}$ and $I_{R \rightarrow L}$, we have to carefully consider the physical layout of our transmons. Our transmons are fabricated using a double-angle evaporation technique [23] that involves depositing two thin-film aluminum (Al) layers to create a Josephson junction, as depicted in Fig. 4.1. Fabrication begins with the deposition of the first Al layer onto a sapphire substrate, followed by oxidation to form a thin AlO_x tunnel barrier. Subsequently, the second Al layer is deposited on top of the first layer using an e-beam resist-bridge stencil, resulting in a precisely defined junction with small overlap between the two layers. It is important to note that the two Al layers can have different thicknesses, and variations in the growth conditions can lead to significant variations in their superconducting gaps [24]-[27].

I will assume that the first layer has a superconducting gap Δ_1 and this forms the left electrode (See Fig. 4.1). The second layer and right electrode has a superconducting gap Δ_2 . This electrode connects to the right pad of the transmon. Note that both the right and left side of the device have two layers. I denote the volume of the first and second layer on the right to be Ω_{1R} and Ω_{2R} , respectively. To ensure coverage, the second layer is approximately twice as thick as the first layer and the left and right side volumes are vertically same. Then we have the approximate volume relations $\Omega_{1L} \approx \Omega_{1R} \approx \Omega_{2R}/2 \approx \Omega_{2L}/2$. As we will see, the relative volumes of the layers may play a significant role in the temperature dependence of quasiparticle induced relaxation phenomenon.

For the devices I built and measured, $hf_{01} \ll \Delta_1, hf_{01} \ll \Delta_2$. I will also assume that non-equilibrium quasiparticles are generated in the junction electrodes by an external source that breaks pairs such as strong radiation. In addition, I assume that the quasiparticles in each pad have thermalized to the substrate's temperature T and that the two layers in each pad are in good diffusive contact. These assumptions imply that the non-equilibrium quasiparticles in each region

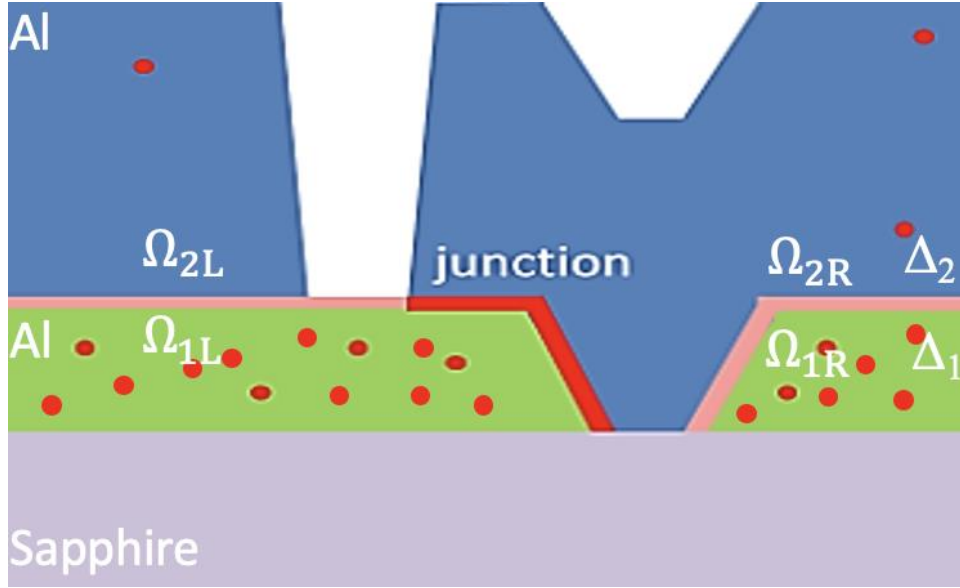


Figure 4.1: Schematic view of the Al/AIOx/Al Josephson junction. The junction is made of two Al layers - a thinner layer 1 (green) with superconducting gap Δ_1 and a thicker layer 2 (blue) with gap Δ_2 and connects the Ω_{1L} region on the left and Ω_{2R} region on the right.

will still have a Fermi-Dirac distribution: $f_{FD}(E)$ and obey $f_{FD}(-E) = 1 - f_{FD}(E)$. Under this assumption, quasiparticles with $E > 0$ quasi electrons and $E < 0$ quasi holes will both contribute to the current noise. From Eq. (4.14), the noise which is at frequency f is related to $I_{L \rightarrow R}$ and $I_{R \rightarrow L}$ at an applied voltage $V = hf/e$. From Tinkham, for an ideal tunnel junction in the low transparency limit [4], the current can be written as:

$$I_{L \rightarrow R} = \frac{2}{eR_n} \int_0^\infty \frac{|E|\theta(E - \Delta_1)}{\sqrt{E^2 - \Delta_1^2}} \frac{|E + hf|\theta(E + hf - \Delta_2)}{\sqrt{(E + hf)^2 - \Delta_2^2}} f_{FD}(E, \mu_{1L})(1 - f_{FD}(E + hf, \mu_{2R}))dE, (4.15)$$

where R_n is the normal-state tunneling resistance of the junction, $\theta(E)$ is the Heaviside step function, E is the quasiparticle energy, and μ_{1L} and μ_{2R} are the chemical potential for the $E > 0$ quasiparticles on the left side of region 1 and right side of region 2, respectively.

From the previous discussion, the density of quasiparticles in the system is determined by the chemical potential [28]. For the left side of region 1, the density of quasiparticles is [16]

$$\begin{aligned} n_{1L} &= 4N_0 \int_{\Delta_1}^{\infty} \frac{E}{\sqrt{E^2 - \Delta_1^2}} f_{FD}(E, \mu_{1L}) dE \\ &= 4N_0 \Delta_1 \sum_{n=1}^{\infty} (-1)^{n+1} e^{\frac{n\mu_{1L}}{k_B T}} K_1\left(\frac{n\Delta_1}{k_B T}\right) \end{aligned} \quad (4.16)$$

where K_1 is the modified Bessel function, $N_0 = 3n_e/4\varepsilon_F$ is the single-spin density of electron states in the normal state at the Fermi level, n_e is the electron density, and ε_F is the Fermi energy. The density n_{2R} of quasiparticles of layer 2 on the right is obtained by changing Δ_1 to Δ_2 and μ_{1L} to μ_{2R} in Eq. (4.16).

The next step is to calculate the noise spectrum from the junction currents by evaluating Eq. (4.14) with positive frequencies. My junctions were designed so that $\Delta_1 < \Delta_2$, $\Delta_2 - \Delta_1 < hf_{01}$, $\Delta_1 - \mu_{1L} \gg k_B T$ and $\Delta_2 - \mu_{2R} \gg k_B T$. Unfortunately, some of my junctions did not meet these design goals. Nevertheless, if these constraints are satisfied, then

$$I_{L \rightarrow R} \approx \frac{\alpha(\Delta_1, \Delta_2) n_{1L}}{eR_n} \frac{1}{2N_0} \left[1 - \frac{e^{\frac{(\Delta_1 - \Delta_2 + hf_{01})}{k_B T}}}{\sqrt{\pi k_B T \Delta_2}} \beta \frac{n_{2R}}{8N_0} \right], \quad (4.17)$$

where [16]:

$$\alpha(\Delta_1, \Delta_2) = \frac{\Delta_1 + hf_{01} + z_0 k_B T}{\sqrt{(\Delta_1 + hf_{01} + z_0 k_B T)^2 - \Delta_2^2}} \quad (4.18)$$

and

$$\beta(\Delta_1, \Delta_2) = \frac{\sqrt{2\Delta_2 + z_0 k_B T} (2\Delta_1 + z_0 k_B T)^{\frac{3}{2}}}{(\Delta_2 + z_0 k_B T) (\Delta_1 + z_0 k_B T)} \frac{\sqrt{\Delta_2}}{\sqrt{4\Delta_1 + z_0 k_B T}} \approx 2. \quad (4.19)$$

The quantity $z_0 k_B T$ acts like an effective thermal energy of the quasiparticles. Applying different values of z_0 for Eq. (4.18) and comparing to the numerical integration of Eq. (4.15), we find that $z_0 = 0.3$ provides a good approximation for typical parameters. Similarly, the current $I_{R \rightarrow L}$ can be obtained by exchanging the subscripts 1 and 2 and 1L and 2R everywhere in Eqs. (4.17), (4.18) and (4.19).

Using Eqs. (4.13) and (4.16), one finds [16],

$$S_l(f_{01}) \approx \frac{1}{R_n N(0)} \left[\frac{\alpha(\Delta_1, \Delta_2)}{2} n_{1L} + \frac{\alpha(\Delta_2, \Delta_1)}{2} n_{2R} \right]. \quad (4.20)$$

Combining Eqs. (4.13) and (4.20) yields

$$\Gamma_{1 \rightarrow 0} \approx \frac{1}{\tau_0 n_e} \left[\frac{\alpha(\Delta_1, \Delta_2)}{2} n_{1L} + \frac{\alpha(\Delta_2, \Delta_1)}{2} n_{2R} \right], \quad (4.21)$$

where

$$\tau_0 = 3R_n C \left(\frac{\hbar f_{01}}{2\varepsilon_F} \right). \quad (4.22)$$

A similar analysis of the excitation rate, which corresponds to negative frequencies in Eq. (4.20), gives

$$\Gamma_{0 \rightarrow 1} \approx \frac{e^{-\frac{\hbar f_{01}}{k_B T}}}{\tau_0 n_e} \left[\frac{\gamma(\Delta_1, \Delta_2)}{2} n_{1L} e^{-\frac{(\Delta_2 - \Delta_1)}{k_B T}} + \frac{\gamma(\Delta_2, \Delta_1)}{2} n_{2R} e^{-\frac{(\Delta_1 - \Delta_2)}{k_B T}} \right], \quad (4.23)$$

where

$$\gamma(\Delta_1, \Delta_2) = \alpha(\Delta_1, \Delta_2) \frac{(\Delta_2 + z_0 k_B T) \sqrt{2\Delta_1 + z_0 k_B T}}{\sqrt{2\Delta_2 + z_0 k_B T} (\Delta_1 + z_0 k_B T)}. \quad (4.24)$$

Using Eq. (4.11) (4.21) and (4.23), we can rewrite the relaxation time as [16]:

$$T_1 \approx \frac{2\tau_0 n_e}{\left[\alpha(\Delta_1, \Delta_2) + \gamma(\Delta_1, \Delta_2) e^{-\frac{(\Delta_2 - \Delta_1 + hf_{01})}{k_B T}} \right] n_{1L} + \left[\alpha(\Delta_2, \Delta_1) + \gamma(\Delta_2, \Delta_1) e^{-\frac{(\Delta_1 - \Delta_2 + hf_{01})}{k_B T}} \right] n_{2R}}. \quad (4.25)$$

If $\Delta_1 = \Delta_2 = \Delta$, this expression becomes

$$T_1 \approx \frac{\sqrt{(\Delta + hf_{01} + z_0 k_B T)^2 - \Delta^2}}{\left(1 + e^{-\frac{hf_{01}}{k_B T}} \right) (\Delta + hf_{01} + z_0 k_B T)} \frac{2\tau_0 n_e}{(n_{1L} + n_{2R})}. \quad (4.26)$$

From Eq. (4.26), we can see that the relaxation time scales inversely with the average quasiparticle density n_{1L} and n_{2R} . Taking a different limit, $k_B T \ll \Delta_2 - \Delta_1 < hf_{01}$, the non-equilibrium quasiparticles will tend to accumulate in layer 1, since the gap of layer 1 is smaller than the gap of layer 2. In this case we will tend to have $n_{2R} \ll n_{1L}$ and the relaxation time reduces to

$$T_1 \approx \frac{2\tau_0 n_e}{\alpha(\Delta_1, \Delta_2) n_{1L}}. \quad (4.27)$$

As a result, at sufficiently low temperatures, we expect the relaxation time to scale inversely with the quasiparticle density in the junction's low-gap electrode.

4.3 Modeling Quasiparticle Density

From the previous discussion, one can see that T_1 depends on n_{1L} and n_{2R} . To find how T_1 depends on temperature, we have to find how the quasiparticle densities n_{1L} and n_{2R} depend on temperature. To do so, we need to account for the non-equilibrium and equilibrium quasiparticles.

It is unknown if our transmons' nonequilibrium pair-breaking is driven by high-energy phonons, infrared photons, optical photons, or other processes [29]-[31]. To keep things simple, I assume that there is a constant, temperature-independent source that generates non-equilibrium

quasiparticles at a steady rate in layer 1 (which is directly in contact with the substrate) in both the left and right transmon pads. I also assume that the quasiparticles are thermalized to the substrate's temperature T and that the two layers in each pad are in good diffusive contact.

In order to model the behavior of quasiparticles in a Josephson junction that has regions with different gaps, I also made the following assumptions:

- (1) The left side of the junction is formed from contact to layer 1L, which has small volume Ω_{1L} with low gap Δ_1 . Above this in layer 2L, which has large volume Ω_{2L} with high gap Δ_2 .
- (2) The right side of the junction is formed from high gap Δ_2 and large volume Ω_{2R} . Beneath this is layer 1R with small volume $\Omega_{1R} = \Omega_{1L}$ and gap Δ_1 .
- (3) The junction only contacts the low gap region on the left side and the high gap region on the right side.
- (4) I neglect the transfer of quasiparticles across the junction when calculating the steady state density of quasiparticles in the different layers. This should be a good approximation since the contact between layers 1 and 2 is much larger than the junction area.
- (5) On each side of the junction, layer 1 can easily exchange quasiparticles with layer 2.
- (6) Nonequilibrium quasiparticles are only created on each side of the junction in layer 1, which we assume is in contact with the substrate.
- (7) We ignore quasiparticle recombination and instead assume that quasiparticles are captured by normal-metal inclusions, interfaces, vortices or other deviations from bulk superconductivity.

With these assumptions, the net rate of quasiparticle generation in the two layers on the left can be written as:

$$\frac{dN_{1L}}{dt} = G_{p1} + G_{g1} - G_{tr,1L}N_{1L} - G_{L,1\rightarrow 2}A_L \frac{N_{1L}}{\Omega_{1L}} + G_{L,2\rightarrow 1}A_L \frac{N_{2L}}{\Omega_{2L}} \quad (4.28a)$$

$$\frac{dN_{2L}}{dt} = G_{g2} - G_{tr,2L}N_{2L} - G_{L,2\rightarrow 1}A_L \frac{N_{2L}}{\Omega_{2L}} + G_{L,1\rightarrow 2}A_L \frac{N_{1L}}{\Omega_{1L}}. \quad (4.28b)$$

Here N is the number of quasiparticles in the region with the subscript, A_L is the contact area between the two layers on the left, G_{p1} is the rate at which non-equilibrium quasiparticles are generated in layer 1, G_{gj} is the rate at which quasiparticles are generated thermally in layer j , G_{tr} is the rate at which quasiparticles are trapped in the indicated region, and $G_{L,i\rightarrow j}$ is the rate at which quasiparticles escape from layer i and g to j on the left. We obtain the steady state number of quasiparticles in region 1 on left by setting the derivatives in Eq. (4.28) to zero, which yields [16]

$$N_{1L} = \frac{\left(\frac{G_{p1}}{G_{tr,1L}} + \frac{G_{g1}}{G_{tr,1L}}\right) + \frac{G_{L,2\rightarrow 1}}{G_{tr,2L}} \frac{A_L}{\Omega_{2L}} \left(\frac{G_{p1}}{G_{tr,1L}} + \frac{G_{g1}}{G_{tr,1L}} + \frac{G_{g2}}{G_{tr,1L}}\right)}{1 + \frac{G_{L,2\rightarrow 1}}{G_{tr,2L}} \frac{A_L}{\Omega_{2L}} + \frac{G_{L,1\rightarrow 2}}{G_{tr,1L}} \frac{A_L}{\Omega_{1L}}}. \quad (4.29)$$

It is helpful to consider some limits of Eq. (4.29) to understand this expression. When T goes to zero, the thermal generation terms G_{g1} and G_{g2} are zero. Setting the transfer rates $G_{L,2\rightarrow 1}$ and $G_{L,1\rightarrow 2}$ to zero for disconnected regions, we obtain

$$N_{1L} = G_{p1}/G_{tr,1L} \equiv N_{ne,1L}. \quad (4.30)$$

Here we introduce the parameter $N_{ne,1L}$ to describe the number of non-equilibrium quasiparticles in the steady state at zero temperature in region 1 on the left if it was disconnected from all other regions. Similarly the number of thermal quasiparticles in the two regions on the left to be identified as

$$N_{th,1L} \equiv G_{g1}/G_{tr,1L} \quad (4.31)$$

and

$$N_{th,2L} \equiv G_{g2}/G_{tr,2L}. \quad (4.32)$$

Different kinds of quasiparticle traps, such as normal metal inclusions, normal metal surface layers, normal metal interfaces, and trapped flux vortices, will result in trapping rates that scale differently with the thickness, area and volume of the region. For simplicity I will assume that the trapping is due to magnetic flux vortices that penetrate both layers of the sample. If each vortex acts like a cylinder with a surface trapping area of

$$A_v = 2\pi r_v h_j, \quad (4.33)$$

where r_v is the effective radius of the vortex and h_j is the thickness of layer j . Then the total rate at which quasiparticles are trapped in region 1L is then

$$G_{tr,1L} N_{1L} = \frac{N_{1L}}{\Omega_{1L}} v 2\pi r_v h_j N_{v1}, \quad (4.34)$$

where v is the speed of the quasiparticles and N_{v1} is the number of vortices. Since layer 1 is on top of layer 2, I assume they have the same number of vortices, $N_{v1} = N_{v2}$. The trapping rate in region 2L is then:

$$G_{tr,2L} N_{2L} = \frac{N_{2L}}{\Omega_{2L}} v (2\pi r_v h_2) N_{v1}. \quad (4.35)$$

Combining these two equations gives

$$\frac{G_{tr,1L}}{G_{tr,2L}} = \frac{\Omega_{2L}}{\Omega_{1L}} \frac{v(2\pi r_v h_1) N_{v1}}{v(2\pi r_v h_2) N_{v1}} = \frac{\Omega_{2L}}{\Omega_{1L}} \frac{h_1}{h_2} = \frac{A_{2L}}{A_{1L}} = 1, \quad (4.36)$$

Notice that $A_{2L} = A_{1L}$ is the planar area of layers 1 and 2 on the left.

I can now rewrite the general expression for N_{1L} in Eq. (4.29) as:

$$N_{1L} = \frac{(N_{ne,1L} + N_{th,1L}) + \frac{G_{L,2 \rightarrow 1}}{G_{tr,1L}} \frac{A_L}{\Omega_{2L}} (N_{ne,1L} + N_{th,1L} + N_{th,2L})}{1 + \frac{G_{L,2 \rightarrow 1}}{G_{tr,1L}} \frac{A_L}{\Omega_{2L}} + \frac{G_{L,1 \rightarrow 2}}{G_{tr,1L}} \frac{A_L}{\Omega_{1L}}}. \quad (4.37)$$

If the trapping rate is relatively slow compared to exchange rate from layer 2 to layer 1, then:

$$G_{L,2 \rightarrow 1} \frac{A_L}{\Omega_{1L}} > G_{L,2 \rightarrow 1} \frac{A_L}{\Omega_{2L}} \gg G_{tr,1L}. \quad (4.38)$$

Equation (4.37) then reduce to:

$$N_{1L} \approx \frac{1}{1 + \frac{G_{L,1 \rightarrow 2} \Omega_{2L}}{G_{L,2 \rightarrow 1} \Omega_{1L}}} (N_{ne,1L} + N_{th,1L} + N_{th,2L}). \quad (4.39)$$

In thermal equilibrium there will be just as many quasiparticles flowing from 1 to 2 as from 2 to 1 so that,

$$G_{L,1 \rightarrow 2} A_L \frac{N_{th,1L}}{\Omega_{1L}} = G_{L,2 \rightarrow 1} A_L \frac{N_{th,2L}}{\Omega_{2L}}, \quad (4.40)$$

which yields

$$\frac{G_{L,1 \rightarrow 2} \Omega_{2L}}{G_{L,2 \rightarrow 1} \Omega_{1L}} = \frac{N_{th,2L}}{N_{th,1L}}. \quad (4.41)$$

Next consider the thermally generated quasiparticles in region 1L. Setting $\mu = 0$ in Eq. (4.16), we have

$$N_{th,1L} \approx 2N(0)\Omega_{1L}\sqrt{2\pi k_B T \Delta_1} e^{-\frac{\Delta_1}{k_B T}}. \quad (4.42)$$

Region 2L has a similar expression. Equation (4.39) then becomes:

$$N_{1L} \approx \frac{\Omega_{1L}\sqrt{\Delta_1} e^{-\frac{\Delta_1}{k_B T}}}{\Omega_{1L}\sqrt{\Delta_1} e^{-\frac{\Delta_1}{k_B T}} + \Omega_{2L}\sqrt{\Delta_2} e^{-\frac{\Delta_2}{k_B T}}} (N_{ne,1L} + N_{th,1L} + N_{th,2L}). \quad (4.43)$$

From this result, the density of quasiparticles in region 1 with left becomes:

$$n_{1L} \approx n_{th,1} + \left(\frac{\Omega_{1L}\sqrt{\Delta_1} e^{-\frac{\Delta_1}{k_B T}}}{\Omega_{1L}\sqrt{\Delta_1} e^{-\frac{\Delta_1}{k_B T}} + \Omega_{2L}\sqrt{\Delta_2} e^{-\frac{\Delta_2}{k_B T}}} \right) n_{ne,1L}, \quad (4.44)$$

where $n_{th,1} = N_{th,1L}/\Omega_{1L}$ is the density of thermally generated quasiparticles in layer 1. We assume there is the same density in regions 1L and 1R. A similar analysis gives the quasiparticle density in region 2R as:

$$n_{2R} \approx n_{th,2} + \left(\frac{\Omega_{2R}\sqrt{\Delta_2}e^{-\frac{\Delta_2}{k_B T}}}{\Omega_{1R}\sqrt{\Delta_1}e^{-\frac{\Delta_1}{k_B T}} + \Omega_{2R}\sqrt{\Delta_2}e^{-\frac{\Delta_2}{k_B T}}} \right) \left(\frac{\Omega_{1R}}{\Omega_{2R}} \right) n_{ne,1R}. \quad (4.45)$$

I note that this assumes that non-equilibrium quasiparticles are only being generated in layer 1.

4.4 Andreev Reflection

4.4.1 Introduction of Andreev Reflection

Andreev reflection [32] of quasiparticles play a significant role in quasiparticle tunneling in junctions that have barriers with non-zero transparency.

Andreev reflections are most easily understood at a superconductor-normal metal (S-N) interface. Suppose an electron with energy E (measured from ϵ_F) that is less than the superconducting gap Δ approaches an S-N boundary from the normal metal side. In this situation, the electron can't enter the superconductor due to the lack of available quasiparticle states matching its energy. Instead, the incoming electron is reflected back into its normal metal as a hole and a Cooper pair enters the superconductor (see Fig. 4.2). This ‘‘Andreev reflection’’ process conserves both charge and momentum.

In contrast to regular reflections, which decrease the transport current through the junction, Andreev reflections lead to an increase in the conductance around zero bias [32]. The amount of Andreev reflection is affected by the height and width of the potential barrier between the superconductor and the normal metal. For instance, a fully transparent barrier (strength $Z=0$ or

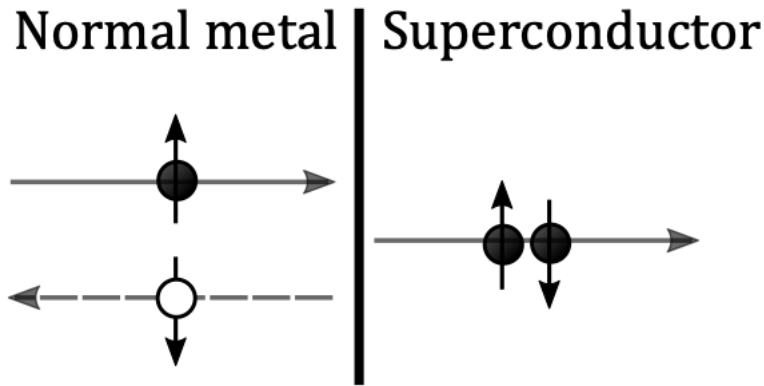


Figure 4.2: The process of Andreev reflection in S-N interface. Black and white circles represent electrons and holes, respectively. The horizontal arrows represent the momentum. The vertical arrows represent the spin.

transparency $D=1$) will have a large contribution from Andreev reflections. Increasing barrier strength (denoted by a higher Z value, a small transparency D) suppresses Andreev reflections, causing the current-voltage characteristic to resemble that of a conventional normal-insulator-superconductor (N/I/S) tunnel junction [32].

4.4.2 BTK Model with S-N Junction

The Blonder-Tinkham-Klapwijk (BTK) model [33] provides a convenient method for including Andreev reflections when finding the I-V curves of N/S interfaces. Their model is based on the generalized semiconductor model using the Bogoliubov-de Gennes (BdG) equations. To deal with the interface, they included a potential barrier and matched the wavefunctions at the interface to find the transmission and reflection coefficients.

Starting from my discussion in Chapter 3, we can rewrite Eq. (3.6) and get the one-dimensional Bogoliubov equation [4][33] for the superconducting side of the junction:

$$\begin{pmatrix} -\frac{\hbar^2}{2m}\frac{\partial^2}{\partial x^2} - \mu + H_0\delta(x) & \Delta(x) \\ \Delta^*(x) & \frac{\hbar^2}{2m}\frac{\partial^2}{\partial x^2} + \mu - H_0\delta(x) \end{pmatrix} \begin{pmatrix} u(x) \\ v(x) \end{pmatrix} = E \begin{pmatrix} u(x) \\ v(x) \end{pmatrix}. \quad (4.46)$$

There is no superconducting gap on the normal metal side, so Eq. (4.46) becomes simply:

$$\begin{pmatrix} -\frac{\hbar^2}{2m}\frac{\partial^2}{\partial x^2} - \mu & 0 \\ 0 & \frac{\hbar^2}{2m}\frac{\partial^2}{\partial x^2} + \mu \end{pmatrix} \begin{pmatrix} u(x) \\ v(x) \end{pmatrix} = E \begin{pmatrix} u(x) \\ v(x) \end{pmatrix}. \quad (4.47)$$

The eigenvalues for the energy E in the normal metal side can be found from Eq. (4.47) and one finds simply:

$$E = + \sqrt{\left(\frac{\hbar^2 k^2}{2m} - \mu\right)^2}, \quad (4.48)$$

where $\mu = \hbar^2 k_F^2/2m$ is the Fermi energy. We then have two solutions: one corresponds to an electron with wavevector \bar{k}_e such that $|\bar{k}_e| > k_F$ and energy $E = \frac{\hbar^2 k_e^2}{2m} - \mu$. The other solutions correspond to a hole which has a wavevector \bar{k}_h such that $|\bar{k}_h| < k_F$ and energy $E = -\frac{\hbar^2 k_h^2}{2m} + \mu$.

The wavefunctions corresponding to these solutions are:

$$\Psi_e(x) = \begin{pmatrix} 1 \\ 0 \end{pmatrix} e^{\pm i k_e x}, \quad \text{where } k_e = \sqrt{\frac{2m}{\hbar^2}(E + \mu)} \quad (4.49a)$$

$$\Psi_h(x) = \begin{pmatrix} 0 \\ 1 \end{pmatrix} e^{\pm i k_h x}, \quad \text{where } k_h = \sqrt{\frac{2m}{\hbar^2}(\mu - E)} \quad (4.49b)$$

On the superconducting side, Eq. (4.46) gives eigenvalues of energy

$$E = + \sqrt{\left(\frac{\hbar^2 q^2}{2m} - \mu\right)^2 + \Delta^2}, \quad (4.50)$$

noticed that Eq. (4.50) implies that $\sqrt{E^2 - \Delta^2} = \frac{\hbar^2 q_e^2}{2m} - \mu$. For $q_e > k_F$, one finds $\sqrt{E^2 - \Delta^2} = -\frac{\hbar^2 q_h^2}{2m} + \mu$, which gives the solution for quasi-electrons, which the hole case occurs for $q_h < k_F$.

The wavefunctions for quasiparticles on the superconducting side can then be written as:

$$\Psi_e(x) = \begin{pmatrix} u_0 \\ v_0 \end{pmatrix} e^{\pm i q_e x}, \text{ where } q_e = \sqrt{\frac{2m}{\hbar^2} (\sqrt{E^2 - \Delta^2} + \mu)} \quad (4.51a)$$

$$\Psi_h(x) = \begin{pmatrix} v_0 \\ u_0 \end{pmatrix} e^{\pm i q_h x}, \text{ where } q_h = \sqrt{\frac{2m}{\hbar^2} (\mu - \sqrt{E^2 - \Delta^2})}. \quad (4.51b)$$

Using Eq. (4.51) into Eq. (4.46), we find:

$$u_0 = \sqrt{\frac{1}{2} \left(1 + \frac{\sqrt{E^2 - \Delta^2}}{E} \right)} \quad (4.52)$$

$$v_0 = \sqrt{\frac{1}{2} \left(1 - \frac{\sqrt{E^2 - \Delta^2}}{E} \right)}. \quad (4.53)$$

Given Eqs. (4.49) and (4.51) for the wavefunctions, we can assume that when an S-N interface is present there will be incident and reflected waves. For an incident electron wave function which comes from the normal metal (left) electrode towards the interface S-N, I can write:

$$\Psi_{\text{in}}(x) = \frac{1}{\sqrt{v_e}} \begin{pmatrix} 1 \\ 0 \end{pmatrix} e^{i k_e x}. \quad (4.54)$$

This incident wave will be reflected back to the normal left side as two left-moving waves corresponding to both an electron and a hole. Note that the momentum of a left moving hole is the negative of a left moving electron [33], and we have [33]:

$$\Psi_r(x) = \frac{r_{ee}}{\sqrt{v_e}} \begin{pmatrix} 1 \\ 0 \end{pmatrix} e^{-i k_e x} + \frac{r_{he}}{\sqrt{v_h}} \begin{pmatrix} 0 \\ 1 \end{pmatrix} e^{+i k_h x}, \quad (4.55)$$

where r_{ee} is the amplitude of the electron's reflection coefficient, r_{he} is the amplitude of the Andreev reflection coefficient of the holes from incident electrons [33] and $v_e \simeq v_h \simeq v_F$ is the Fermi velocity on the left side.

On the right side of the interface (the superconductor), the transmitted wave consists of right-moving electron-like quasiparticles and right-moving hole-like quasiparticles and we can write the wave function as:

$$\Psi_{\text{tr}}(x) = \frac{t_{ee}}{\sqrt{w_e}} \begin{pmatrix} u_0 \\ v_0 \end{pmatrix} e^{+iq_e x} + \frac{t_{he}}{\sqrt{w_h}} \begin{pmatrix} v_0 \\ u_0 \end{pmatrix} e^{-iq_h x}, \quad (4.56)$$

where t_{ee} is the amplitude of the electron transmission coefficient and t_{he} is the amplitude of the hole transmission coefficient [33]. Note that in Eq. (4.56) w_e and w_h are the quasiparticle velocities. To find the velocity of the quasiparticles in superconducting electrode, we use the relation $v = \frac{1}{\hbar} \left| \frac{dE}{dk} \right|$ to obtain:

$$w_e = \frac{\sqrt{E^2 - \Delta^2} \hbar q_e}{E} \frac{1}{m} \quad (4.57a)$$

$$w_h = \frac{\sqrt{E^2 - \Delta^2} \hbar q_h}{E} \frac{1}{m} \quad (4.57b)$$

Blonder *et al.* [37] solved the quasiparticle velocities using a semiclassical approximation. The approximation is based on that E and Δ are relatively small compared to the Fermi energy μ . This gives:

$$w_e \approx w_h \approx \frac{\sqrt{E^2 - \Delta^2} \hbar k_f}{E} \frac{1}{m} \quad (4.58)$$

By matching the wave functions and their slope at the S-N interface, we can get the four coefficients [33]:

$$r_{he} = \frac{u_0 v_0}{u_0^2 + Z^2(u_0^2 - v_0^2)} \quad (4.59a)$$

$$r_{ee} = \frac{(Z^2 + iZ)(v_0^2 - u_0^2)}{u_0^2 + Z^2(u_0^2 - v_0^2)} \quad (4.59b)$$

$$t_{ee} = \frac{(1 - iZ)u_0\sqrt{u_0^2 - v_0^2}}{u_0^2 + Z^2(u_0^2 - v_0^2)} \quad (4.59c)$$

$$t_{he} = \frac{iZv_0\sqrt{u_0^2 - v_0^2}}{u_0^2 + Z^2(u_0^2 - v_0^2)} \quad (4.59d)$$

where the barrier height parameter is defined as [33]:

$$Z = \frac{H_0 m}{\hbar^2 k_f} = \frac{H_0}{\hbar v_f}. \quad (4.60)$$

Blonder *et al.* next defined the transmission and reflection coefficients from Eq. (4.59): $A = |r_{he}|^2$ is the probability of Andreev reflection, $B = |r_{ee}|^2$ is the ordinary reflection probability of electrons, $C = |t_{ee}|^2$ is the transmission probability of electrons without branch crossing while $D = |t_{he}|^2$ is the transmission of the holes with branch crossing. Note that if $E < \Delta$, we will have $C = D = 0$ [33].

The concept of “branch crossing” that was introduced by Blonder *et al.* [33] arises from the existence of four mechanisms that contribute to current through an S-N interface. The first contribution is due to electrons that travel to the S-N contact from the normal side. Such electrons may be Andreev reflected as holes or normally reflected as electrons, or may result in quasiparticles that are transmitted to the superconducting side. The second contribution is caused by holes in the N side that impinge on the S-N interface. The third contribution is from electron-like quasiparticles originating on the superconducting side and transferring electrons or holes to the normal side. The last process involves hole-like quasiparticles in the superconductor that are incident on the S-N interface. To obtain the overall current, we simply add the currents from each process. Blonder *et al.* find:

$$I = 2N(0)ev_f\sigma \int_{-\infty}^{\infty} [f_0(E - eV) - f_0(E)](1 + A(E) - B(E))dE. \quad (4.61)$$

Here $N(0)$ is the single spins density of states at the Fermi energy of the electrons in the normal metal side.

4.4.3 Multiple Andreev Reflection in S-I-S junctions

Equation (4.61) is for the current in an S-N junction. For transmons, we are interested in S-I-S junctions. The effects produced by Andreev reflection become quite complex in S-I-S junctions because of the phenomena of Multiple Andreev Reflections (MAR) [34]. Here I discuss what happens in superconducting junctions (S-I-S) under a finite voltage and describe bias how a quasiparticle may undergo multiple Andreev reflections. During each Andreev reflection, charge of $\pm 2e$ is transferred across the junction, and the quasiparticle gains or loses an energy of $2eV$ (where V is the voltage across the junction). After n such Andreev reflections, a quasiparticle may have acquired enough energy to enter one of the superconducting electrodes.

In the following discussion, I mainly follow the approach of Averin and Bardas [34]. Their discussion is particularly clear and describes the current-voltage characteristics of a single S-I-S superconducting channel with arbitrary transmission [34]-[37].

Figure 4.3 illustrates my version of the AB model of an S-I-S junction. This model is essentially an S-N-I-N-S junction. The left lead in this model is a superconductor with gap Δ_1 , while the right lead is a superconductor with gap Δ_2 . For my research, I am interested in the case where $\Delta_1 \neq \Delta_2$. A_n, B_n, C_n and D_n are the amplitudes of the electron and hole wavefunctions in

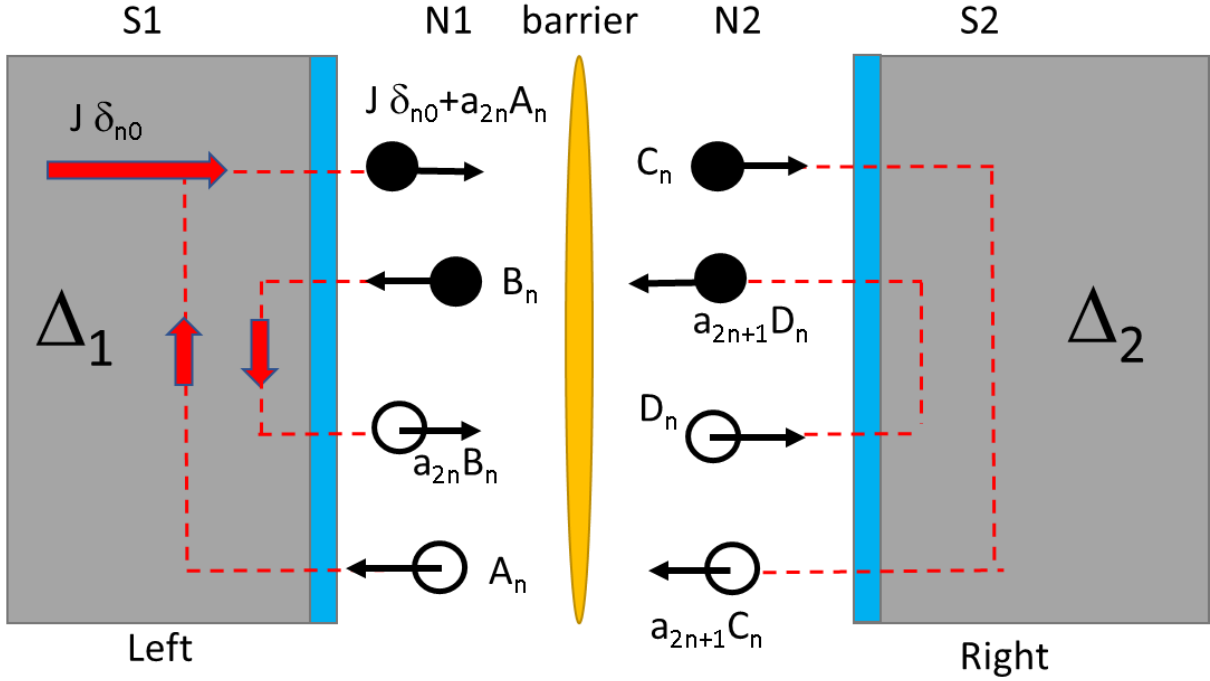


Figure 4.3: Illustration of Andreev reflections process that occur in a model of an SIS tunnel junction. The model has two S/N interfaces. An electron-like quasiparticle enters from the left electrode. A_n and B_n represent rightward and leftward moving electron amplitudes and C_n and D_n represent the amplitudes of leftward and rightward moving holes. The label n represents the net number of Andreev reflections. a_n is the n -th reflection amplitude.

the left and right normal regions. In the middle of the junction is a tunnel barrier where electrons or holes are reflected or transmitted. A barrier that is entirely transparent will have transparency $D = 1$. In general, the quantum channel will not be completely transparent, and D will be between 0 and 1. It's important to note that D is different from the potential barrier Z that we discussed earlier in the BTK model. They are related by $D = 1/(1 + Z^2)$ [33]. Andreev reflections take

place at each S-N interface. This gives rise to the possibility of multiple Andreev reflections and multiple barrier scattering, which significantly complicates the analysis.

Andreev reflection can be characterized by a reflection amplitude a that depends on quasiparticle energy ε [34]:

$$a(\varepsilon) = \frac{1}{\Delta} \times \begin{cases} \varepsilon - \text{sgn}(\varepsilon)(\varepsilon^2 - \Delta^2)^{\frac{1}{2}}, & \text{for } |\varepsilon| > \Delta \\ \varepsilon - i(\Delta^2 - \varepsilon^2)^{\frac{1}{2}}, & \text{for } |\varepsilon| < \Delta \end{cases}. \quad (4.62)$$

Averin and Bardas then defined a scattering matrix to account for the tunnel barrier:

$$S_{el} = \begin{pmatrix} r & t \\ t & -r^*t \end{pmatrix}, \quad (4.63)$$

where r is the probability amplitude of the quasiparticle reflected from the barrier in the normal region (see N1 in Fig. 4.2), and t represents the probability amplitude for a quasiparticle to be transmitted through the barrier. In the AB model, wavefunctions in region N1 generated by an electron-like quasiparticles incident from the left superconductor can be written as [34]:

$$\psi_{el} = \sum_{n=-\infty}^{\infty} [(a_{2n}A_n + J\delta_{n0})e^{ikx} + B_n e^{-ikx}] e^{-\frac{i(\varepsilon+2neV)t}{\hbar}} \quad (4.64a)$$

$$\psi_h = \sum_{n=-\infty}^{\infty} [A_n e^{ikx} + a_{2n}B_n e^{-ikx}] e^{-\frac{i(\varepsilon+2neV)t}{\hbar}}, \quad (4.64b)$$

where k and ε are the wave-vector and energy of the incident quasiparticle, and $a_n = a(\varepsilon + neV)$, and n is the net number of Andreev reflection. The second term of the electron wave function in Eq. (4.64) corresponds to a quasiparticle incident from the superconductor and this produces an electron in the normal region with effective source amplitude [34]:

$$J(\varepsilon) = [1 - |a(\varepsilon)|^2]^{\frac{1}{2}}. \quad (4.65)$$

AB find the wave functions in region N2 of the channel are:

$$\psi_{el} = \sum_{n=-\infty}^{\infty} [C_n e^{ikx} + a_{2n+1} D_n e^{-ikx}] e^{-\frac{i(\varepsilon+(2n+1)eV)t}{\hbar}} \quad (4.66a)$$

$$\psi_h = \sum_{n=-\infty}^{\infty} [a_{2n+1} C_n e^{ikx} + D_n e^{-ikx}] e^{-\frac{i(\varepsilon+(2n+1)eV)t}{\hbar}}, \quad (4.66b)$$

where the sum over n represents contributions from multiple Andreev reflections. In this case, it takes over all integers from $-\infty$ to ∞ .

AB next used the scattering matrix to relate the wavefunctions in region 1 and 2. They wrote this matching conditions as [34]:

$$\begin{pmatrix} B_n \\ C_n \end{pmatrix} = S_{el} \begin{pmatrix} a_{2n} A_n + J \delta_{n0} \\ a_{2n+1} D_n \end{pmatrix} \quad (4.67a)$$

$$\begin{pmatrix} A_n \\ D_{n-1} \end{pmatrix} = S_h \begin{pmatrix} a_{2n} B_n \\ a_{2n-1} C_{n-1} \end{pmatrix}, \quad (4.67b)$$

where

$$S_h = S_{el}^*, \quad (4.68a)$$

$$S_{el} = \begin{pmatrix} r & t \\ t & -\frac{r^* t}{t^*} \end{pmatrix} \quad (4.68b)$$

Using Eqs. (4.67), Averin and Bardas presented a recursion relation for finding the coefficients A_n, B_n, C_n and D_n for the case $\Delta_1 = \Delta_2$. From Eq. (4.67a) we can get:

$$B_n = r a_{2n} A_n + r J \delta_{n0} + t a_{2n+1} D_n, \quad (4.69)$$

$$C_n = t a_{2n} A_n + t J \delta_{n0} - \frac{r^* t}{t^*} a_{2n+1} D_n. \quad (4.70)$$

Then from Eq. (4.69) and Eq. (4.70), we can get C_n and D_n as a function of A_n and B_n :

$$D_n = \frac{1}{ta_{2n+1}}B_n - \frac{ra_{2n}}{ta_{2n+1}}A_n - \frac{rJ\delta_{n0}}{ta_{2n+1}}, \quad (4.71)$$

$$C_n = \left(\frac{|r|^2}{t^*}a_{2n} + ta_{2n} \right) A_n - \frac{r^*}{t^*}B_n + \left(\frac{|r|^2}{t^*} + t \right) J\delta_{n0}. \quad (4.72)$$

We get the similar results for the Eq. (4.67b):

$$A_n = r^*a_{2n}B_n + t^*a_{2n-1}C_{n-1}, \quad (4.73)$$

$$D_{n-1} = t^*a_{2n}B_n - \frac{rt^*}{t}a_{2n-1}C_{n-1}. \quad (4.74)$$

Substituting C_n from Eq. (4.70) into Eq. (4.73), we get:

$$\begin{aligned} A_{n+1} &= r^*a_{2n+2}B_{n+1} + t^*a_{2n+1} \left[\left(\frac{|r|^2}{t^*}a_{2n} + ta_{2n} \right) A_n - \frac{r^*}{t^*}B_n + \left(\frac{|r|^2}{t^*} + t \right) J\delta_{n0} \right] \\ &= r^*a_{2n+2}B_{n+1} + Ra_{2n}a_{2n+1}A_n + Da_{2n}a_{2n+1}A_n - r^*a_{2n+1}B_n + Ra_{2n+1}J\delta_{n0} + Da_{2n+1} \end{aligned} \quad (4.75)$$

thus:

$$A_{n+1} - a_{2n+1}a_{2n}A_n = \sqrt{R}(a_{2n+2}B_{n+1} - a_{2n+1}B_n) + Ja_1\delta_{n0}, \quad (4.76)$$

where $R = |r|^2$.

The same method can be used to derive the recursion relation for B_n [34]:

$$\begin{aligned} &\frac{Da_{2n+1}a_{2n+2}}{1 - a_{2n+1}^2}B_{n+1} - \left(\frac{a_{2n+1}^2R - 1}{a_{2n+1}^2 - 1} - \frac{Da_{2n-1}a_{2n}^2}{a_{2n-1}^2 - 1} \right. \\ &- Ra_{2n}^2)B_n + \left. + \left(\frac{a_{2n-1}a_{2n}(a_{2n-1}^2R - 1)}{a_{2n-1}^2 - 1} - Ra_{2n}a_{2n-1} \right) B_{n-1} \right. \\ &= -rJ\delta_{n,0} - rJa_2a_1\delta_{n-1,0} + rJa_2a_1\delta_{n-1,0} \end{aligned} \quad (4.77)$$

These recursion relations are important because Eq. (4.76) and Eq. (4.77) can be solved by choosing a maximum value n_m for n and setting all coefficients to 0 if $|n| > n_m$. The wavefunction amplitudes A_n and B_n are needed to find the current through the S-I-S junction, as I describe in the next session.

4.4.4 Transmon Relaxation with Multiple Andreev Reflections

Quasiparticles tunneling through a junction that is biased with a voltage V can gain or lose energy neV from MAR process. This implies that MAR can cause dissipation in the transmon and this dissipation will be greater than that due to single quasiparticle tunneling. During an MAR process, the total charge transferred across the junction is $ne = \pm e, \pm 2e, \pm 3e\dots$ and the resulting relaxation rate of the qubit is:

$$\frac{1}{T_1} \cong \frac{1}{2\hbar\omega C} \sum_{n=-\infty}^{\infty} 2q_n * I_n \left(\frac{\hbar f}{q_n} \right) = \frac{1}{2\hbar\omega C} \sum_{n=-\infty}^{\infty} 2ne * I_n \left(\frac{\hbar f}{ne} \right), \quad (4.78)$$

Thus, to find the relaxation rate due to quasiparticle, we need to find the current at voltage $\hbar f / ne$ due to each process that transfers different charge ne across the junction, where $n = \pm 1, \pm 2, \pm 3, \dots \infty$. In conventional single quasiparticle tunneling through a low-transparency junction, only the $n = 1$ term will be important. However, for junctions, with non-zero transparency, MAR can be important and higher order terms will dominate.

The approach developed by Averin and Bardas [34] provides a model for finding the current-voltage characteristics of an S-I-S junction undergoing MAR for the case $\Delta_1 = \Delta_2$. This approach was generalised to the case $\Delta_1 \neq \Delta_2$ by W. T. Liao *et al.* [38]. With MAR, an applied voltage can lead to multiple Andreev reflections, allowing for the transport of multiple Cooper pairs across the junction in addition to quasiparticles. The resulting current-voltage characteristics

have features that occur at voltages that are a fraction of the superconducting gap voltages of the electrodes, as well as at their sum and difference.

When an electron-like quasiparticle with energy ε is incident from the left superconducting electrode onto the S/N interface, we could find the wavefunctions by applying Eqs. (4.64) (4.65) and (4.68). The electron and the hole probability current density can then be found by applying:

$$j = \frac{\hbar}{2mi} (\psi^* \nabla \psi - \psi \nabla \psi^*). \quad (4.79)$$

In principle, we can use this to find the total probability current density due to an electron-like quasiparticle with energy ε incident from the left superconducting side. AB find that this probability current density can be written as a sum of Fourier components [34]:

$$j(\varepsilon, t) = \frac{\hbar k}{m} \sum_{K=0, \pm 1, \pm 2, \dots} j_K(\varepsilon, V) e^{\frac{i2KeVt}{\hbar}}. \quad (4.80)$$

Intepreting over energy and including the occupancy and density of states of the quasiparticles, one can write the total current as:

$$I(t) = \sum_k I_k e^{i2keVt/\hbar}, \quad (4.81)$$

where I_k is the current for the k -th Fourier component.

For my devices, I need to include contributions from non-equilibrium quasiparticles. I assume the non-equilibrium quasiparticles have an occupancy function $g_L(\varepsilon)$ for the electron-like quasiparticles and $g_L(-\varepsilon)$ for the hole-like quasiparticles:

$$g(\varepsilon, T) = \begin{cases} \frac{1}{1 + e^{\frac{\varepsilon - \mu}{k_B T}}} & \text{for } \varepsilon > 0. & (4.82a) \\ \frac{1}{1 + e^{\frac{\varepsilon + \mu}{k_B T}}} & \text{for } \varepsilon < 0. & (4.82b) \end{cases}$$

For thermal equilibrium quasiparticles, we have $\mu = \varepsilon_F$ and this was the case considered by AB

and by W. T. Liao *et al.* For non-equilibrium quasiparticles, μ will be determined by the density of non-equilibrium quasiparticles (see discussion in section 4.1.2). For thermal equilibrium quasiparticles, W. T. Liao *et al.* formed the k -th Fourier component which can be written as [38]:

$$I_k = \frac{e}{2\pi\hbar} \left[2eVD\delta_{k0} - \int_{-\infty}^{\infty} d\epsilon (1 - 2g_L(\epsilon)) X_k^{(L)} + \int_{-\infty}^{\infty} d\epsilon (1 - 2g_R(\epsilon)) Y_k^{(R)} \right], \quad (4.83)$$

where:

$$X_k^{(L)} = J^L(\epsilon) \left(a_{2k}^{*(L)} A_k^{*(L)} + a_{-2k}^{(L)} A_{-k}^{(L)} \right) + \sum_{n=-\infty}^{\infty} \left(1 + a_{2n}^{(L)} a_{2(n+k)}^{*(L)} \right) \left(A_n^{(L)} A_{n+k}^{*(L)} - B_n^{(L)} B_{n+k}^{*(L)} \right) \quad (4.84a)$$

$$Y_k^{(R)} = J^R(\epsilon) \left(a_{2k}^{(R)} A_k^{(R)} + a_{-2k}^{*(R)} A_{-k}^{*(R)} \right) + \sum_{n=-\infty}^{\infty} \left(1 + a_{2n}^{*(R)} a_{2(n+k)}^{(R)} \right) \left(A_n^{*(R)} A_{n+k}^{(R)} - B_n^{*(R)} B_{n+k}^{(R)} \right). \quad (4.84b)$$

Here D is the junction transparency. The superscript L in the A_k and B_k factors are quasiparticle amplitudes that arose from quasiparticles that were sourced from the left electrode, while the superscript R in the A_k and B_k factors designate amplitudes that arose from quasiparticles that were sourced from the right electrode. Similarly, the L superscript in the a_k factors designates an Andreev reflection amplitude off the left electrode, while the superscript R superscript in the a_k factors designates an Andreev reflection amplitude off the right electrode. The $X_k^{(L)}$ factor is generated by electron-like or hole-like quasiparticles that started from the left electrode, while the $Y_k^{(L)}$ factor is generated by electron-like or hole-like quasiparticles that started from the right electrode. This result applies to $\Delta_1 \neq \Delta_2$ as well as $\Delta_1 = \Delta_2$. Unfortunately, the electron-like and hole-like contributions have been combined. In Eq. (4.83a) and (4.83b) the sums are formally over

all integer values, *i.e.* for $n = 0, \pm 1, \pm 2, \dots \pm \infty$. The sums cannot be completed analytically and we need to resort to numerical evaluation and terminate these sums.

Notice that the integration over energy ϵ in Eq. (4.82) represents a sum over independent events. There will be a probability of seeing each event, or rate at which each event occurs, and a charge that is transferred during each event. The charge may correspond to a single electron transfer of $\pm e$, as in Giaever tunneling of a quasiparticle from one electrode to the other electrode of a junction. It can also be that charge $\pm 2e$ is exchanged, as occurs for Andreev reflection of a quasiparticle from an electrode. When multiple Andreev processes are included, in general a process can involve the transfer of ne charges, where n is an integer. For determining the transmon relaxation using Eq. (4.83) it will be necessary to not only determine the current contributions from the electron-like and hole-like quasiparticles from each electrode, but we will also need to tease out each process, the rate at which each process occurs and the charge transfer during each process.

Table 4.1 lists the 16 possible distinct processes that may occur with MAR in an S-I-S junction [38]. In this Table, positive n corresponds to clockwise movements around the diagram in Fig. 4.1. In the kernel column, $B_n^L(E, E', V)$, for example, designates the amplitude for leftward going electrons in region N_1 with energy $E' = E + 2neV$ that were generated by an electron that was incident from the left electrode (L-superscript) with energy E . As another example, $D_n^{R'}(E, E', V)$ designates the amplitude for rightward going holes in region N_2 with energy E' that were generated by a hole that entered from the right electrode (R'-superscript) with energy E . Similar to the discussion in Sec. 4.4.3, the amplitudes for the 16 processes can be solved from recursion relations, which are shown in Table 4.2.

Figure 4.4 shows an example simulation of current integrals for $D=0.05$, $\Delta_1 = 220\mu\text{eV}$, $\Delta_2 = 200\mu\text{eV}$, $\mu_1 = \mu_2 = 28.37\mu\text{eV}$, $k_B T = 13\mu\text{eV}$. The blue curve shows the current

from Process #3, the red curve shows the total current from all 16 processes. For process #3, which involves an electron from the left side Andreev reflecting off the right side and a hole being injected into the left side. This is the key Andreev process. I consider a current flow from right to left when V was applied. I can write the current as:

$$I_{\#3} = \sum_{n=-\infty}^{\infty} \frac{2ne}{2\pi\hbar} \int_{-\infty}^{\infty} |A_n^L(E, E')|^2 |J_L(E)|^2 |J_L(E')|^2 (g_L(E)g_L(E')) dE \quad (4.85)$$

where the occupancy and kernel terms of Process #3 can be found in the Table 4.1. The characteristics are quite complicated, there are many features in this plot. The most prominent feature includes in the blue curve, at $eV = \Delta_1 + \Delta_2 = 420 \mu\text{eV}$. This is due to quasiparticle Giaever tunneling when there's enough voltage. Two other features are at $eV = 200 \mu\text{eV}$ and $220 \mu\text{eV}$ (corresponding to Δ_1 and Δ_2). These are due to quasiparticles in the gap $\Delta_1 = 200 \mu\text{eV}$ and $\Delta_2 = 220 \mu\text{eV}$. At $eV = 110 \mu\text{eV}$ and $eV = 100 \mu\text{eV}$ (half of Δ_1 and Δ_2), this is due to MAR with $n=2$ ($2eV$ transfer). Below $80 \mu\text{eV}$, the current is small and independent of voltage. This current is from non-equilibrium quasiparticles. These step sizes will grow with the increased transparency.

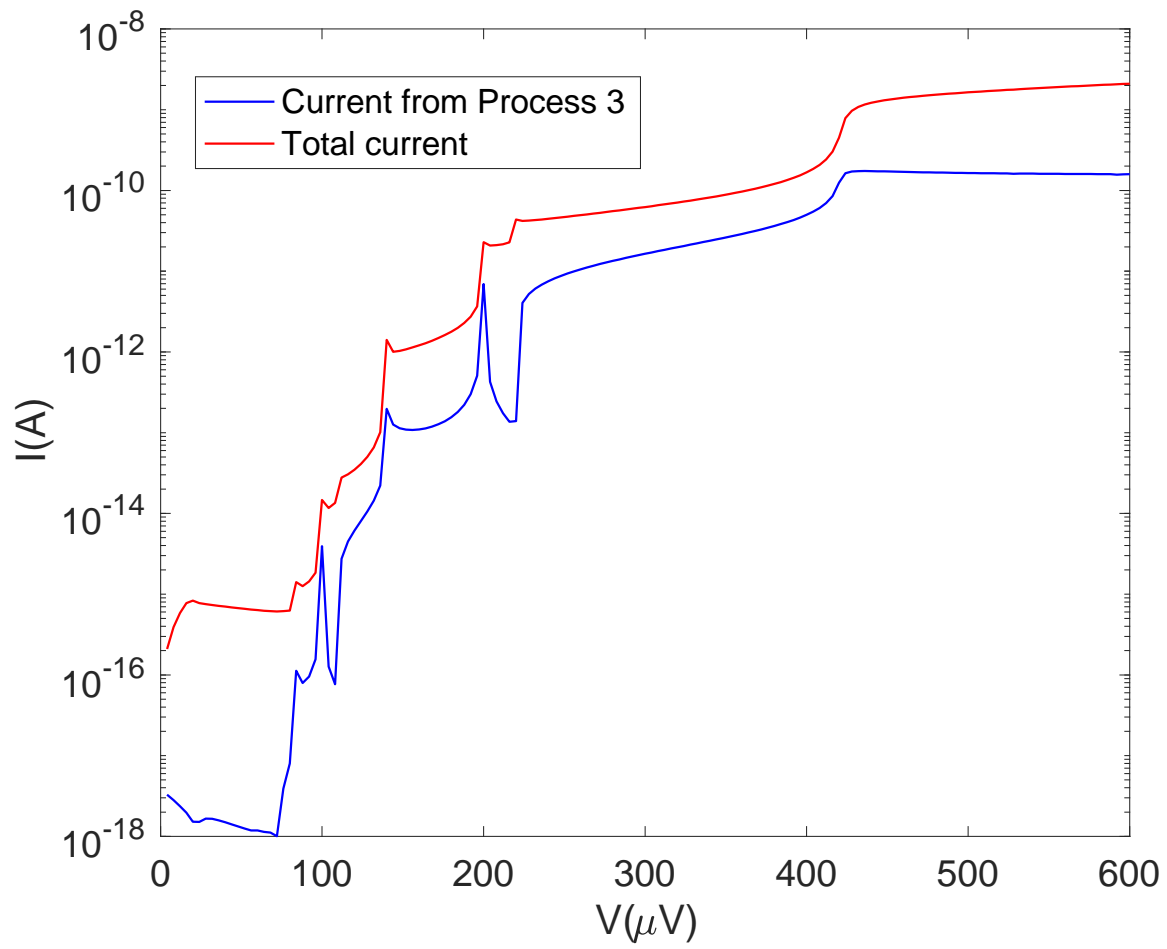


Figure 4.4: I-V curve for Andreev Reflection considering Process #3 and total current in semi log scale.

Table 4.1: Andreev tunneling processes. $-e$ in 2nd and 4th columns denote electron-like quasiparticle (charge $-e$), h denotes a hole with positive charge e , L is the left electrode, R is right electrode, L is left electrode. E is initial energy of the injected quasiparticle, E' is energy of emitted quasiparticle, ΔQ is the charge transferred from the L to R electrode due to the process.

#	start		end		occupancy	source/drain	kernel	E'	ΔQ
1	$-e$	L	$-e$	L	$\frac{g_L(E)^*}{(1-g_L(E'))}$	$ J_L(E) ^2 J_L(E') ^2$	$ B_n^L(E, E', V) ^2$	$E_e = E + 2neV$	$-2ne$
2	$-e$	L	$-e$	R	$\frac{g_L(E)^*}{(1-g_R(E'))}$	$ J_L(E) ^2 J_R(E') ^2$	$ C_n^L(E, E', V) ^2$	$E_e = E + (2n+1)eV$	$-(2n+1)e$
3	$-e$	L	h	L	$g_L(E)g_L(E')$	$ J_L(E) ^2 J_L(E') ^2$	$ A_n^L(E, E', V) ^2$	$-(E + 2neV) = -E_n$	$-2ne$
4	$-e$	L	h	R	$g_L(E)g_R(E')$	$ J_L(E) ^2 J_R(E') ^2$	$ D_n^L(E, E', V) ^2$	$-(E + (2n+1)eV) = -E_n$	$-(2n+1)e$
5	$-e$	R	$-e$	L	$\frac{g_R(E)^*}{(1-g_L(E'))}$	$ J_R(E) ^2 J_L(E') ^2$	$ B_n^R(E, E', V) ^2$	$E_e = E + (2n+1)eV$	$-(2n+1)e$
6	$-e$	R	$-e$	R	$\frac{g_R(E)^*}{(1-g_R(E'))}$	$ J_R(E) ^2 J_R(E') ^2$	$ C_n^R(E, E', V) ^2$	$E_e = E + 2neV$	$-2ne$
7	$-e$	R	h	L	$g_R(E)g_L(E')$	$ J_R(E) ^2 J_L(E') ^2$	$ A_n^R(E, E', V) ^2$	$-(E + (2n+1)eV) = -E_n$	$-(2n+1)e$
8	$-e$	R	h	R	$g_R(E)g_R(E')$	$ J_R(E) ^2 J_R(E') ^2$	$ D_n^R(E, E', V) ^2$	$-(E + 2neV) = -E_n$	$-2ne$
9	h	L	$-e$	L	$\frac{(1-g_L(E))^*}{(1-g_L(E'))}$	$ J_L(E) ^2 J_L(E') ^2$	$ B_n^{L'}(E, E', V) ^2$	$E_e = -E + 2neV$	$-2ne$
10	h	L	$-e$	R	$\frac{(1-g_L(E))^*}{(1-g_R(E'))}$	$ J_L(E) ^2 J_R(E') ^2$	$ C_n^{L'}(E, E', V) ^2$	$E_e = -E + (2n+1)eV$	$-(2n+1)e$
11	h	L	h	L	$\frac{(1-g_L(E))^*}{g_L(E')}$	$ J_L(E) ^2 J_L(E') ^2$	$ A_n^{L'}(E, E', V) ^2$	$E - 2neV = -E_n$	$-2ne$
12	h	L	h	R	$\frac{(1-g_L(E))}{g_R(E')}$	$ J_L(E) ^2 J_R(E') ^2$	$ D_n^{L'}(E, E', V) ^2$	$E - (2n+1)eV = -E_n$	$-(2n+1)e$
13	h	R	$-e$	L	$\frac{(1-g_R(E))}{*(1-g_L(E'))}$	$ J_R(E) ^2 J_L(E') ^2$	$ B_n^{R'}(E, E', V) ^2$	$E_e = -E + (2n+1)eV$	$-(2n+1)e$
14	h	R	$-e$	R	$\frac{(1-g_R(E))}{*(1-g_R(E'))}$	$ J_R(E) ^2 J_R(E') ^2$	$ C_n^{R'}(E, E', V) ^2$	$E_e = -E + 2neV$	$-2ne$
15	h	R	h	L	$\frac{(1-g_R(E))}{*g_L(E')}$	$ J_R(E) ^2 J_L(E') ^2$	$ A_n^{R'}(E, E', V) ^2$	$E - (2n+1)eV = -E_n$	$-(2n+1)e$
16	h	R	h	R	$\frac{(1-g_R(E))}{*g_R(E')}$	$ J_R(E) ^2 J_R(E') ^2$	$ D_n^{R'}(E, E', V) ^2$	$E - 2neV = -E_n$	$-2ne$

Table 4.2: Unity Source Recursion relations for finding the electron and hole wave amplitudes.

e-source on left (process 1-4)	h-source on left (process 9-12)	e-source on right (process 5-8)	h-source on right (process 13-16)
\mathcal{A}_n $= r^* a_{2n} \mathcal{B}_n + t^* a_{2n-1} \mathcal{C}_{n-1}$	\mathcal{A}_n $= r^* a_{2n} \mathcal{B}_n + t^* a_{2n-1} \mathcal{C}_{n-1}$ $+ r^* \delta_{n0}$	$\mathcal{A}_n = r^* a_{2n} \mathcal{B}_n + t^* a_{2n-1} \mathcal{C}_{n-1}$	\mathcal{A}_n $= r^* a_{2n} \mathcal{B}_n + t^* a_{2n-1} \mathcal{C}_{n-1}$ $+ t \delta_{n-1,0}$
$\mathcal{B}_n = r a_{2n} \mathcal{A}_n + t a_{2n+1} \mathcal{D}_n$ $+ r \delta_{n0}$	$\mathcal{B}_n = r a_{2n} \mathcal{A}_n + t a_{2n+1} \mathcal{D}_n$	$\mathcal{B}_n = r a_{2n} \mathcal{A}_n + t a_{2n+1} \mathcal{D}_n$ $+ t \delta_{n0}$	$\mathcal{B}_n = r a_{2n} \mathcal{A}_n + t a_{2n+1} \mathcal{D}_n$
$\mathcal{C}_n = t a_{2n} \mathcal{A}_n - r^* \frac{t}{t^*} a_{2n+1} \mathcal{D}_n$ $+ t \delta_{n0}$	$\mathcal{C}_n = t a_{2n} \mathcal{A}_n - r^* \frac{t}{t^*} a_{2n+1} \mathcal{D}_n$	$\mathcal{C}_n = t a_{2n} \mathcal{A}_n - r^* \frac{t}{t^*} a_{2n+1} \mathcal{D}_n$ $+ r \delta_{n0}$	$\mathcal{C}_n = t a_{2n} \mathcal{A}_n$ $- r^* \frac{t}{t^*} a_{2n+1} \mathcal{D}_n$
\mathcal{D}_{n-1} $= t^* a_{2n} \mathcal{B}_n - r \frac{t^*}{t} a_{2n-1} \mathcal{C}_{n-1}$	\mathcal{D}_{n-1} $= t^* a_{2n} \mathcal{B}_n - r \frac{t^*}{t} a_{2n-1} \mathcal{C}_{n-1}$ $+ t^* \delta_{n0}$	\mathcal{D}_{n-1} $= t^* a_{2n} \mathcal{B}_n - r \frac{t^*}{t} a_{2n-1} \mathcal{C}_{n-1}$	$\mathcal{D}_{n-1} = t^* a_{2n} \mathcal{B}_n$ $- r \frac{t^*}{t} a_{2n-1} \mathcal{C}_{n-1}$ $+ r^* \delta_{n-1,0}$

Chapter 5

Transmons Design and Fabrication

The transmon qubits I fabricated and measured were based on a three-dimensional (3D) configuration [1], in which the qubit is mounted in a three-dimensional microwave cavity made of superconducting Al, as in H. Paik's original design. This innovative design offers some advantages over 2D configurations [2], including reduction of decoherence caused by surface dielectric loss and reduced loss due to coupling to low-Q microwave modes. Consequently, this strategy allows for potentially longer lifetimes of the qubits.

In this chapter, I describe the design and fabrication of a transmon chip SKD102. Dr. Sudeep Dutta wrote the pattern and I fabricated the chip. In Section 5.1, I discuss the design of our transmons as well as the test patterns and the layout of the chips. In section 5.2, I discuss the cavity design. This is followed, in section 5.3, with a discussion of transmon fabrication, including substrate preparation, e-beam lithography, thermal evaporation, and lift-off. In the remaining sections I describe initial testing on the junctions and films that I used to characterize the process.

5.1 Transmon Design

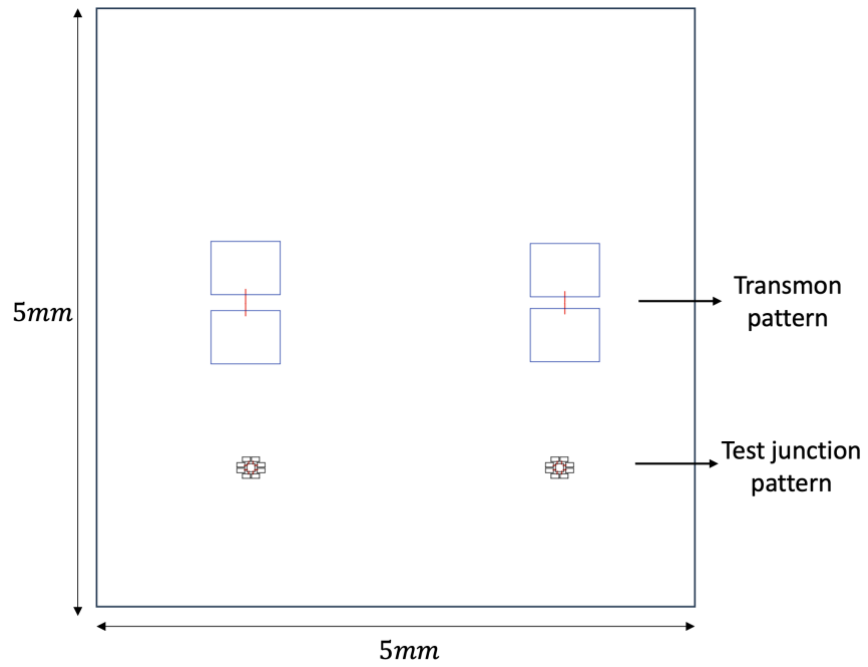
The design of our 3D transmons is similar to that of many other groups [3][4]. I used the same design for our conventional and gap-engineered transmons. For most of my transmon chips, there were two transmons and two sets of test junction patterns on one $5\text{mm} \times 5\text{mm}$ sapphire chip. The main reason for having two transmons on one chip was to allow me to fabricate and simultaneously test a gap-engineered transmon and a standard transmon.

Figure 5.1(a) shows the design of our transmon chip pattern. Each transmon has two large pads which act as shunting capacitors for the Josephson junctions. They also act as a dipole antenna to couple to the mode of the cavity. Each pad is $500\ \mu\text{m} \times 650\ \mu\text{m}$ and this layout gives $C_\Sigma \sim 80\text{fF}$ and $E_c/h \simeq 200\ \text{MHz}$ on a sapphire substrate. My design target was for a transmon frequency below 4 GHz which reduces the loss from the Purcell effect [5].

For spectroscopic measurements to distinguish the two transmons on each chip, the junction areas were designed to differ by 10% with $200\ \text{nm} \times 200\ \text{nm}$ and $200\ \text{nm} \times 220\ \text{nm}$, respectively, which tends to give critical currents that differ by 10%. In practice however, there is too much variation in our oxidation process to make this difference reliable, so in addition the spacings between the two pads were also made to differ. I used spacings of $120\ \mu\text{m}$ and $150\ \mu\text{m}$, respectively, which resulted in a 10% difference in E_c . This difference in E_c was observable by measuring the anharmonicity and transition frequencies.

Each chip also included test junctions. Below each transmon, there was a test pattern with eight Josephson junctions (see Fig. 5.1(b)). Each test junction was identical to the left transmon with $200\ \text{nm} \times 200\ \text{nm}$ junction sizes. The eight junctions in a pattern share one capacitance pad in the center. The purpose of these test patterns was to check the resistance variation in co-evaporated junctions and identify good oxidation patterns.

(a)



(b)

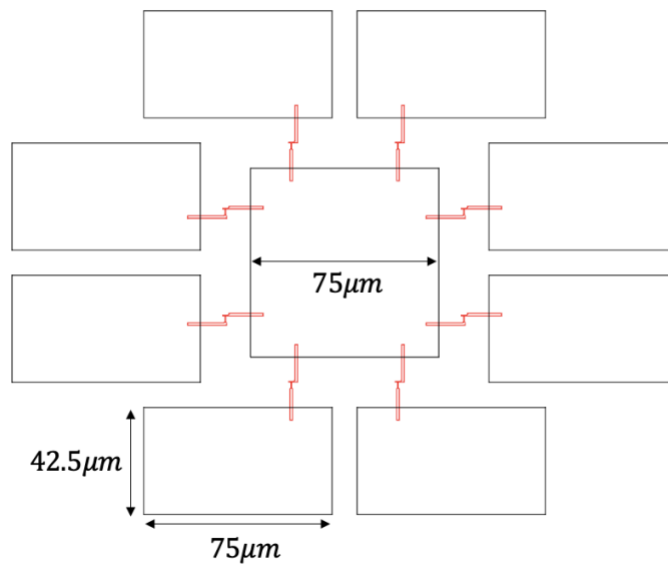


Figure 5.1: CAD drawing of the chip design. (a) Two transmons (large structures) and two sets of testing junctions below. (b) Detail of the testing junctions.

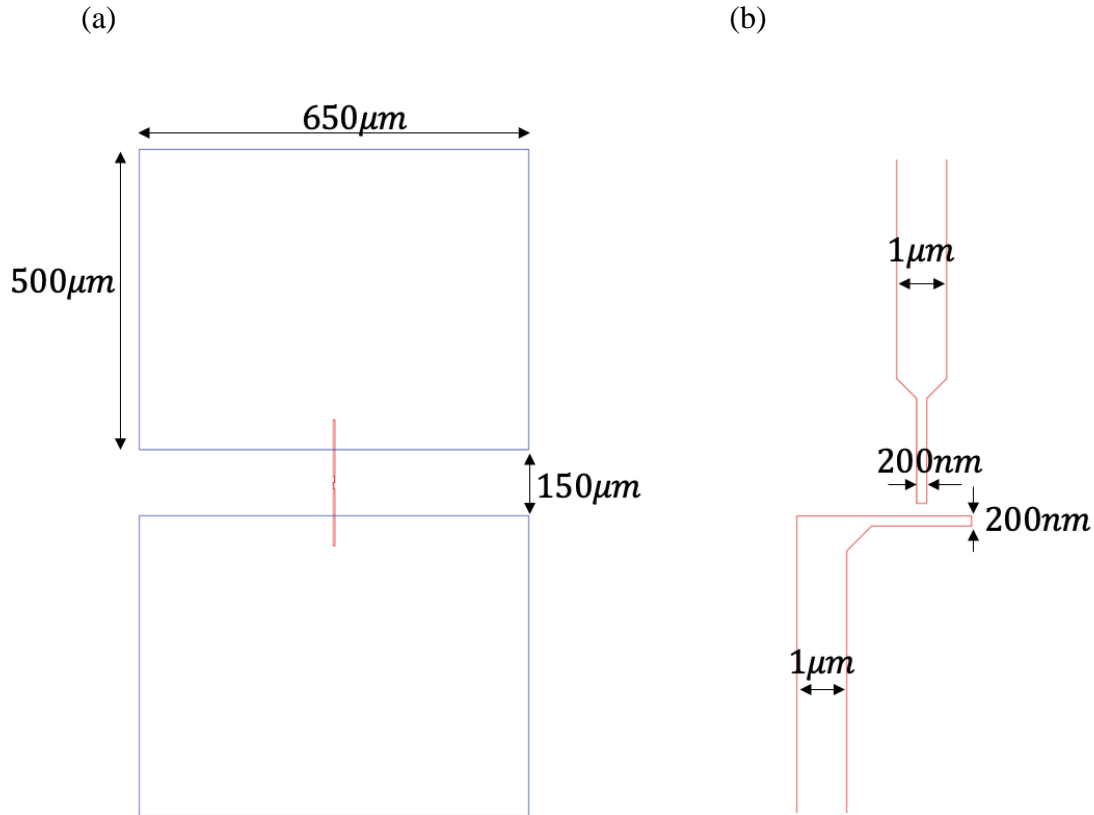


Figure 5.2 (a) CAD drawing of transmon pads (blue) and the Josephson junction (red). (b) Detail of the Josephson junction design.

Figure 5.2 (a) shows the CAD design of the left transmon. The blue rectangles represent the transmon capacitor pads and the red line represents the Josephson junction and its connections to the pads. The dimensions of each pad are $500\mu\text{m} \times 650\mu\text{m}$. Figure 5.2 (b) shows the design for the Josephson junction of the left transmon. This pattern gives a resist bridge between two disconnected lines; the bridge is used for two-angle evaporation of the junction [6]. The two 200nm wide lines are perpendicularly oriented to each other and separated by the 250nm resist bridge. The right transmon has slightly different dimensions as discussed above.

5.2 Cavity Design

The microwave cavities I used in my research were built by Dr. Cody Ballard [7]. A photograph of cavity SI-2a is shown in Fig. 5.3. The 5 mm × 5 mm transmon chip was placed inside the 3D cavity.

This cavity has a fundamental cavity resonance of about $f_c = 6.115$ GHz [8]. Setting the cavity's resonance higher than the transmon's transition frequency of ~ 3-6 GHz was an intentional design choice to decrease loss from the Purcell effect [5]. The cavity was made from Al because it exhibits low energy loss when it is in a superconducting state. The cavity was fitted with two non-magnetic SMA (Sub Miniature version A) connectors. These served as the input and output pins for the microwave drive and readout, respectively [9]. The strength of the coupling between the cavity mode and these ports was fine-tuned by carefully adjusting the length of the central conducting pin of the SMA connector that extends into the cavity [7].

5.3 Transmon Fabrication

For the construction of transmons, it's crucial to follow a precise and reliable fabrication process. Dust, unwanted oxide layers between the superconductor and substrate, contaminants, impurities, and errors in the alignment of the layers can significantly degrade the performance or operating parameters of the transmon. The fabrication of my transmons was carried out in the Toll Physics Building room B0219 and the FabLab in the Kim Building at the University of Maryland. In the following sections, I present a comprehensive description of each step in the fabrication procedure.

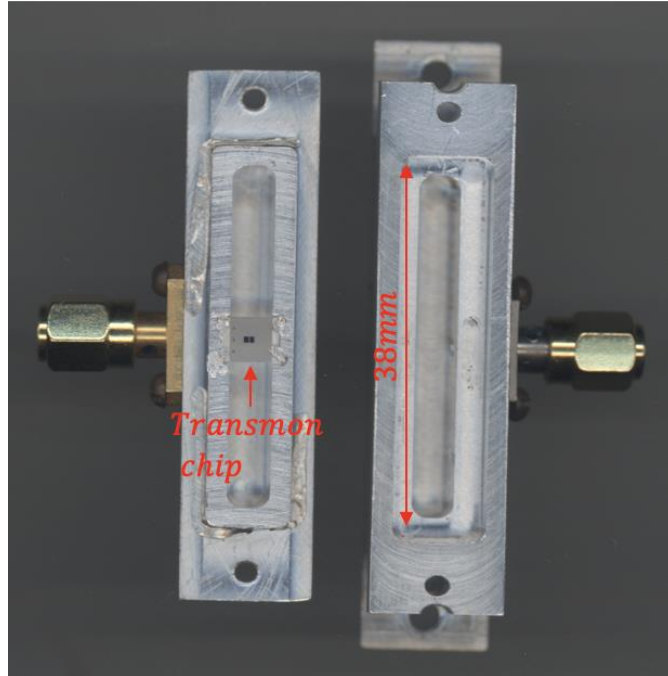


Figure 5.3: Picture of Al cavity SI-2a. The left half has a transmon chip mounted inside it. The SMA connectors (gold) are for the microwave input and output signals. The transmon chip was secured in place with indium between the sides of the chip and the cavity. The cavity was then sealed with In between the two halves.

5.3.1 Substrate Cleaning

The substrate preparation was performed in the FabLab by Dr. Sudeep Dutta. A clean 3-inch diameter c-axis oriented sapphire wafer was used. This wafer was 430 μm thick and polished on one side. The wafer was rinsed with acetone, methanol, isopropanol and finally water to remove any solvent residue. Each rinsing process took around 1 min. The wafer was then dried with nitrogen gas and baked on a hot plate at 200 $^{\circ}\text{C}$ for about 5 minutes.

5.3.2 Application of Resist Layers

The wafer was mounted on a Headway EC101 wafer spinner [10] and LOR10A resist [11] was applied. The spin speed was increased from 1000 rpm to 4000 rpm for 45 s. This speed and time results in a 1000 nm thick layer. The wafer was then baked on a hot plate at 180°C to 200°C for 10 minutes. Following the baking step, with the wafer stationary on the spinner, a drop of 950 PMMA C2 [12] was next applied. I then spun the wafer at 4000 rpm for 45 s, leaving a 150 nm thick layer. The wafer was then baked at 230°C in an oven for 2 hours.

Since sapphire is highly insulating, charging problems would occur during e-beam writing. To prevent this, I added a conducting layer. This anti-charging layer was 15 nm of thermally evaporated Al on top of the LOR/PMMA bi-layer stack.

5.3.3 Wafer Dicing

Before dicing the chip, 1813 photoresist [13] was applied to the wafer and spun at 4000 rpm for 45 s. It was then baked at 120 °C for 5 minutes. This protected the e-beam layers and the anti-charging layer from damage and contamination. Cutting was done on a Microautomation Industries Model 1006 dicing saw [14] with a 200 µm wide diamond blade to dice a wafer into 5 mm by 5 mm chips. In order to mount the wafer to the dicing saw stage, tape from Ultron Systems, Inc [15] was used.

5.3.4 E-Beam lithography

Before doing e-beam lithography, I peeled off the chosen chip from the dicing adhesive tape. I then put the chip into an acetone bath for 3 minutes to remove the protective 1813 resist layer. I then dried the chip with N_2 gas. I next applied a drop of aquaSAVE, a conductive polymer,

and spun the chip at 4000 rpm for a minute. The aquaSAVE helped to further reduce charging problems. After this step, the chip was then ready for e-beam writing.

E-beam writing was done on a Raith Eline system [16] in the FabLab using an accelerating voltage of 10 kV. I used a 60 μm aperture for junctions and a 120 μm aperture for capacitance pads. After adjusting the beam alignment and focus, the system was ready to do the writing. First, following the procedure of Dr. Sudeep Dutta for the junction layers, I used a dose of 160 $\mu\text{C}/\text{cm}^2$ with step size of 20 nm in x and y. For the pads layer, I used a dose of 200 $\mu\text{C}/\text{cm}^2$ with 100 nm lateral step size. The design was loaded as DXF format files with different layers. After checking the position list of each layer and the estimated dwell time, the chip was written. This typically took about one hour for pattern writing [16].

5.3.5 Developing the Resists

After finishing the writing, I developed the e-beam resist in the cleanroom of the FabLab. First, I removed the aquaSAVE anti-charging layer by rinsing the chip in water for one minute and then drying it with nitrogen gas. I next removed the Al anti-charging layer by placing the chip in a beaker of MF CD-26 [17] for 3 minutes. I next rinsed the chip in deionized water for 30 s and dried it with nitrogen gas. I then developed the PMMA e-beam resist layer by putting the chip in a beaker with a mixture of MIBK [18] and isopropanol in a ratio of 1:3 for about 80 s. I then moved the chip to a beaker of isopropanol for 30 s and dried with nitrogen gas. These steps removed all the areas that had been exposed by the electron beam.

I next placed the chips in MF CD-26 again to develop the undercut of the junction bridges. The development time for this step depends on the desired undercut widths. I typically used a development time of 50 s. After this I put the chip in DI water for one minute and dried the chip.

In Fig. 5.4, the undercut from the development of the LOR is visible as a bright edge around the pattern. After developing, each transmon pattern has an undercut bridge where the junction will be.

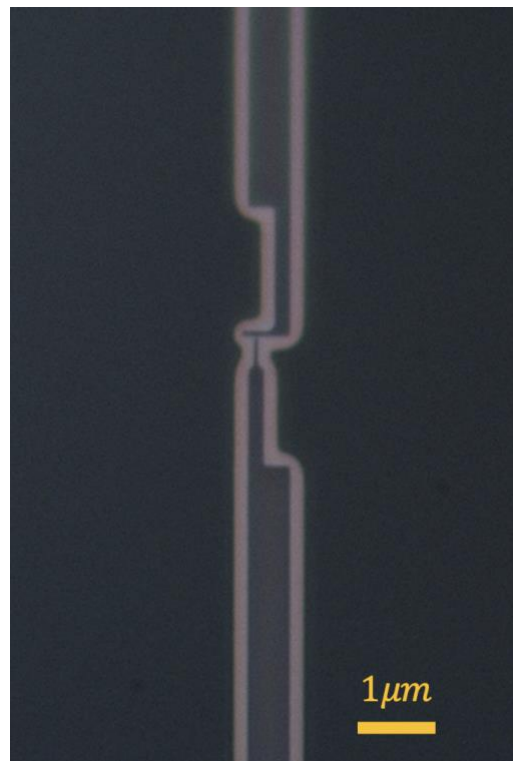


Figure 5.4: An optical photograph of the e-beam resist layers of the junction area after the development process. The brighter areas are the undercut region.

5.3.6 Thermal Evaporation

I used the cryo-pumped thermal evaporator in Room 0219 in the Toll Physics Building to perform the evaporation (see Fig. 5.5). The base pressure of this evaporator is about 2×10^{-7} Torr. For Al evaporation, I used top #2 of the evaporator. This evaporator top is designed for double-angle evaporation and has an angle indicator, which controls the sample tilt and can be seen through a window on the evaporator.

The evaporator has a small, separate volume which can be filled with oxygen for use during the oxidation step. This oxygen reservoir is connected to the chamber with a general-purpose valve and a needle valve. The needle valve allows precise control of oxygen pressure during the deposition (see last section of this Chapter).

After venting the evaporator, I loaded an evaporation boat with 5 or six pieces of Al shot; I used electrode #1 with tungsten wire evaporation baskets for the Al shot. I next clamped the chips onto a sample holder made by Dr. Sudeep Dutta. For depositing transmons with different layers, a mechanical mask was attached under the sample holder. If identical devices were needed, this mask was not used. Otherwise, the end of the mask was attached to the shutter with a string. With this system you can move the mechanical mask, and also cover chips when you don't want to deposit, or only expose chips you want by rotating the shutter. The moving mask attached to the shutter made it allowed me to make different depositions on different devices on the same chip. I then mounted the sample holder onto the rotating stage of the evaporation top, placed the top back onto the vacuum chamber and then pumped out the system to base pressure. I typically pumped overnight to ensure a low background pressure.

5.3.7 Double-Angle Al Deposition and Oxidation

For transmon chip SKD102 with left transmon Q_{L1} and right transmon Q_{R1} , I first set the sample stage angle to $\phi = -45^\circ$ and the entire chip with two qubits was then exposed to the evaporating aluminum. The typical evaporation rate was 0.3 nm/s to 0.6 nm/s. I stopped the Al

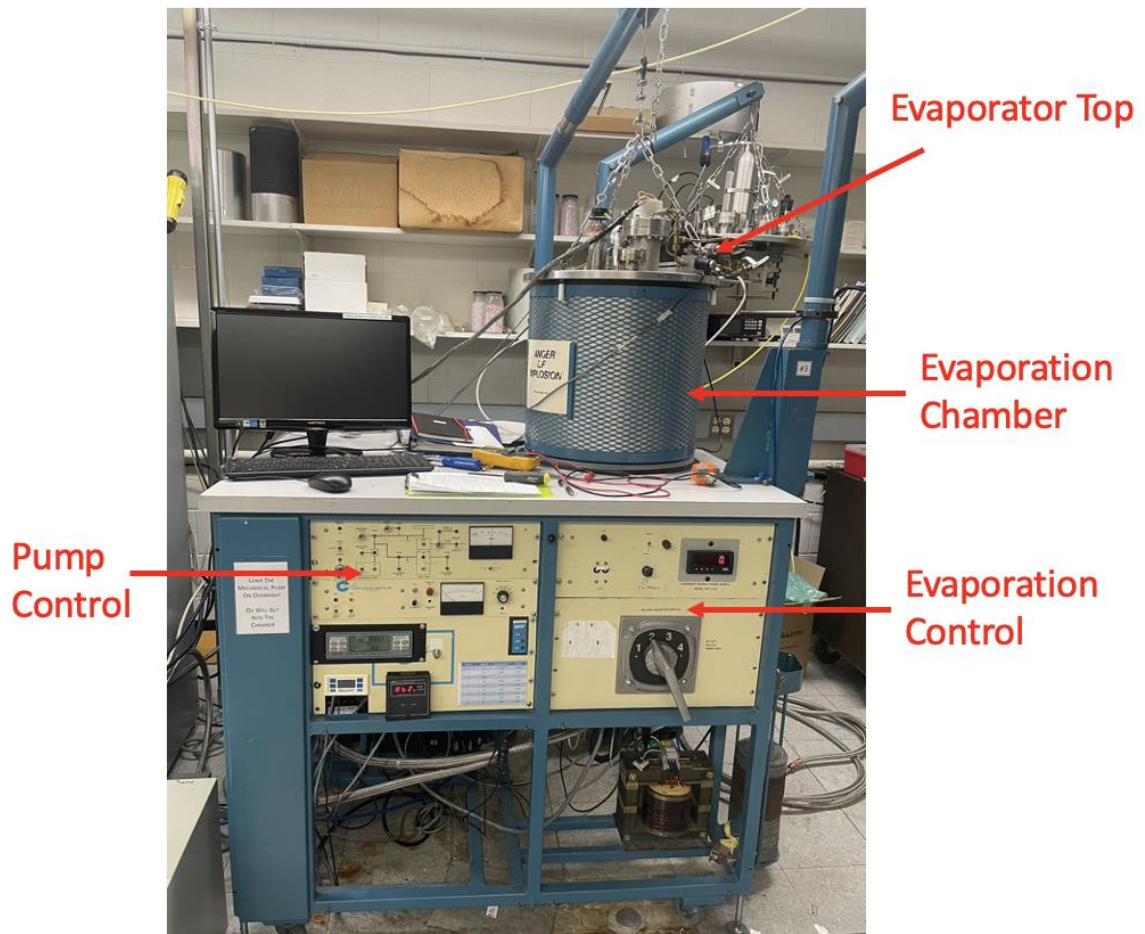


Figure 5.5: Photograph of the thermal evaporator.

deposition at a thickness of $h_1=28$ nm. the base electrode layers of the left and right transmons were evaporated at the same time, they should have the same superconducting gap Δ_1 .

After evaporating the base layer, I closed the shutter and stopped the evaporation. After waiting one minute for the system to cool down, I closed the valve between the cryopump and the evaporation chamber. I then oxidized the first Al layer by opening the general valve between the oxygen reservoir and the chamber to bleed in the desired amount of O_2 . The amount of the O_2 I used would vary from evaporation to evaporation. For device SKD102, I used 2 Torr of O_2 for 7.5 minutes. After the oxidation I reopened the cryo-pump valve and pumped the system for about 5 to 10 min to reach base pressure. During this process, I also changed the mechanical mask position, so the right transmon was totally covered by the mechanical mask while the left transmon was exposed to the evaporation source.

I then set an angle of $\phi= -12.5^\circ$ relative to the chip surface for the second evaporation, which is for second layer (counter electrode layer) of the gap-engineered transmon (left transmon). I then opened the needle valve to let oxygen in slowly. When the O_2 pressure inside the chamber stabilized to 2.5×10^{-6} Torr, I opened the shutter and started the evaporation. The second layer of the left transmon needs to fully cover the base electrode layer and should be twice as thick as the first layer to form a junction, so I evaporated the second layer to a thickness of about $h_2= 77$ nm. After the evaporation, I closed the shutter, turned off the needle valve and stopped the current. This gave a second layer with a superconducting gap Δ_2 that was greater than Δ_1 .

I then set the angle to $\phi= 0^\circ$ and moved the mechanical mask to fully cover the left transmon with the right transmon exposed to the evaporation source; no O_2 was present for this evaporation. This let me build the right transmon so that it was not gap-engineered. After the

evaporation, I closed the shutter and stopped the evaporation at a thickness of $h_3 = 66$ nm for this layer. The resulting gap Δ_3 of this layer should be close to Δ_1 .

Sudeep and I did separate measurements in co-deposited film to obtain the gaps of each electrode from T_C measurements. As discussed in the final section of this Chapter, I also did separate tests to determine how the gap of the thin Al films depended on O_2 pressure. For these two devices, the T_C measurements gave $\Delta_1 = 200.0$ μeV , $\Delta_2 = 227.1$ μeV and $\Delta_3 = 191.1$ μeV .

Finally, in order to have a clean oxide layer on the top layer of both devices, I ended with a passivation step. After the evaporation I closed off the cryo-pump and opened the O_2 reservoir to set a pressure of about 1.5 Torr for 15 to 30 minutes. After this was done, I vented the chamber with N_2 , placed the device in a chip holder, and moved onto the lift-off stage. The whole process is shown schematically in Fig. 5.6. Figure 5.7 shows the images of mechanical mask and chip holder and how mechanical mask moves during the deposition. Figure 5.8 shows part of the evaporation setup inside the evaporator with the location of shutter, mechanical mask and chip holder.

5.4 Lift-off Procedure

I performed the lift-off process in Room 0357 in the Toll Physics Building. The purpose of this step is to remove the Al that is not part of the final devices. I first prepared a beaker with Remover PG and put it on a hot plate set to 95 °C, covering it with a glass lid. After 15 min, the remover is hot, and I placed the chip in the liquid and left it for about 15 minutes. Next, I removed the chip and sprayed it with isopropanol to remove the excess Al. After this, I placed the chip back in the Remover PG for at least 30 min on the hot plate. I then removed it, gave it a final isopropanol spray, dried it using N_2 gas, and placed it in a chip carrier for transport. I then checked the junctions

under the optical microscope. If needed, I would repeat the lift-off process. Figure 5.9 shows SEM and optical microscope images of the resulting junction area.

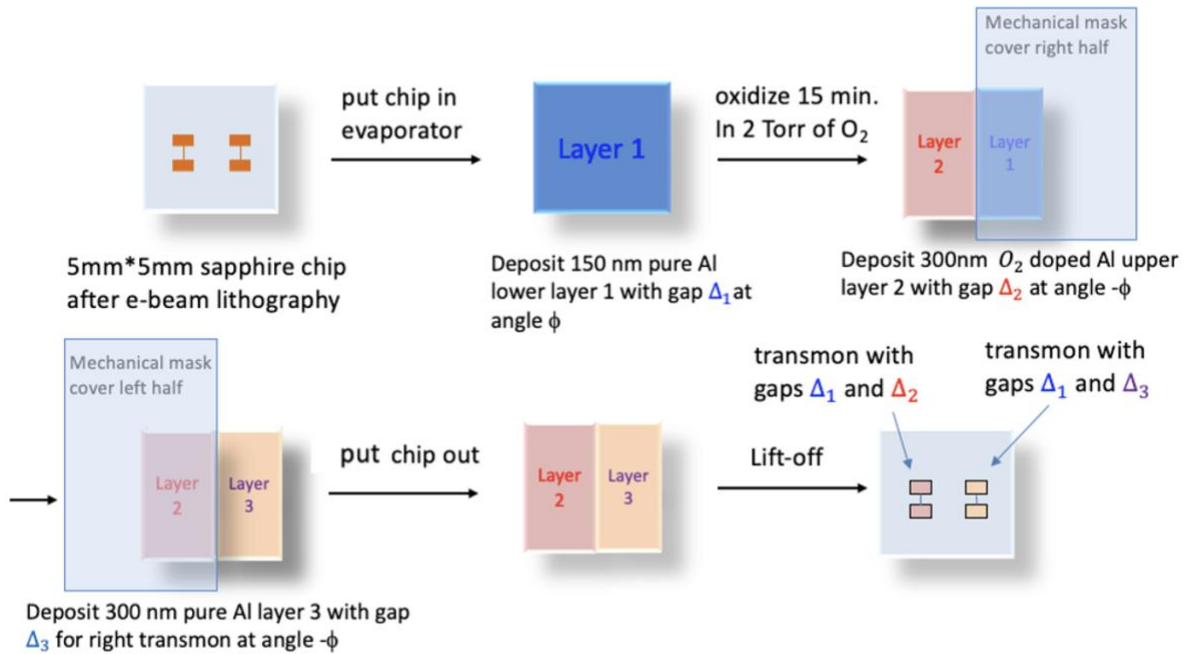
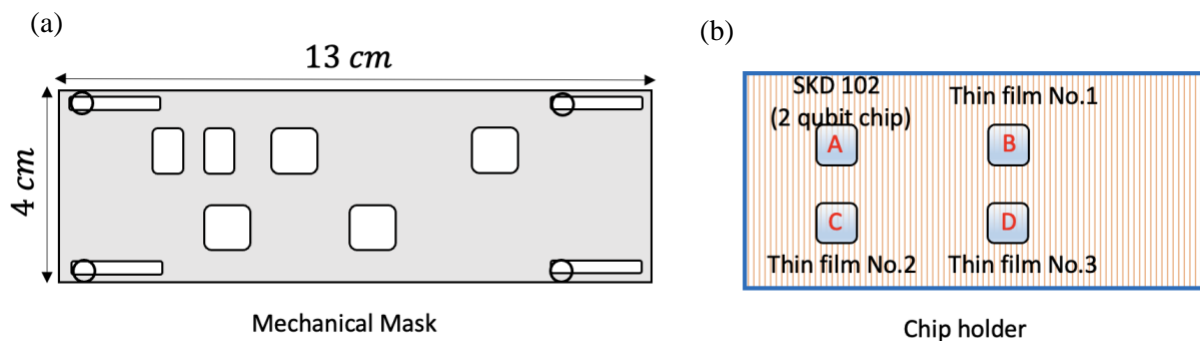


Figure 5.6: Double-angle evaporation fabrication procedure for building two transmons with different layer configurations on the same chip in the same pump down. The gap-engineered transmon has layers with gaps Δ_1 and Δ_2 . The standard transmon has layers with gaps Δ_1 and Δ_3 .



(c)

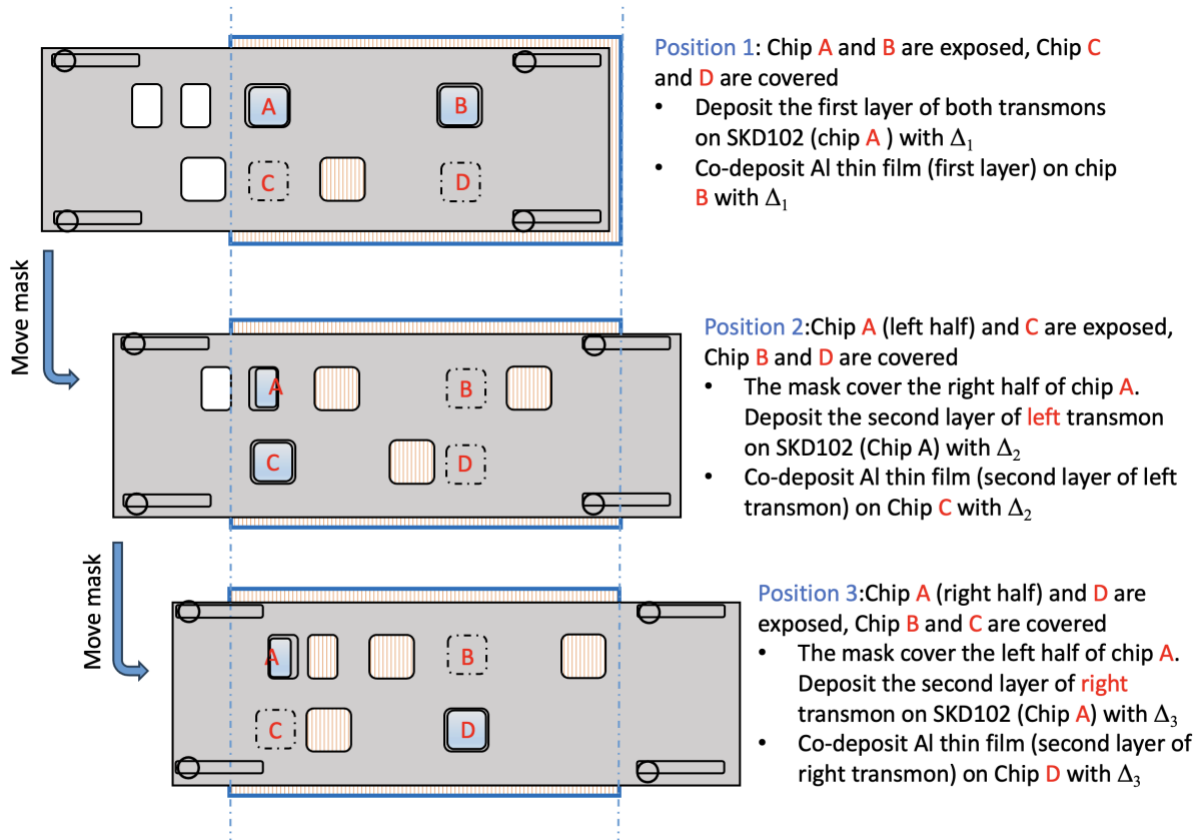


Figure 5.7: Images of chip holder and mechanical mask. (a) The mechanical mask has six holes in order to expose the chips on the chip holder. (b) The chip holder has four chips on it. The chip SKD102 is placed on position A. The chips on position B, C and D are for collecting the Al thin films for gap measurements. The mask is anchored on top of the chip holder with 5mm space in between. (c) Three different mask positions showing the deposition process of chip SKD102 with two transmons having the same first layer (Δ_1) but different second layer (Δ_2 and Δ_3) and the deposition of other three Al thin films.

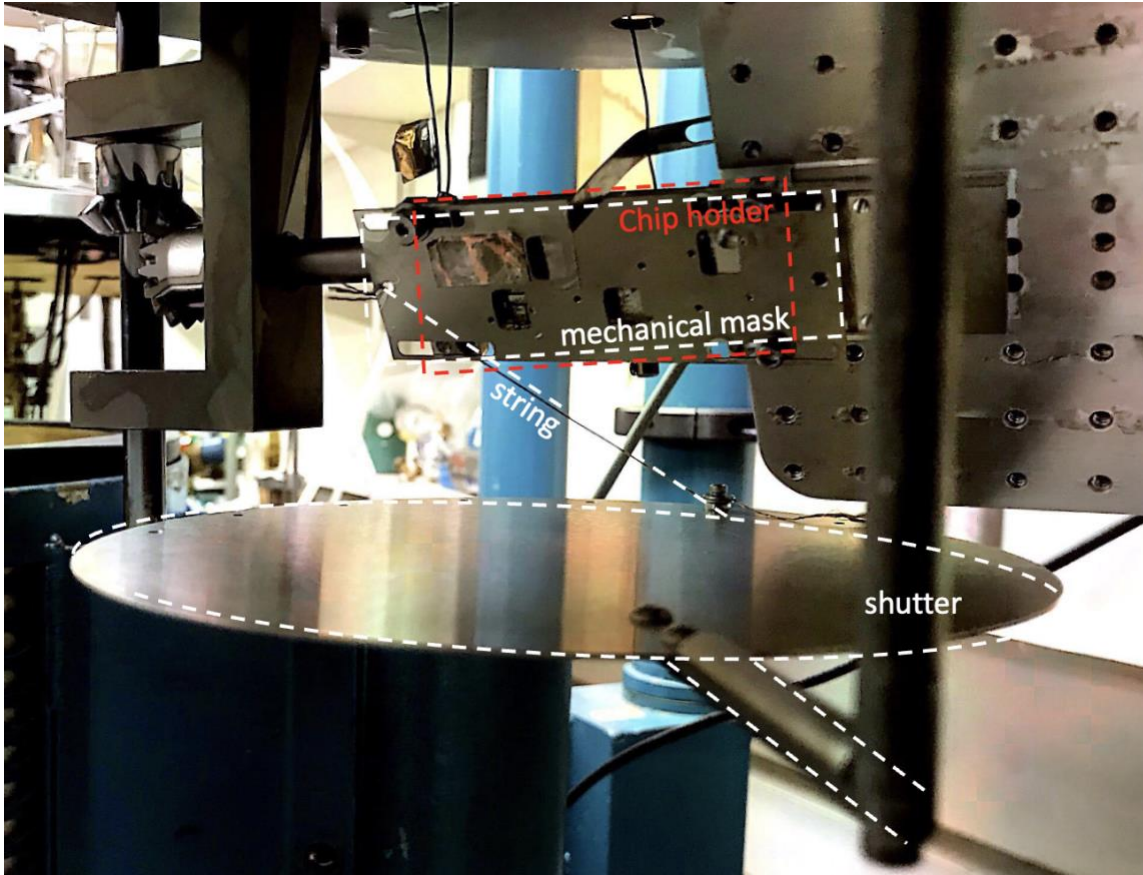
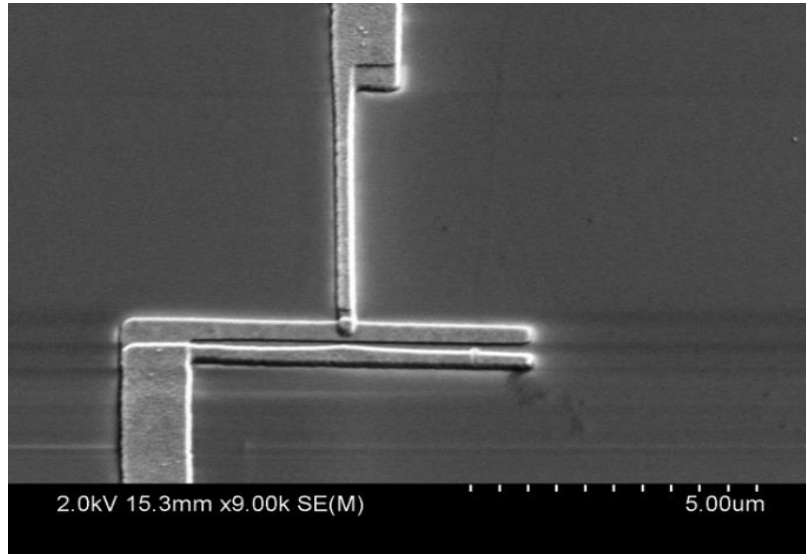


Figure 5.8: Evaporation setup inside the evaporator. The mechanical mask is anchored with the chip holder with screws. The chip holder is covered by the mask and its position is fixed while the mechanical mask can move horizontally. The mask is also attached to the shutter with a string, so it can follow the movement of the shutter. By rotating the shutter, mask can move to different positions for different depositions.

(a)



(b)



Figure 5.9: (a) SEM micrograph showing transmon junction formed using double-angle evaporation of Al. (b) Optical micrograph of transmon junction area.

5.5 Tunnel Junction Resistance Measurement

I next measured the resistance across the junctions using the probe station located in the sub-basement lab, Room SB 0331. I used a 100 k Ω resistor in series with the probes in order to protect the junctions from being blown out by static electricity. To measure the resistance, I used a Fluke 87 III handheld digital multimeter [19] set to a fixed range of 600 k Ω . To further protect the junctions, I attached a grounding switch via a BNC tee in parallel with the probes. While touching the probes to the junction pads, this switch was set to “ground”, which grounded the probes; I switched to “live” mode to take the measurement, which connected the probes to the circuit. I also used an SCD model 963E benchtop air ionizer [20] to reduce electrostatic charging. The gap engineered transmon on SKD102 had normal-state resistance $R_n = 22.4$ k Ω and the standard transmon had $R_n = 11.4$ k Ω . This was an acceptable range and corresponded to an expected transition frequency of 2.77 GHz and 3.88 GHz.

5.6 Oxygen Doping Tests on Al Films

As discussed, I used granular Al with different oxygen doping to fabricate transmon electrodes with different superconducting gaps. The gap-engineered transmon needed to have a base electrode and counter electrode that had different superconducting gaps. To have good values for the gap, I needed to know how much O₂ to include during the deposition. To get this data, I performed oxygen doping tests on thin Al films.

The test Al films were deposited on sapphire at a rate of about 0.5 nm/s in a cryo-pumped system with a base pressure of 3.5×10^{-7} Torr. Oxygen was bled into the chamber from an opening about 13 inches above the substrate and flowed continually through the system during the deposition. The O₂ pressure was monitored just above the system’s open gate valve and was lower

than the pressure at the sample, although we do not have an accurate calibration of difference in pressure. The film thickness was monitored using a crystal thickness monitor.

I deposited thin films with different O₂ pressure and thickness. After deposition, the resistance of the samples was measured versus temperature to determine the transition temperature T_C and the residual resistivity ratio (RRR). The RRR is a measure of the purity and granularity of the material. These measurements were carried out using a Physical Properties Measurement System (PPMS) in Room 0335 of Toll's Building.

Figure 5.10 shows the resulting critical temperature T_C versus oxygen doping pressure P according to crystal monitor during the deposition, the film thickness of the samples were around either 15nm and 35nm. However, subsequent profilometer measurements of real thickness showed this was about twice as large as the thickness from crystal monitor reading. As expected, higher oxygen doping pressure and thinner films [21]-[24] produced higher T_C values. From T_C , I determined the superconducting gap Δ using the BCS Eq. (3.28).

Finally, Figure 5.11 shows the RRR of the films vs T_C . Higher T_C films produced lower RRR as expected, and all the points fall on practically the same curve, independent of the film thickness.

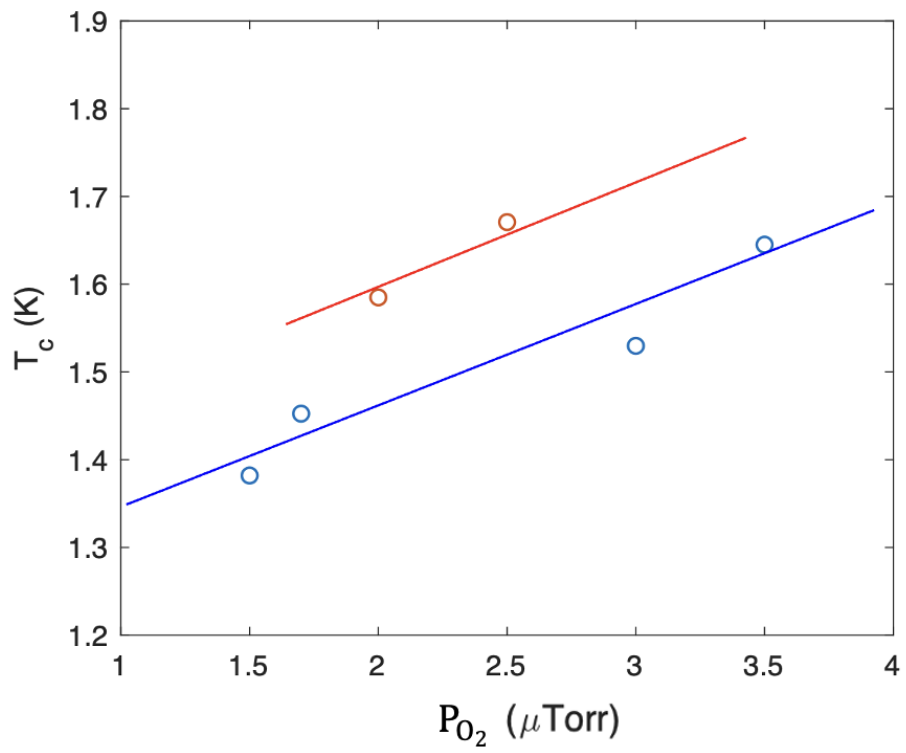


Figure 5.10: Plot showing measured film critical temperature T_C versus O_2 gas doping pressure P_{O_2} . The blue points are for 70 nm thick films and the red points are for 30 nm thick films. Red and blue lines are guides to the eye.

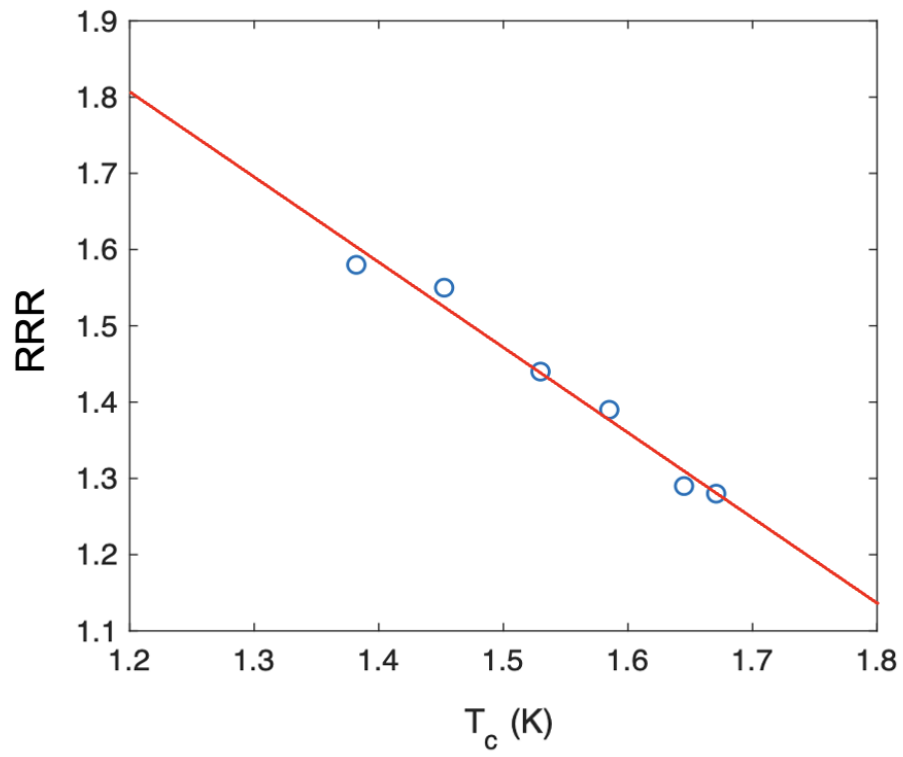


Figure 5.11: Plot showing measured film residual-resistance ratio RRR (blue points) versus T_c . Red line is a guide to the eye.

Chapter 6

Experimental Setup

This chapter provides an overview of the experimental setup and procedures that I used to transmons. I first describe the dilution refrigerator, and then discuss the microwave wiring and filtering, the cryogenic amplifier, and room-temperature microwave equipment.

6.1 The Dilution Refrigerator Setup

To prevent thermal excitation of a superconducting qubit, we require

$$k_B T \ll \hbar \omega_q \ll 2\Delta. \quad (6.1)$$

When $\omega_q/2\pi \sim 4$ GHz, this gives a temperature T much less than 200 mK. Consequently, the device must be cooled well below this temperature. Our devices were typically cooled using a dilution refrigerator with base temperature of approximately 10-20 mK.

The experiments were carried out in an Oxford Triton 200 series dry dilution refrigerator [1]. The refrigerator was in a shielded room in the Toll's Physics Building's sub-basement. The electrical connections, gas handling system, compressor, and pumps were outside the shielded room. Electrical connections between the outside and inside the room were carefully shielded and filtered.

The Oxford refrigerator (see Fig. 6.1) has five stages that operate at successively reduced temperatures: the outer-vacuum chamber is 300 K, the first pulse tube stage (PT1) was at 45 K, the second pulse tube stage (PT2) was at 3.2 K, the still is 700 mK, the cold plate runs at about 100 mK, and the mixing chamber (MXC) reaches 10-20mK. The mixing chamber can also

be heated to allow measurements to be made at higher temperatures, such as those I describe in the following chapters.

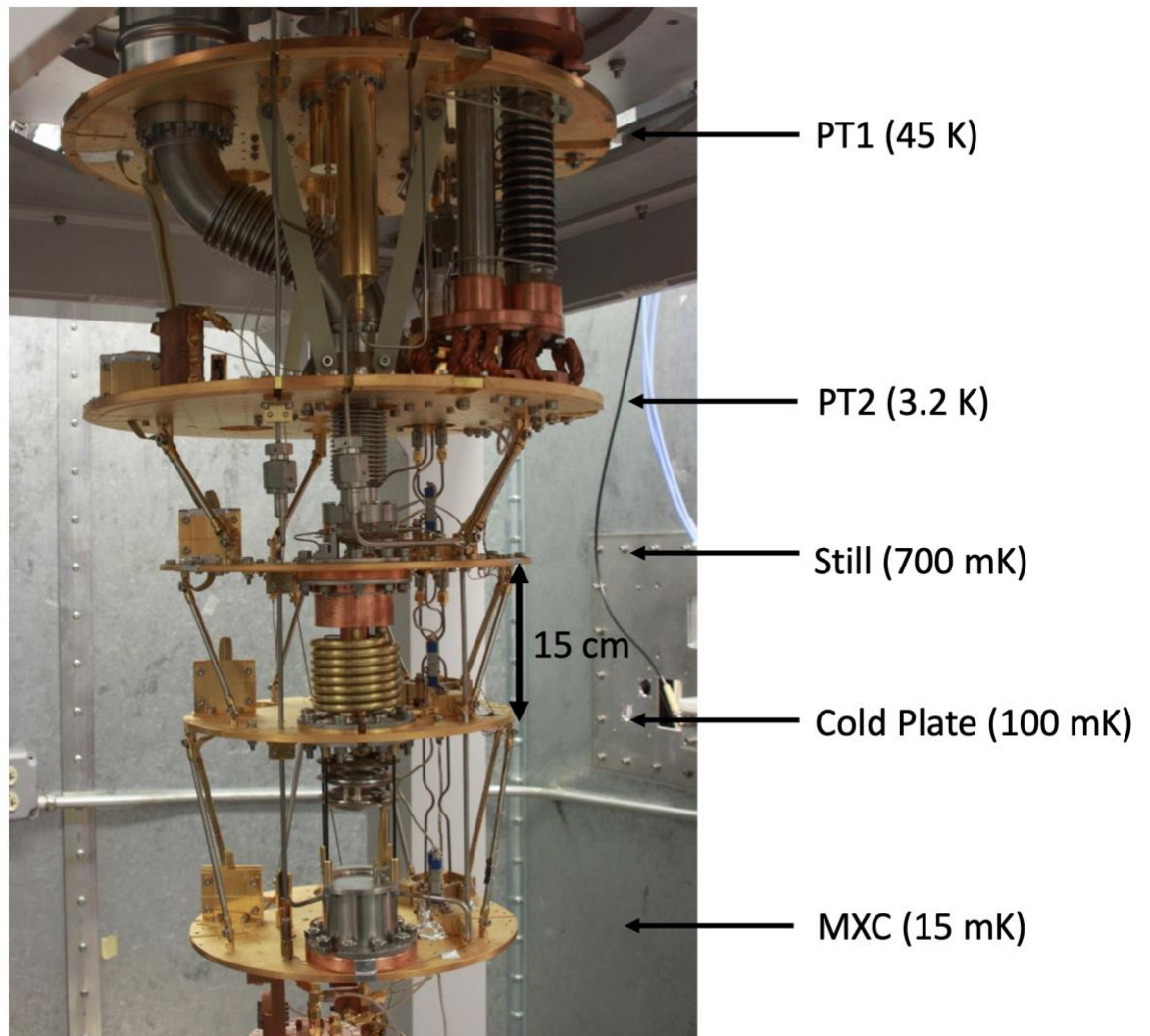


Figure 6.1: Picture of Oxford Triton 200 dilution refrigerator. Each stage is labeled with its name and operating temperature.

The refrigerator has heat shields that are attached to the various stages. The outermost shield of the Oxford refrigerator is just the aluminum outer vacuum container (OVC), which is at room temperature. A Cryomech pulse tube cooler cools down the first two stages. Each pulse tube stage has an aluminum shielding can. The still plate has a copper radiation shielding can. In addition to these shields, we used a Cu cylinder shield, mounted to the mixing chamber at 15 mK. The 3D cavity and device were surrounded by this shield. The interior of this shield was coated with SiC and epoxy to absorb stray infrared light [2].

Our transmons are somewhat sensitive to changes in magnetic field. It is therefore critical to shield the devices from stray fields. Our setup used two high-permeability magnetic shields. Both shields were borrowed from Dr. Ben Palmer. One shield was attached to the exterior of the OVC at room temperature, while the other was mounted to the Cu-shield on the MXC stage at 20 mK (see Fig. 6.2). RuO₂ is used as thermometer to monitor the temperature in the MXC.

6.2 Input and Output Microwave Lines

Our microwave setup for measuring transmons is shown in Fig. 6.3. The input microwave drive line is constructed from short lengths of rigid UT-85 coaxial cable with stainless steel inner and outer conductor [3] to prevent thermal coupling between different stages of the refrigerator. Each section of the line has Midwest Microwave attenuators [4] in order to thermalize the signal on its way down and attenuate external Johnson-Nyquist noise from high-temperature stages. The PT1 stage attenuator was 10 dB, PT2 was 20 dB, and the still attenuator was 6 dB. This resulted in a total attenuation of 36 dB between 300 K and 15 mK just due to the fixed attenuators; the lines contributed additional attenuation. The input line goes to the mixing chamber and Flexible UT-85

(a)



(b)

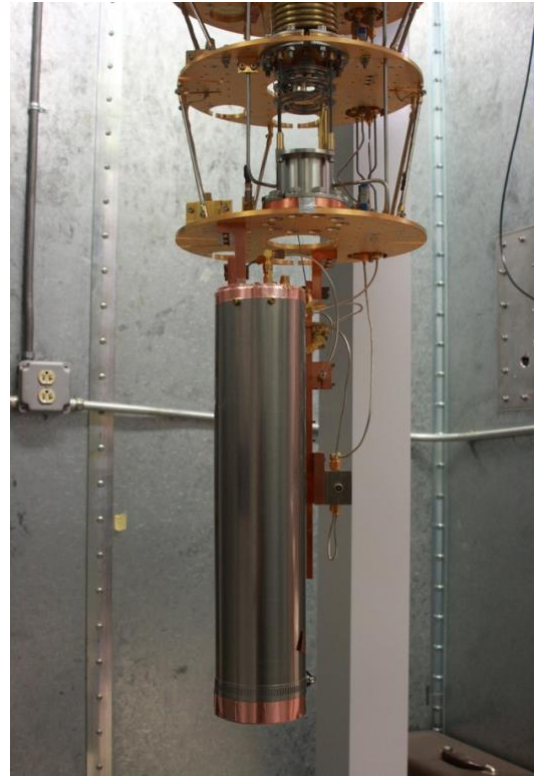


Figure 6.2: Picture of magnetic shields: (a) μ -metal magnetic shield attached to the exterior of OVC. (b) Inner A4K magnetic shield mounted to the Cu heat shield on the MXC.

coaxial cables were utilized between each component at this stage. Due to its flexibility, this was much simpler to deal with than the rigid stainless-steel lines, and it was much simpler to create suitable cable sections. Two 20 dB cryogenic attenuators were installed at the MXC (see Fig. 6.3). As a result, there was a total of 76 dB of fixed attenuation between the source and the cavity input pin. After the two 70dB attenuators, a 10.5 GHz low-pass filter from K&L [5] was used (see Fig. 6.3).

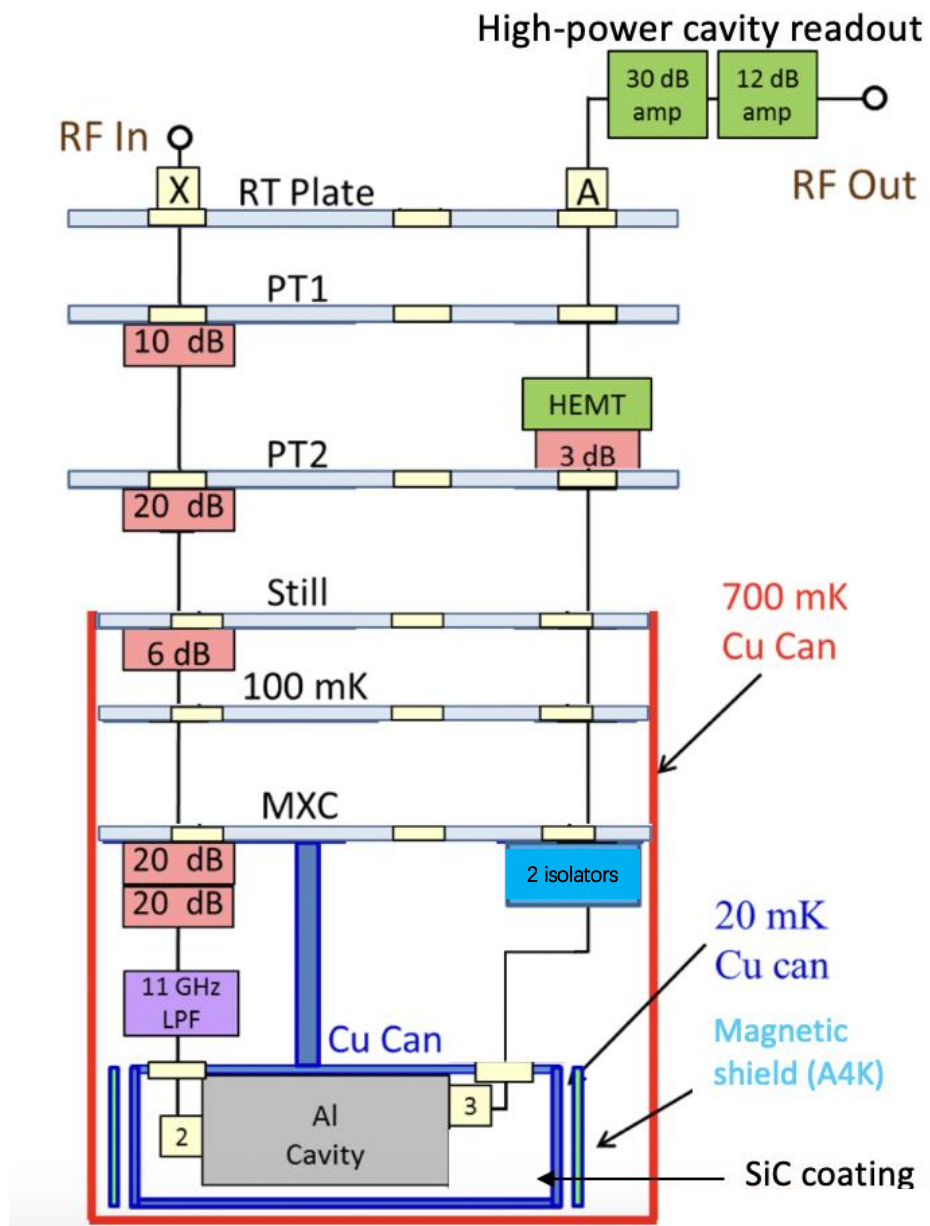


Figure 6.3: Schematic of refrigerator stages showing components on the input and output microwave lines.

The output transmitted microwave signal from the cavity returns to room temperature via a separate coaxial line (see Fig. 6.3). The output goes from the output port of the cavity to two Pamtek CTH1365KS cryogenic isolators [6] that are mounted on the MXC. These isolators, which have a rated range of 4 to 8 GHz, restrict the output line's bandwidth. They each provide 18 dB of isolation from waves traveling in the wrong direction. A HEMT (high electron mobility transistor) amplifier [7] was installed at the PT2 stage to amplify the output signal. The amplifier has a nominal gain of 32 dB, a bandwidth of 4–12 GHz, and a noise temperature of less than 5 K. A 3dB attenuator was put just before the HEMT to help match the input impedance. The output line leaves the refrigerator and travels to a room-temperature Miteq AMF-3F-04000800 low-noise amplifier [8] with a gain of 30 dB and a bandwidth of 4-8 GHz. This amplifier's output was routed to a Mini-Circuits ZX60-14012L+ amplifier [9] with a gain of 12 dB and a bandwidth of 300 kHz to 14 GHz.

6.3 Room Temperature Electronics Setup

Figure 6.4 schematically shows the setup of the room-temperature electronics that I used for measuring transmons. This setup was initially put together by R. Budoyo [10]. The instruments on the left side of Fig. 6.4 were used to control the timing of the pulses and to create various microwave signals. The components on the right side of Fig. 6.4 were used for readout. A 10 MHz reference signal was provided by a Stanford FS725 Rb frequency standard [11]. Using this reference signal, all the measurement components were time-synchronized and stable. This signal also ensures that all parts of the measurement system are synchronized to work together properly.

The repetition rate of the experiment was set by an Agilent 33120A arbitrary waveform generator (AWG) [12]. The AWG created a TTL signal with a frequency matching the repetition rate, which was typically set at 1 kHz. A Stanford DG535 pulse generator [13], which controlled

the timing of the pulse, was triggered using this TTL signal. Agilent E8257D, Agilent 83731B, and Agilent 83732B microwave sources were used to supply qubit drive and cavity readout tones [12]. Pulses from a Stanford Instruments DG535 were used to modulate the first two sources to produce the cavity and the qubit pulses, respectively. A constant Local Oscillator (LO) reference signal that matched the frequency of the cavity source was provided by the third source. The output from the cavity was monitored using homodyne detection [14]. A Dell Windows PC with a National Instruments PCI-GPIB card was used to link all the sources, pulse generators, and the AWG [15]. This configuration allowed us to adjust the measurement parameters via the computer running MATLAB software.

A MAC Technologies C3205-30 directional coupler [16] was utilized to combine the pulses produced by the cavity and qubit sources (see Fig. 6.3). This coupler provided 30 dB coupling and runs between 4 and 8 GHz. The pulses passed through the screen room wall to the top plate of the refrigerator, and then to the refrigerator's input line. The output signal emerged from the refrigerator's output line, where it was further amplified by two amplifiers (See. Fig. 6.3). Using a Marki IQ0318L IQ mixer, the boosted signal was mixed with the LO signal. The mixer supplied two output ports: one for the in-phase (I) port and the other for the quadrature (Q) port. The signals from these two outputs were amplified using two Stanford SR560 preamplifiers after passing through two identical sets of low-pass filters [13]. Finally, the output I and Q signals were sent to a National Instruments BNC-2110 breakout box [15] at the shield room wall. From there, the I and Q signals were measured by a National Instruments PCI-6115 data acquisition card (DAQ).

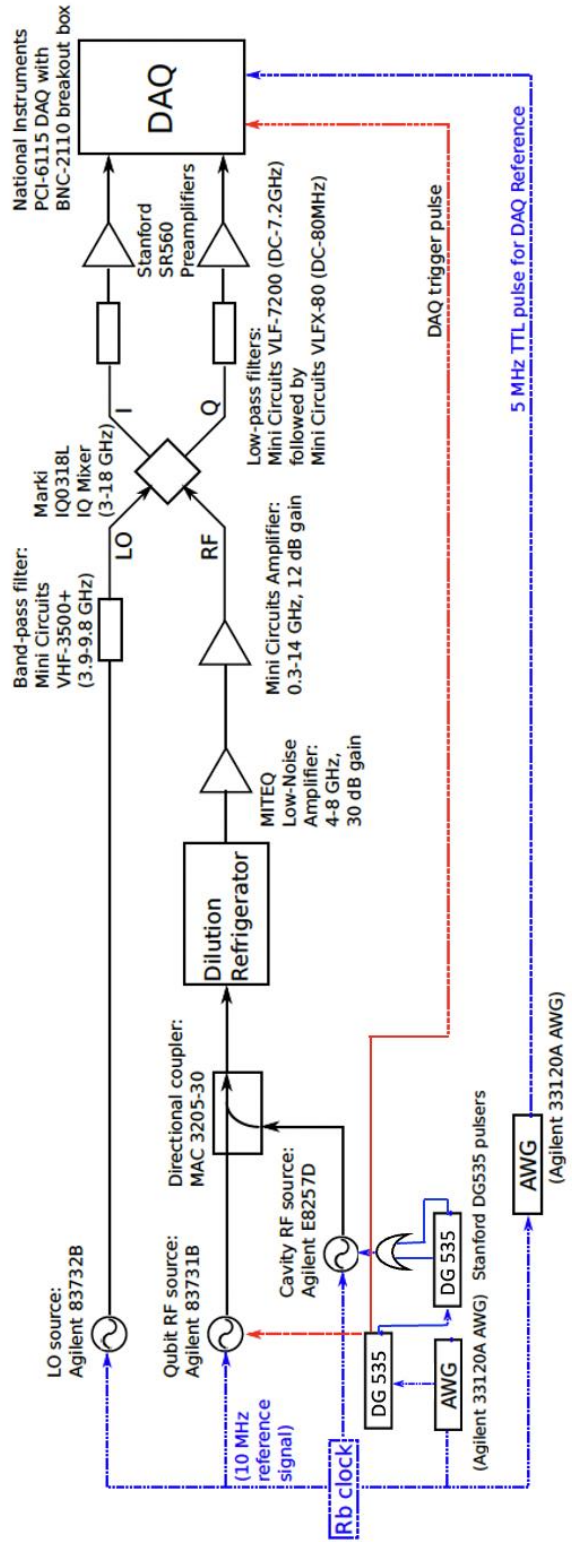
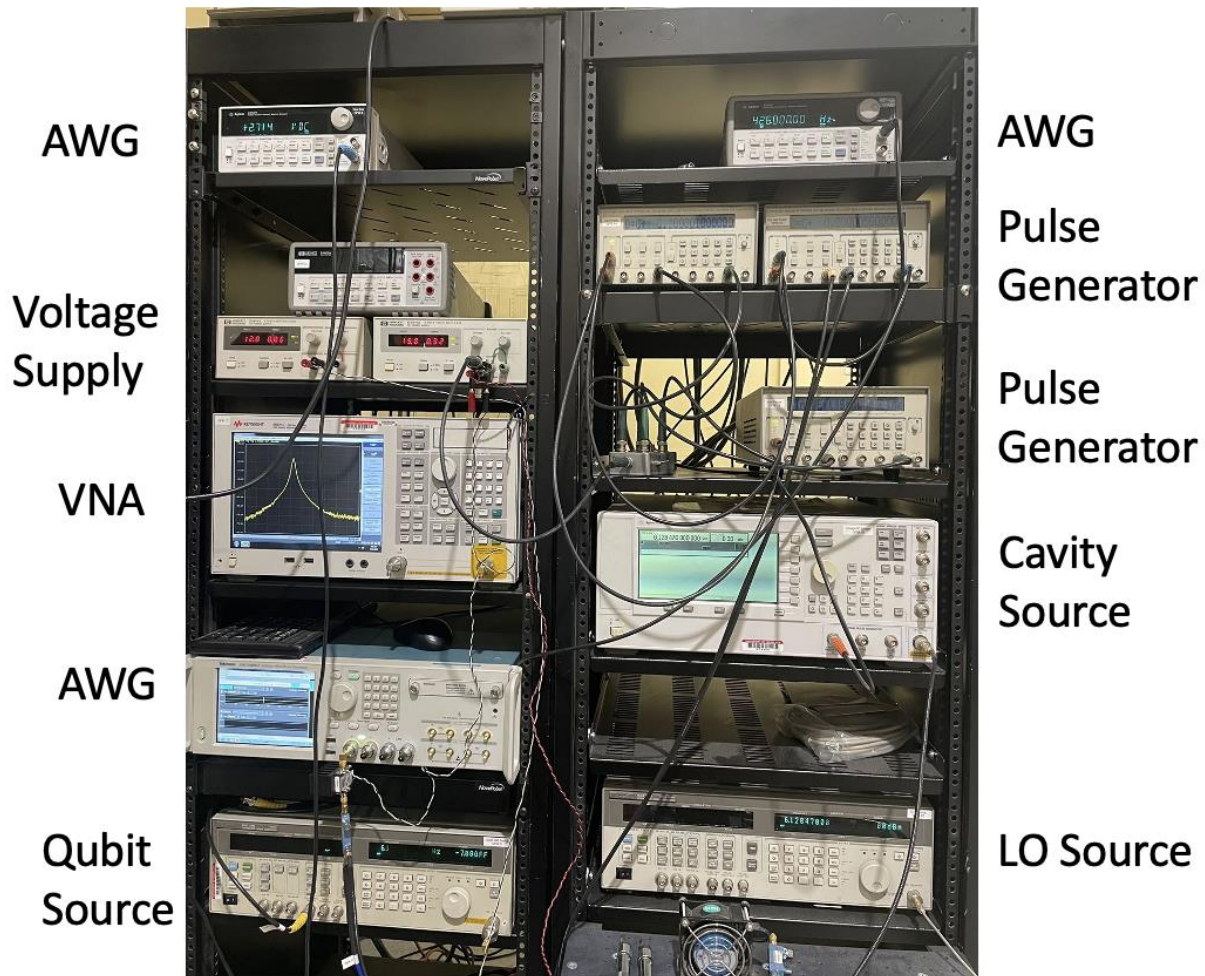


Figure 6.4: Room temperature microwave setup for qubit measurements [10]. The blue dotted lines are the timing portion of the circuit.

The data acquisition card (DAQ) performed the essential task of digitizing the I and Q signals. This transformed the analog signals into digital data for later processing. The data acquisition was set to a rate of 5 million samples per channel per second (5 M samples/channel/s), determined by a 5 MHz TTL signal that emanated from an Agilent 33120A arbitrary waveform generator (AWG). Finally, Fig. 6.5 shows a photograph of the room temperature instrument rack.

Figure 6.5: Photograph of rack with microwave pulse control and qubit readout setup.



Chapter 7

Characterization of Two Transmons

In this chapter, I first describe Dr. Sudeep Dutta and my measurements of the transition spectrum on chip SKD102. This chip was sealed in 3D Al microwave cavity SI-2 and there were two transmons on the sapphire chip (see Chapter 5). I next discuss characteristic time measurements, including Rabi oscillations, the qubit relaxation time T_1 , the spin echo time T_2 , and Ramsey oscillations for these two transmons.

7.1 Measurement Details

Chip SKD102 was measured inside the dilution refrigerator in Room SB0331 of the Toll Physics Building. The high-power readout method (see section 2.5) was used for these measurements.

Each measurement involved the application of a sequence of pulses. Each sequence of pulses started with a cavity pulse that helped calibrate the system's transmission when the transmons were in the ground state. The sequence then paused for a delay time of Δt (of order 1 ms) to allow the system to relax enough for spectroscopic measurements. Following this, qubit manipulation pulses were then applied. After this, a cavity measurement pulse was applied and the amplitude of the transmitted pulse was measured to determine whether the qubit was in the ground state or the excited state. This general pulse sequence is shown in Fig. 7.1.

After both the calibration cavity pulse and the measurement cavity pulse, the amplified transmitted signal was passed to an I-Q (in and out of phase) mixer. The output voltage amplitudes

V_I and V_Q were measured by mixing them with the reference signal from the cavity drive source (see Chapter 6.3). The amplitude of the transmitted output voltage is the magnitude of the coupled voltage:

$$V_t = \sqrt{V_I^2 + V_Q^2}. \quad (7.1)$$

I define V_0 to be the measured voltage amplitude of the transmitted calibration cavity pulse and V_f to be the measured voltage amplitude of the second measurement cavity pulse. Most of my basic qubit measurements were based on measuring V_0 and V_f and I often presented these results as a fractional voltage difference:

$$\frac{\delta V}{V_0} = \frac{V_f - V_0}{V_0}. \quad (7.2)$$

This quantity is the scaled difference between the two pulse voltages and is proportional to the probability to be in the excited state P_e . I typically averaged for ~ 1000 shots.

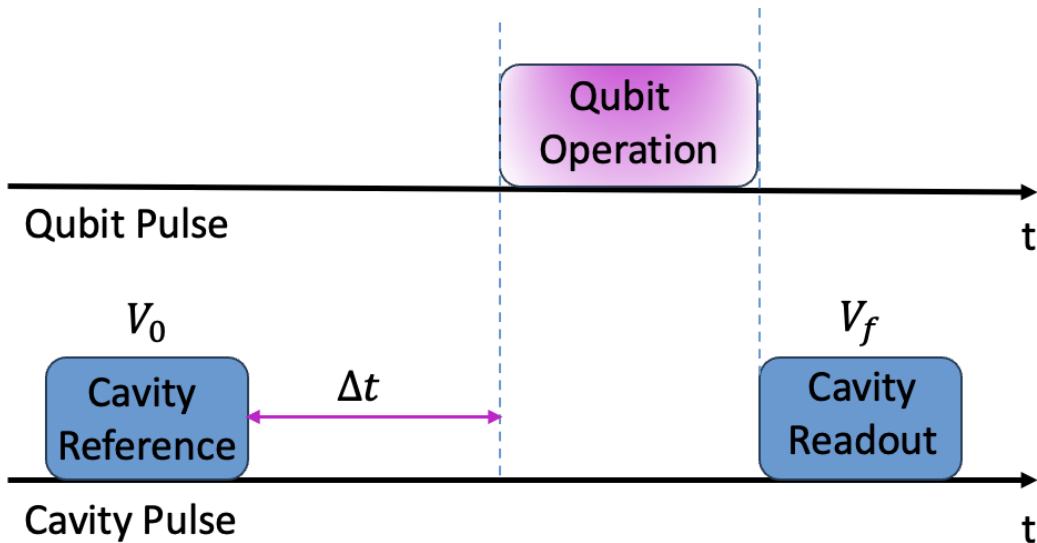


Figure 7.1: General applied pulse sequence for qubit manipulation and state measurements

7.2 Cavity Characterization

After cooling the device to base temperature, the first thing I measured was the cavity resonance with the qubits in the ground state. I used a vector network analyzer (VNA) to measure the transmission S_{21} as a function of frequency and power of the rf signal. This setup is different from the homodyne pulse that I used for qubit manipulation. The output power was supplied by a Keysight E5071C VNA [1] which operated within a frequency range of 900 kHz to 8.5 GHz with a power range of -55 dBm to 10 dBm. The VNA's first output port was linked to the rf input port on the refrigerator's top panel. The VNA's second port was connected to the rf output of the Mini-Circuits amplifier (see Fig. 6.3). For the cavity resonance measurement, the VNA determined $|S_{21}| = |V_{\text{out}}/V_{\text{in}}|$ as a function of frequency and power by measuring the ratio of the microwave output signal (with amplitude V_{out}) to the input signal (with amplitude V_{in}).

By sweeping the frequency and incrementally increasing rf power, I was able to determine the bare cavity frequency $\omega_C/2\pi$ (at high power) and the dressed cavity frequency $\tilde{\omega}_C/2\pi$ (at low power). This let me confirm that the qubit was functioning as expected and also provided an estimate for the dispersive shift [2]

$$\chi_{ge} = \omega_C - \tilde{\omega}_C^{(g)}. \quad (7.3)$$

Figure 7.2 presents a false-color power map of the cavity, with frequency plotted along the x-axis, the power applied by the vector network analyzer (VNA) along the y-axis, and $|S_{21}|^2$ represented by the color bar. There is a prominent peak at high power centered at 6.1155 GHz. This is the bare resonance of the cavity $\omega_C/2\pi$. At low power, the resonance peak shifts to approximately 6.1219 GHz. This is the dressed peak of the cavity. It is important to note that this shift in frequency is due to the coupling of the cavity to both transmons. From the cavity map, we

see that total dispersive shift due to both transmons is 6.4 MHz. Since the qubit frequencies are different, this will lead to a different contribution to the dispersive shift from each qubit due to the different detuning. Nevertheless, simulations show that the total dispersive shift is pretty close to the sum of each qubit's dispersive shift, i.e. for each qubit, $\chi_{ge}/2\pi \approx 3.2$ MHz. This frequency shift confirmed that at least one qubit was functioning. This plot is from the chip's initial cooldown.

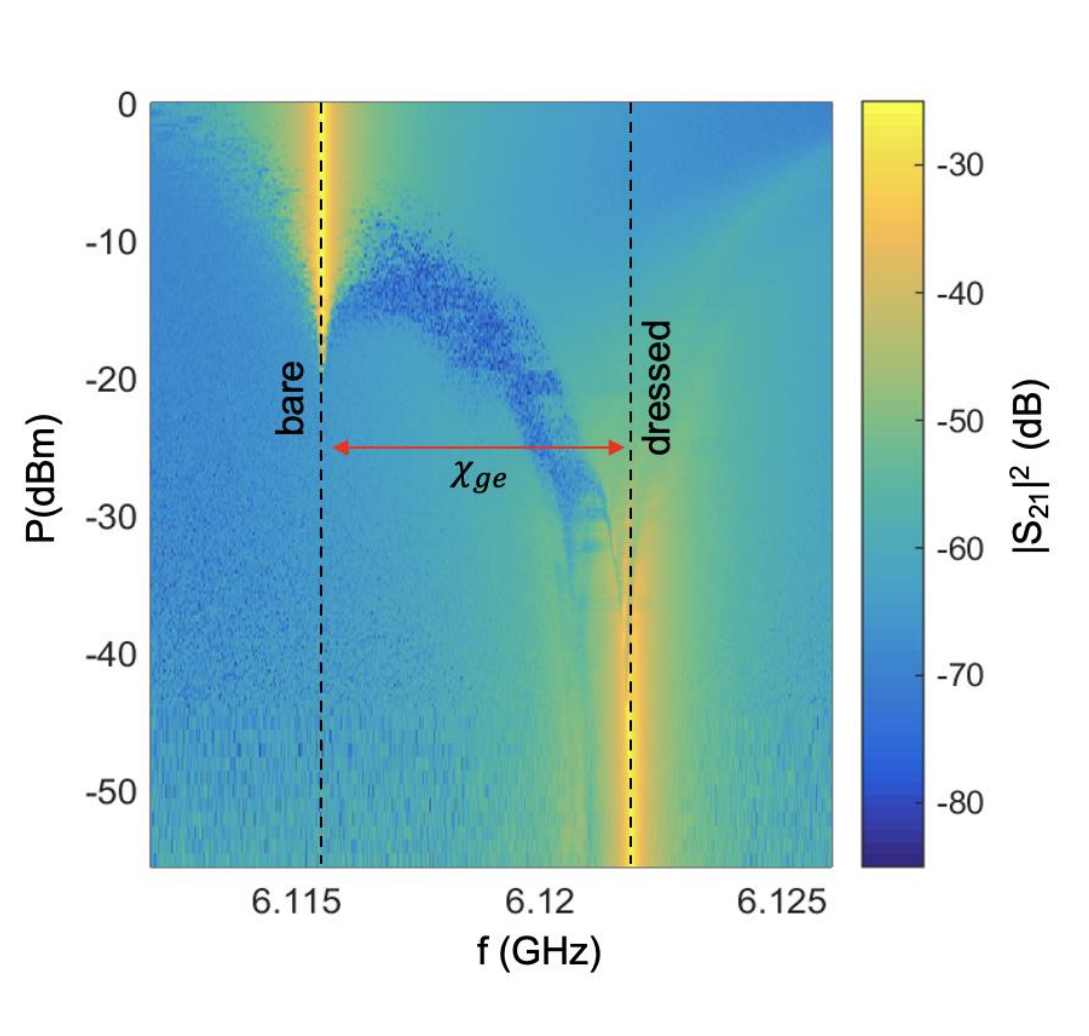


Figure. 7.2: Cavity power map $|S_{21}|^2$ of chip SKD102 in cavity SI-2a. This false-color map shows $|S_{21}|^2$ as a function of frequency and rf power applied by the VNA. The main cavity transition peaks are the bare transit at 6.115GHz and dressed peak at 6.122 GHz, which are indicated by the dashed lines.

Figure 7.3 shows several frequency line cuts through the $|S_{21}|^2$ data presented in Figure 7.2. The left peak corresponds to a VNA power of -10 dBm (black curve), which falls in the bare peak regime. Other line cuts are for VNA powers of -45 dBm (red curve), -50 dBm (green curve), and -55 dBm (blue curve), falling within the dressed peak regime. Fitting the bare peak to a Lorentzian yields a center frequency of $\omega_c/2\pi = 6.11552$ GHz and a loaded quality factor $Q = 49,000$. Similarly, fitting the dressed peak results in $\tilde{\omega}_c/2\pi = 6.12189$ GHz and a loaded quality factor of $Q = 48000$. Thus, the quality factor of the dressed peak was slightly lower than that of the bare resonance, suggesting additional loss in the low-power limit or the existence of additional dephasing when the qubit was coupled to the cavity.

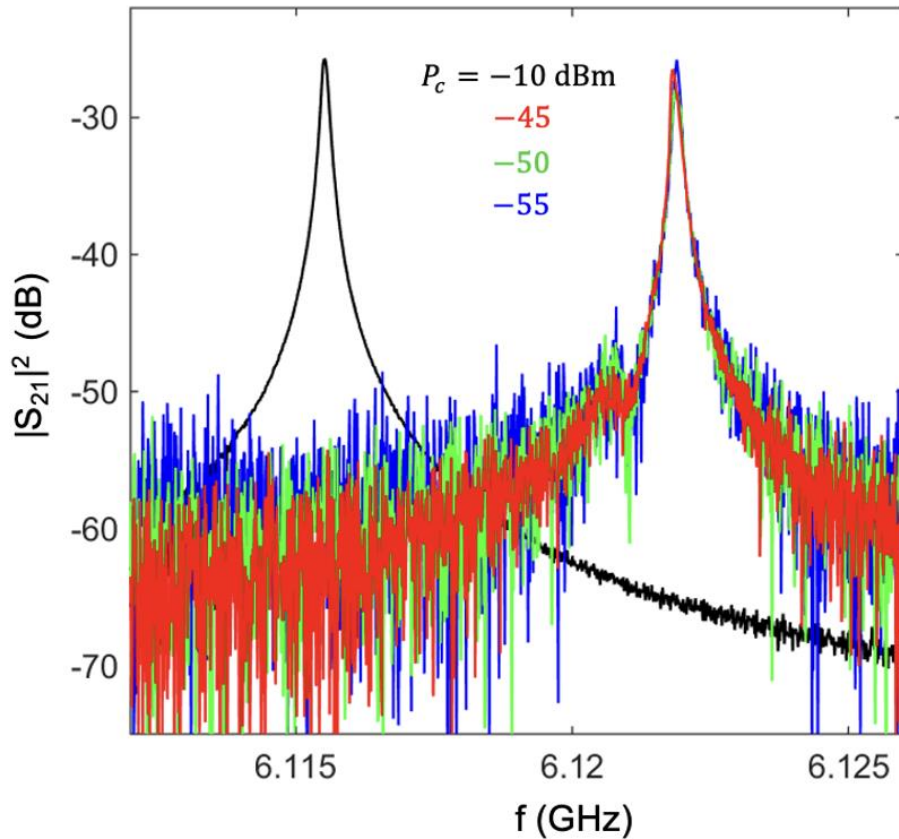


Figure 7.3: Line cuts through plot in Fig. 7.2 showing $|S_{21}|^2$ as a function of frequency for four applied powers P_c .

7.3 Qubit Spectroscopy

The qubit transition frequencies ω_{ge} and ω_{gf} can be measured using spectroscopy with a homodyne pulse sequence. This measurement starts with a cavity reference pulse at cavity frequency $f_c = 6.1155 \text{ GHz}$ and cavity power $P_c = 3 \text{ dBm}$ to acquire the background transmission S_{21} , followed by an idle interval. Then a qubit tone with a long pulse length and moderate power was used to perform qubit spectroscopy. This was followed by a pulsed homodyne measurement with a high drive qubit power of 16 dBm at the bare cavity peak (see Fig. 7.1).

Figure 7.4 shows two spectroscopic plots of $\Delta V/V$ for the two transmon qubits Q_{L1} and Q_{R1} on SKD102 using a high-power readout. In both cases, a broadened $|g\rangle \leftrightarrow |e\rangle$ peak and a two-photon $|g\rangle \Rightarrow |f\rangle$ peak are visible. In the plot, the qubit with high $|g\rangle \leftrightarrow |e\rangle$ transition frequency occurs at $\omega_{ge}/2\pi \sim 3.7739 \text{ GHz}$ and a two-photon transition from $|g\rangle \Rightarrow |f\rangle$ occurs at $\omega_{gf}/4\pi \sim 3.6746 \text{ GHz}$. The charging energy can be roughly estimated from this data using $E_c/h \simeq 2(\omega_{ge}/2\pi - \omega_{gf}/4\pi) \simeq 198.5 \text{ MHz}$. The other qubit has a $|g\rangle \leftrightarrow |e\rangle$ transition frequency at $\omega_{ge}/2\pi \sim 2.9297 \text{ GHz}$ and a two-photon transition from $|g\rangle \Rightarrow |f\rangle$ occurs at $\omega_{gf}/4\pi \sim 2.8172 \text{ GHz}$. The charging energy is roughly $E_c/h \simeq 2(\omega_{ge}/2\pi - \omega_{gf}/4\pi) \simeq 225.0 \text{ MHz}$ (from anharmonicity). From the discussion in Section 5.3, the left qubit has a larger capacitance which corresponds to a smaller E_c . This difference makes it easier for us to distinguish the two qubits. Thus, the spectroscopy indicates that the low transition-frequency qubit is the gap-engineered one which we denote as Q_{L1} . The other qubit with higher transition frequency is a nominally standard transmon, which I denote as Q_{R1} (see Fig. 7.4). This is also consistent with the differences in E_j . I also note that for Q_{L1} , $|e\rangle \rightarrow |f\rangle$ is also visible, suggesting a significant thermal population in the $|e\rangle$ state for Q_{L1} .

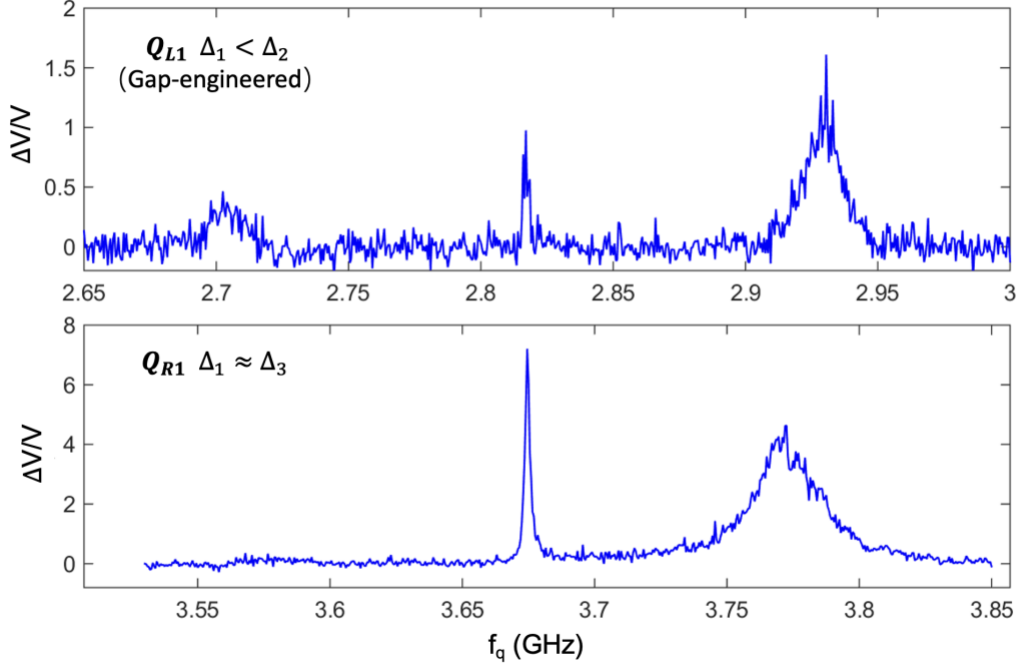


Figure 7.4: Qubit spectroscopy of the gap-engineered transmon Q_{L1} (top) and the nominally standard transmon Q_{R1} (bottom) at high qubit drive powers with qubit transition $\omega_{ge}/2\pi \sim 3.7739$ GHz and $\omega_{gf}/4\pi \sim 3.6746$ GHz for Q_{R1} and $\omega_{ge}/2\pi \sim 2.9297$ GHz and $\omega_{gf}/4\pi \sim 2.8172$ GHz for Q_{L1} .

7.4 Rabi Oscillations

A Rabi oscillation [3], involves driving cyclic transitions between the states $|g\rangle \leftrightarrow |e\rangle$ using a nearly resonant drive. In the absence of dissipation and dephasing, driving a qubit at the $|g\rangle \leftrightarrow |e\rangle$ transition frequency causes a sinusoidal oscillation of the system's state between the two levels [4]. The process I used to measure Rabi oscillations used the pulse sequence depicted in Fig. 7.5,

where the qubit tone pulse duration t_{Rabi} at ω_{ge} is applied with varying Rabi pulse lengths. Figure 7.6 shows plots of 250 kHz Rabi spanning an 80 μs duration for the two transmons on chip SKD102. Due to decoherence, the amplitude of the Rabi oscillations decay with a time constant T' .

The waveform can be fit to a function of an exponentially decaying sine wave

$$P_{|e\rangle} = Ae^{-\frac{t}{T'}} (1 - \cos(\Omega_R t)) + C. \quad (7.4)$$

The constants A and C are the amplitude of the oscillation and the steady-state population, respectively. The two curves shown in Fig. 7.6 have $T' \simeq 50 \mu\text{s}$. Note that for a frequency-independent loss and dephasing, the decay time of the Rabi oscillation is related to T_1 and T_2 by [5]

$$\frac{1}{T'} = \frac{1}{2T_1} + \frac{1}{2T_2}. \quad (7.5)$$

which implies that $T' \leq 4T_1/3$.

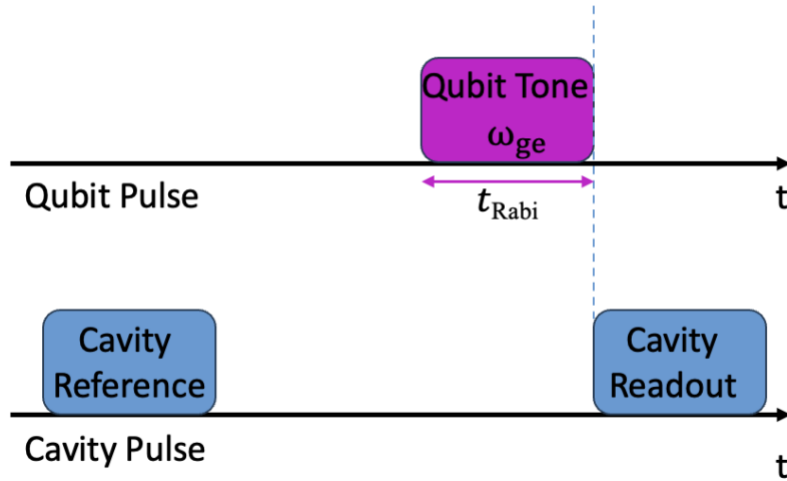


Figure 7.5: Pulse sequence for Rabi oscillation measurements. The qubit tone pulse length t_{Rabi} is varied for Rabi measurements.

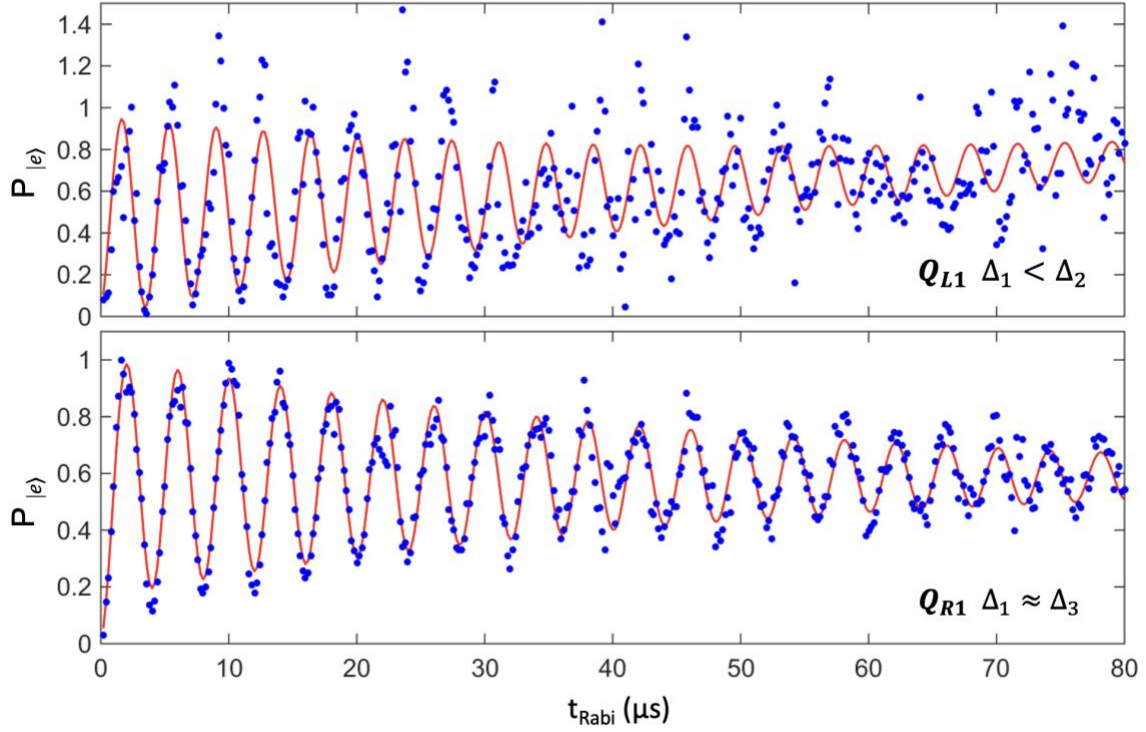


Figure 7.6: Rabi Oscillation decay measurements for transmons Q_{L1} and Q_{R1} with 250 kHz Rabi frequency. The red curves are fits to an exponential decaying sine wave. $T' \simeq 50 \mu\text{s}$ for both devices.

7.5 Relaxation Time T_1

To measure the relaxation time T_1 , I first applied a $1 \mu\text{s}$ cavity pulse to and measured its transmission through the cavity (see Fig. 7.7), the magnitude of this output voltage is V_0 . A calibrated π -pulse was then applied with a length t_π (calibrated using the Rabi oscillations discussed in Sec. 7.4). This π -pulse puts the qubit into its excited state. I then waited for a time Δt and measured the amplitude of the transmitted cavity pulse V_q . To correct for drift, I also measured the transmission through the cavity of a π -pulse. The transmitted amplitude of this pulse was V_π .

Before measuring V_π , I also repeated the measurement of the transmitted amplitude V_g when the system was in ground state. Typically, this process was repeated around 1000 times and the results were averaged to determine the population of the qubit in the excited state $|e\rangle$ at the specified time delay Δt using:

$$P_{|e\rangle} = \frac{\langle V_q \rangle - \langle V_0 \rangle}{\langle V_\pi \rangle - \langle V_g \rangle}. \quad (7.6)$$

These steps were repeated for different Δt to obtain $P_{|e\rangle}$ as a function of Δt . I fit my results to

$$P_{|e\rangle} = Ae^{-\frac{\Delta t}{T_1}} + C, \quad (7.7)$$

where $A \sim 1$ is the initial $|e\rangle$ state occupancy and $C \sim 0$ is the steady state occupancy or residual thermal $|e\rangle$ state occupancy.

Figure 7.8 shows relaxation measurements of the two qubits on chip SKD102 at the base temperature of about 20 mK. Fitting to Eq. (7.7) to my result, for Q_{L1} yielded $T_1 = 181 \mu\text{s}$ and Q_{R1} yielded $T_1 = 84 \mu\text{s}$. Repeated measurements showed substantial fluctuations in T_1 on successive days, as I discuss in Chapter 8.

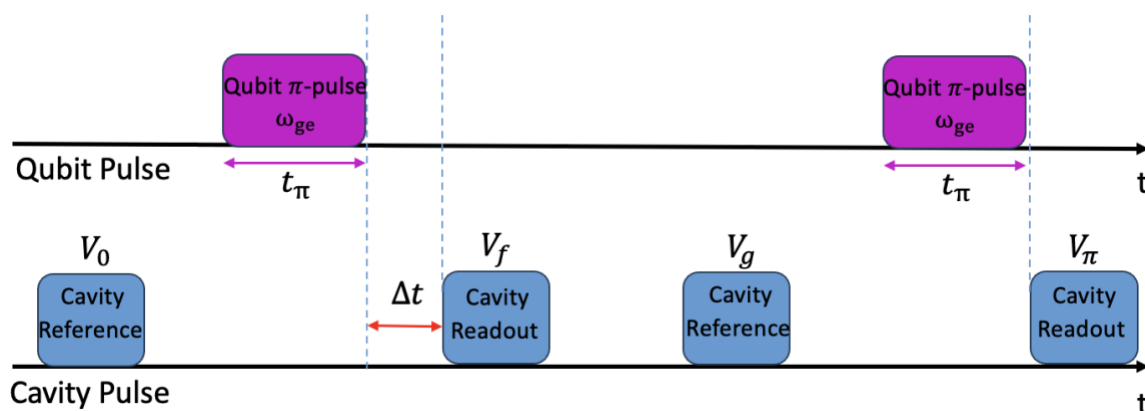


Figure 7.7: Applied pulse sequence for relaxation time T_1 measurements. The delay time Δt is varied. Four transmitted amplitudes V_q, V_0, V_π, V_g are measured to obtain $P_{|e\rangle}$ at delay time Δt

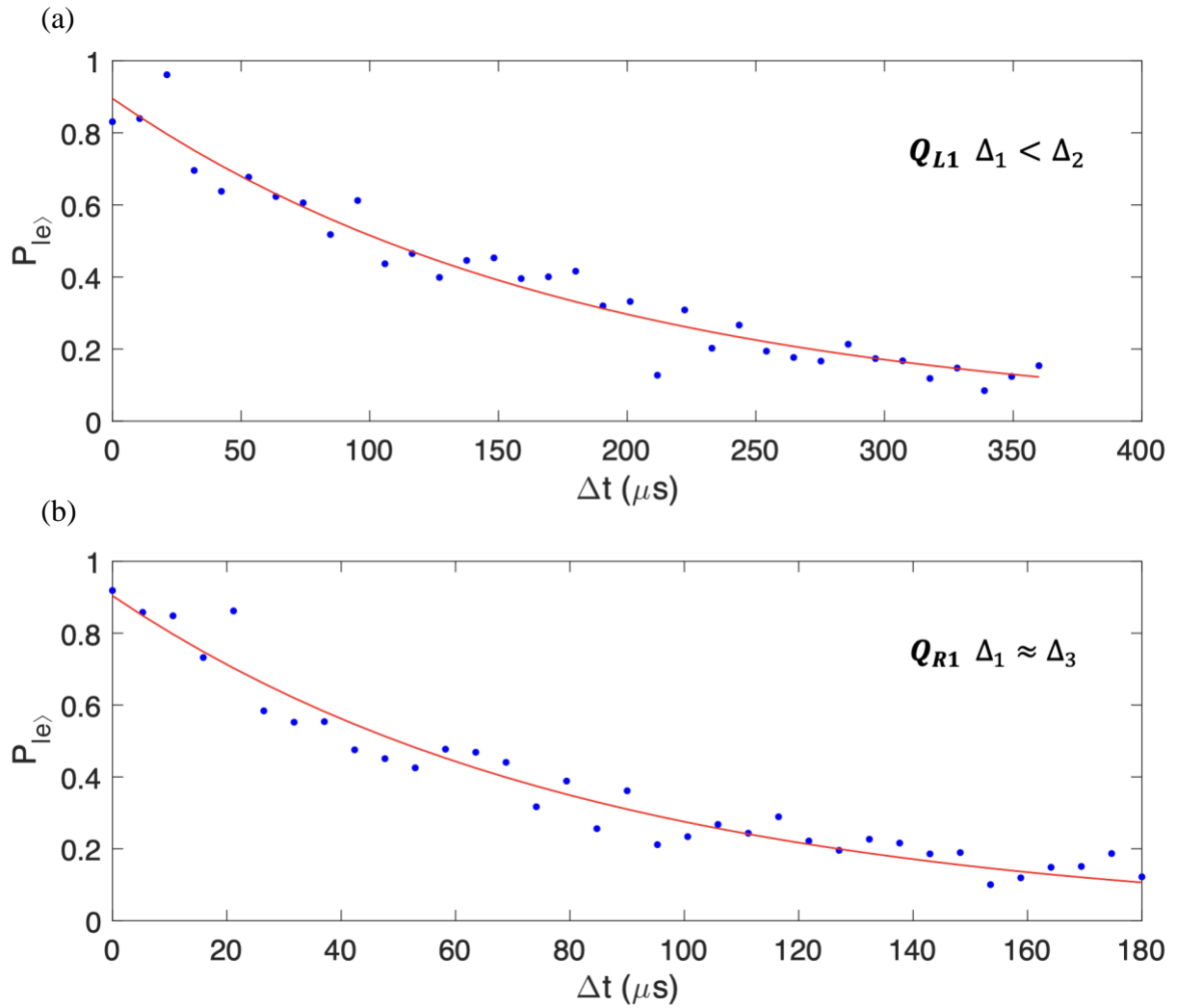


Figure 7.8: Blue points show one relaxation measurements for transmons (a) Q_{L1} and (b) Q_{R1} . The red curves are fits to an exponential decay. The fits yielded $T_1 = 181 \mu s$ for Q_{L1} and $T_1 = 84 \mu s$ for Q_{R1} .

7.6 Spin Echo T_2

The spin-echo technique, pioneered by Erwin Hahn [5], was designed to counteract inhomogeneous broadening in nuclear magnetic resonance (NMR). Hahn realized that inhomogeneities in the magnetic field were leading to significant spectral broadening [6], and this could be removed by using a clever pulse sequence. The dephasing that was not removed causes the resulting signal to decay with a characteristic time T_2 , called the spin-echo time.

Figure 7.9 shows the pulse sequence I employed for spin-echo measurement. I first applied a $1 \mu\text{s}$ cavity pulse V_0 and measured the amplitude V_0 of three pulses transmitted through the cavity. I next applied a $\pi/2$ pulse to drive the qubit to the x-axis on the Bloch sphere. The system then evolved for an interval $\Delta t/2$, followed by a π -rotation around the x-axis. Assuming no decoherence or relaxation, this pulse aligns the state vector with the positive y-axis in the co-rotating frame. Then the system again is allowed to evolve for a time $\Delta t/2$. A final $-\pi/2$ rotation, in the clockwise direction around the x-axis, is executed. The system is then measured, resulting in a signal magnitude of V_f . I also measured the response of the system with a π -pulse labelled as V_π without time delay ($\Delta t = 0$) and its background reference pulse signal V_g .

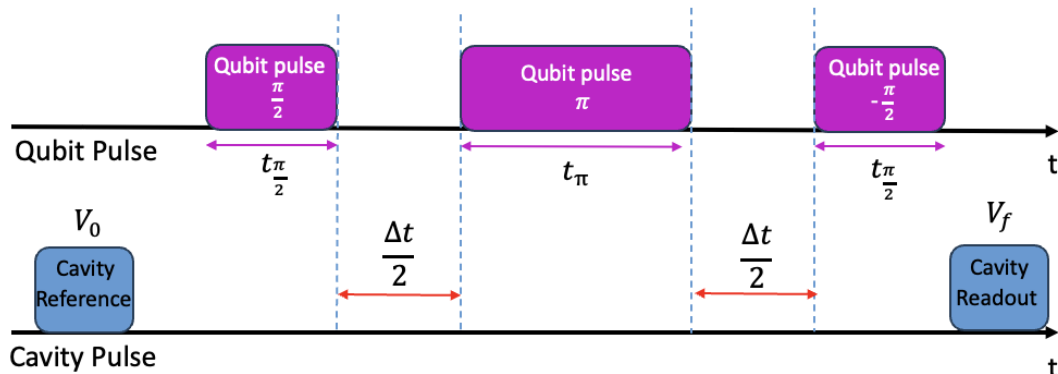


Figure 7.9: Applied pulse sequence for spin echo T_2 measurements. The delay time Δt is varied.

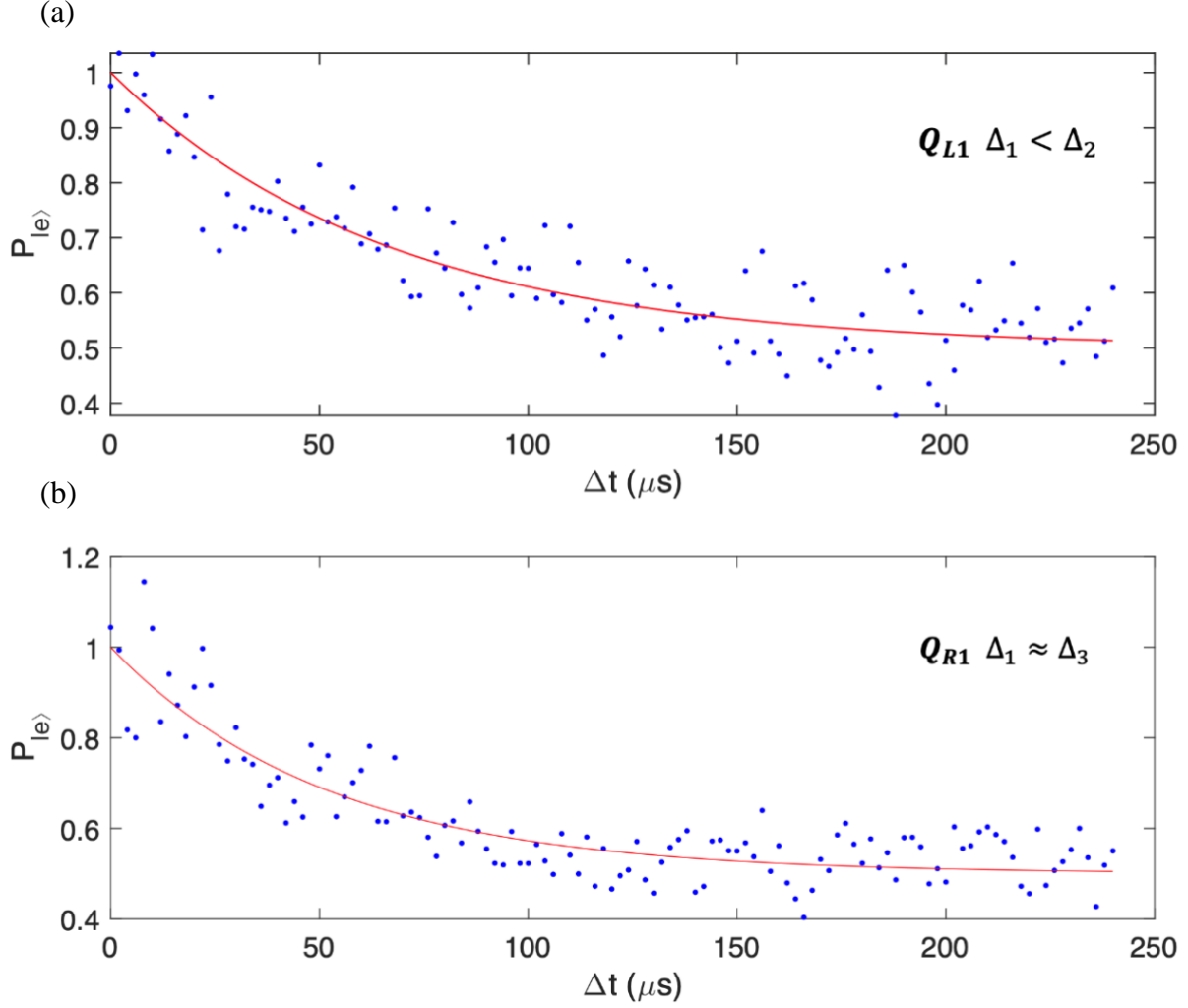


Figure 7.10: Spin echo measurements (blue points) for transmons (a) Q_{L1} and (b) Q_{R1} on chip SKD102. The red curve indicates the fit to an exponential decay. The fittings yielded $T_2 = 66.5 \mu\text{s}$ for Q_{L1} and $T_2 = 51.9 \mu\text{s}$ for Q_{R1} .

In an ideal scenario without any decoherence, this sequence would leave the qubit in its excited state. However, the real system experiences decoherence, which reduces the probability of finding the system in the excited state. The average final signal was fit to

$$P_{|e\rangle} = A e^{-\frac{\Delta t}{T_2}} + C_2, \quad (7.8)$$

where $A \sim 1$ is the initial $|e\rangle$ state occupancy, and $C_2 \sim 1/2$ is the expected steady-state occupancy.

Figure. 7.10 shows my fit to the spin echo data for qubits Q_{L1} and Q_{R1} on chip SKD102 at base temperature. I find $T_2 = 66.5 \mu\text{s}$ and $51.9 \mu\text{s}$, respectively. Note that T_2 is related to T_1 and the pure dephasing time T_ϕ by [5]

$$\frac{1}{T_2} = \frac{1}{2T_1} + \frac{1}{T_\phi}, \quad (7.9)$$

if the loss and dephasing are frequency independent. From the T_1 and T_2 values I measured for these two transmons, yields $T_\phi = 81.5 \mu\text{s}$ for Q_{L1} and $T_\phi = 75.0 \mu\text{s}$ for Q_{R1} .

7.7 Ramsey Oscillations

Norman Ramsey, a student of Isidor Rabi, first developed the method now called Ramsey interferometry [6]. This method allows highly precise measurement of the transition frequencies.

To measure a Ramsey Oscillation, I first apply a cavity pulse and measure the transmitted voltage V_0 (see Fig. 7.11). After letting the system evolve, I apply a $\pi/2$ -pulse, which rotates the qubit state around the x-axis. After this pulse, the system is given time Δt to evolve. Following this, another $\pi/2$ -pulse is applied around the x-axis, and the state is then measured by applying a cavity pulse and measuring the transmitted amplitude V_f . If $\Delta t = 0$, the effect is just a π -pulse, resulting in the qubit being left in the excited state. Conversely, if Δt is equal to $\pi/\Delta\omega$, which $\Delta\omega$ is the detuning, the state vector rotates by 180° along the equator. The subsequent $\pi/2$ -pulse then returns the state vector to its ground state. For $\Delta t > 0$, the qubit state can relax and dephase.

Ramsey fringes are typically generated by driving the qubit with a tone that is just slightly off its resonance. When the $\pi/2$ pulse deviates by $\Delta\omega$ from the qubit's resonant frequency ω_{ge} the qubit state precesses around the z-axis in the co-rotating frame, with the rotation angle being the

product of the detuning $\Delta\omega$ and the delay time Δt . The accumulated phase during Δt leads to a change in the final state's observed population P_e in the $|e\rangle$ state. Consequently, $P_{|e\rangle}$ oscillates with a frequency proportional to $\Delta\omega$. This oscillation decreases in magnitude with a time constant T_2^* called the Ramsey time constant in spectroscopic coherence time. These oscillations can be fit to:

$$P_{|e\rangle} = A \left(1 + e^{\frac{-\Delta t}{T_2^*}} \sin(\Delta\omega\Delta t) \right), \quad (7.10)$$

where A is the amplitude of the oscillations and $\Delta\omega$ is the detuning between the drive frequency and the qubit transition frequency.

Figure 7.12 shows the Ramsey oscillations produced by transmon Q_{R1} on chip SKD102 at the base temperature. From the fit, I find $T_2^* = 24.8 \mu\text{s}$ and detuning $\Delta\omega = 0.4 \text{ MHz}$. Note that the Ramsey oscillation of Q_{L1} was so noisy that it was hard to extract a T_2^* value.

By measuring Ramsey Oscillations for different detunings $\Delta\omega$, I could map out the behavior of the Ramsey fringes. The frequency of the oscillations should match the detuning, enabling a highly precise determination of the qubit frequency. By analyzing the oscillation frequency relative to the drive frequency, the transition frequency can be pinpointed where the Ramsey frequency becomes zero. Figure 7.13 shows an example of the Ramsey fringe measurement of Q_{R1} .

In general, the Ramsey decay is related to the T_1 relaxation and T_ϕ dephasing times by

$$\frac{1}{T_2^*} = \frac{1}{2T_1} + \frac{1}{T_\phi} + \frac{1}{T^\dagger}, \quad (7.11)$$

where T^\dagger is the time constant for inhomogeneous broadening [7]. Inhomogeneous broadening arises specifically from low-frequency noise in measurement-to-measurement variations. Inhomogeneous broadening, loss, and dephasing all play a role in determining the qubit's spectroscopic linewidth and T_2^* .

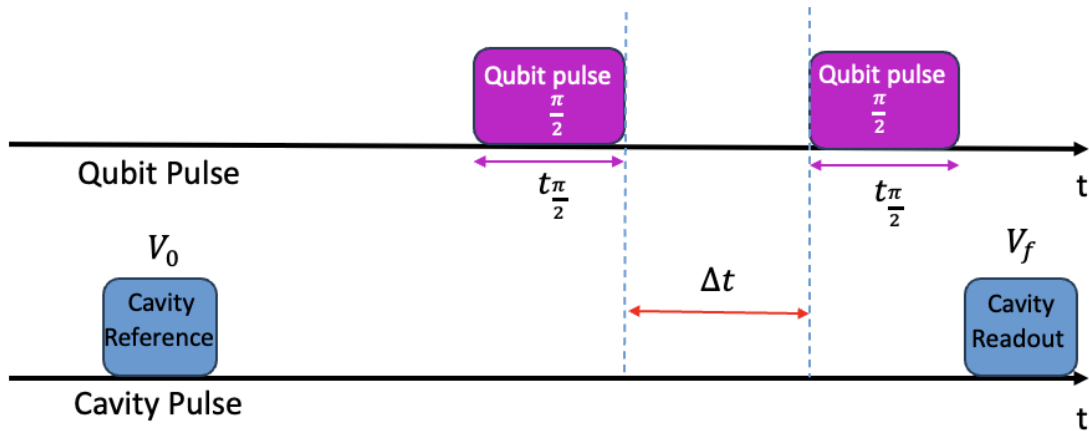


Figure 7.11: Pulse sequence for Ramsey Oscillation measurements. The delay time Δt is varied.

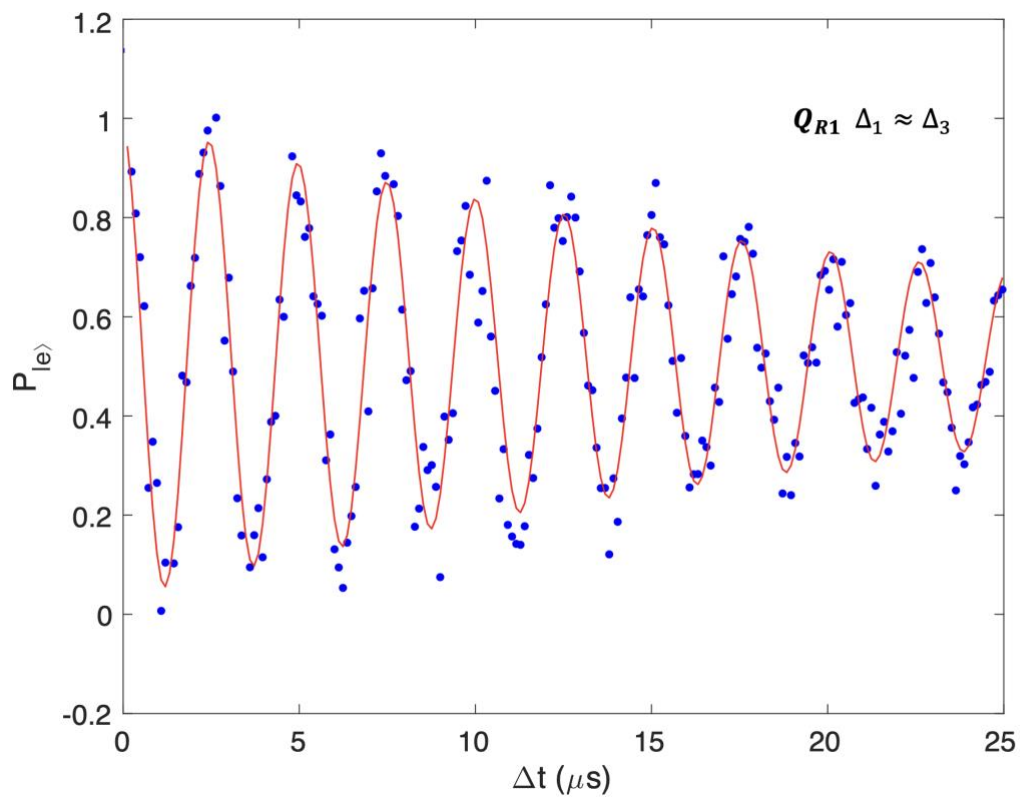


Figure 7.12: Measurement of the excited state population $P_{|e\rangle}$ versus Ramsey delay time Δt of Q_{R1} . The red curve indicates the exponential decay fit to the blue data points. The fit yielded $T_2^* = 24.8 \mu\text{s}$ with $\Delta\omega/2\pi = 0.4\text{MHz}$.

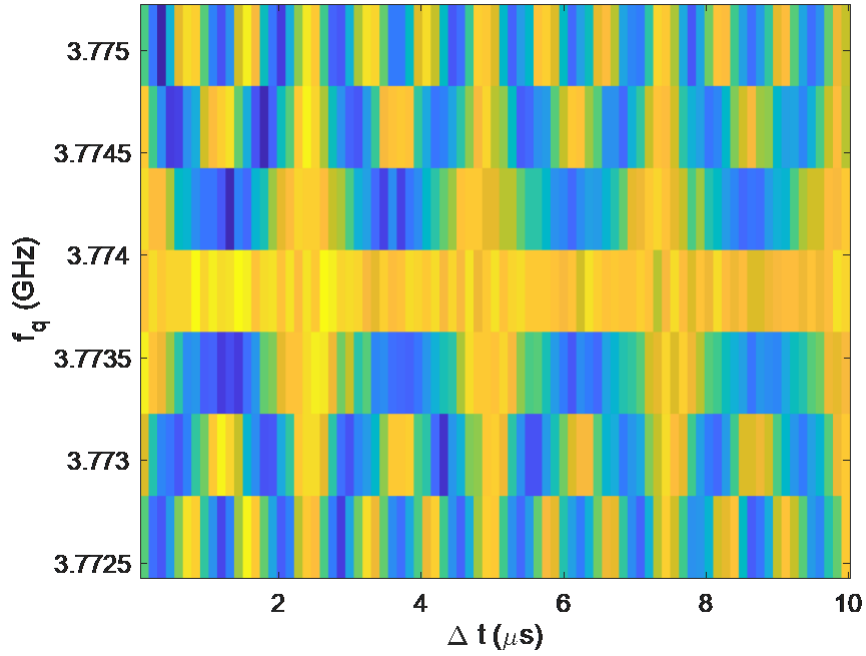


Figure 7.13: Ramsey fringe measurement results of Q_{R1} . From this plot, the main $|g\rangle$ to $|e\rangle$ qubit transition frequency can be extracted at 3.773820 GHz.

7.8 Summary of Measured Parameters of the Devices

In this chapter, I described the characterization of the cavity SI-2a and the two qubits on chip SKD102 and presented initial measurements of T' , T_1 , T_2 and T_2^* . I presented the sections in the order I usually follow for transmon characterization, but it was necessary to repeat measurements fairly often to ensure the qubit parameters had not drifted too much. A summary of the main cavity and qubit parameters are provided in Table 7.1.

Table 7.1: Summary of the measured parameters of transmons Q_{L1} and Q_{R1} on chip SKD102. ω_{ge} is the $|g\rangle \leftrightarrow |e\rangle$ transition frequency. In this table, Δ_1 is the gap of the pure Al lower layer. Δ_2 is the gap of the oxygen-doped upper layer of the gap-engineered transmon Q_{L1} . Δ_3 is the gap of the pure Al upper layer of the standard transmon Q_{R1} . E_J is the Josephson energy and E_c is the rough estimate for the charging energy. Ω_2 / Ω_1 is the volume ratio of the upper and lower layers of the transmon.

	Gap-engineered transmon Q_{L1}	Standard transmon Q_{R1}
Junction area (nm ²)	200×220	200×200
$\omega_{ge}/2\pi$ (GHz)	2.9297	3.7738
$h\omega_{ge}$ (μeV)	12	16
E_c/h (MHz)	225.0	198.5
E_J/h (GHz)	5.55	9.95
Δ_1 (μeV)	200.0	200.0
Δ_2 (μeV)	227.7	---
Δ_3 (μeV)	---	191.1
Ω_2 / Ω_1	2.75	2.32
T' (μs)	50	50
T_1 (μs)	180.9	84.1
T_2 (μs)	66.5	51.9

Chapter 8

Transmons with Gap-Engineered Electrodes:

T_1 Measurements and Other Results

In the previous chapter, I described a gap-engineered transmon that showed a relatively large value for T_1 . The gap difference between the transmon electrode and counter-electrode was intended to induce loss from single quasiparticle tunneling. Motivated by these findings, I constructed Al/AlO_x/Al transmons with a range of gap values and large arrangements to discern their influence on T_1 . In this chapter I mainly discuss three specific designs. The first design was discussed in the previous chapter. It has a base electrode of pure Al and a counter-electrode of oxygen-doped Al. I call this the low gap–high gap device. For the next design, this layout was flipped: The base electrode used oxygen-doped Al, and the counter electrode was of pure Al. I called this a high-gap low-gap design. The third design involved adding an extra layer of pure aluminum to function as a quasiparticle trap.

In this Chapter, I describe T_1 vs time and T_1 vs temperature results on three chips. I observed large T_1 fluctuations in time in each transmon. From these measurements, I tried to unravel the source of these fluctuations and the identity of the dominant loss mechanism.

8.1 Comparison of Low-Gap High-Gap Transmon and an Undoped Al Transmon

After completing a preliminary characterization of the qubits two qubits Q_{L1} and Q_{R1} on transmon chip SKD102 (see Chapter 7), I used the high-power pulsed cavity readout technique [1] to measure the relaxation time repeatedly over many hours. Each T_1 measurements took about 5 minutes to obtain and required averaging 2000 voltage measurements of V_g , V_e and V_q (see Chapter 5). After each T_1 value was found for one transmon, I immediately measured the T_1 of the other transmon to get repeated interleaved T_1 measurements of Q_{L1} and Q_{R1} .

Figure 8.1(a) shows repeated measurements of the relaxation time T_1 of the gap-engineered transmon Q_{L1} at the 20 mK base temperature of the refrigerator. The measurements spanned 15 hours. Large fluctuations were observed, with T_1 varying between a minimum of about 100 μ s and a maximum of about 310 μ s. Figure 8.1(b) shows the corresponding plot of T_1 versus time for the transmon Q_{R1} which had pure Al layers. Relatively large fluctuations in T_1 were also obvious in this transmon, with T_1 varying between about 50 μ s and 100 μ s. Thus, the gap-engineered device had a T_1 that was typically about two or three times longer than that of the standard transmon. All the measurements are with 5000 averaging, most uncertainties of the T_1 vary between 10% to 20%.

Examination of Fig. 8.1 reveals that the fluctuations of the two transmons were not cross-correlated, even though both transmons were on the same chip and the measurements were interleaved in time. This strongly suggests that the fluctuations are not consistent with a common fluctuating external source that is generating the loss, but rather is consistent with a fluctuating loss that is local to each qubit. Further analysis of the fluctuation data will be discussed in the Chapter 9.

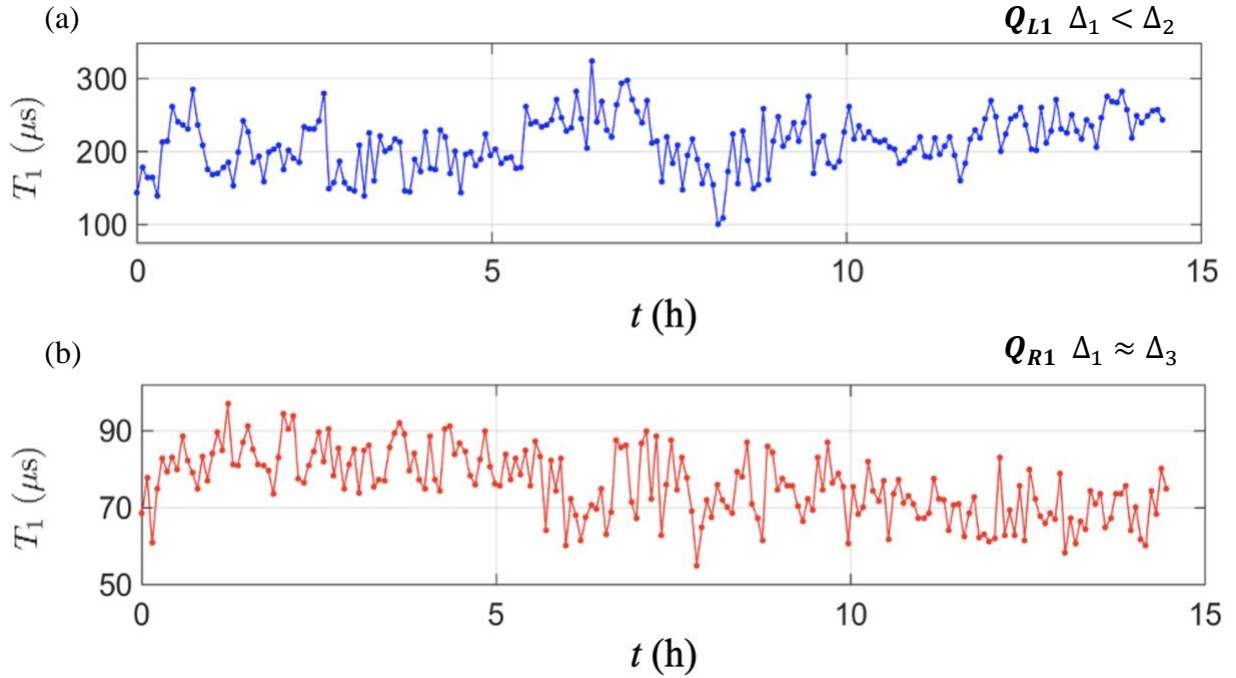


Figure 8.1: (a) The T_1 vs time t measurement for the gap-engineered transmon Q_{L1} on chip SKD102. The maximum T_1 is over $300 \mu\text{s}$. (b) The T_1 vs time t for the standard transmon Q_{R1} on the same chip. The measurements of the two devices were interleaved.

8.2 Temperature Dependence of T_1 for Low-Gap High-Gap Device and Nominal Al Device

I next measured the temperature dependence of T_1 of the transmons Q_{L1} and Q_{R1} . To achieve higher temperatures, power was applied to heater resistors located at the mixing chamber plate. This allowed us to reach temperatures between 20 mK and 250 mK. In order to collect the temperature-dependent data, I swept the temperature up and down slowly for a few cycles over a period of over 2 days. Each measurements took a few mins and required 2000 shots. At temperature over 250 mK, T_1 decreased to below a few μs and the fidelity of the high-power readout was poor.

Figure 8.2(a) shows measurements of T_1 vs temperature T for the gap engineered transmon Q_{L1} . These data were taken while the mixing chamber temperature was slowly swept higher and lower two times. There was a large variation in T_1 after sweeping to high temperature as well as large fluctuations in T_1 in this data set, particularly at low temperatures, with T_1 ranging between about $70 \mu\text{s}$ at the end of the temperature sweeps and $200 \mu\text{s}$ at the start of the sweep. At temperatures above about 150 mK , T_1 decreased rapidly, as expected from loss due to thermally generated quasiparticles.

Figure 8.2(b) shows the corresponding T_1 vs T plot for the standard transmon Q_{R1} . This data was acquired at the same time as that for transmon Q_{L1} . This transmon also showed significant T_1 variations and relatively large fluctuations, with T_1 ranging between about $60 \mu\text{s}$ and $90 \mu\text{s}$ at low temperature, as well as a rapid decrease in T_1 above about 150 mK due to thermal quasiparticles.

Figure 8.2(c) and (d) show the same T_1 vs T data, but on a semi-log plot. Examination of these two plots reveal that the fractional size of the fluctuations in T_1 does not seem to depend on temperature, *i.e.* the size of the fluctuations in T_1 appears to be proportional to T_1 . In particular, this means that the fluctuations in T_1 persist with the same relative size into the region where loss is dominated by thermal quasiparticles. This was quite unexpected and reveals much about the sources of the fluctuations and the origin of the loss in these devices, as I will discuss in Chapter 9.

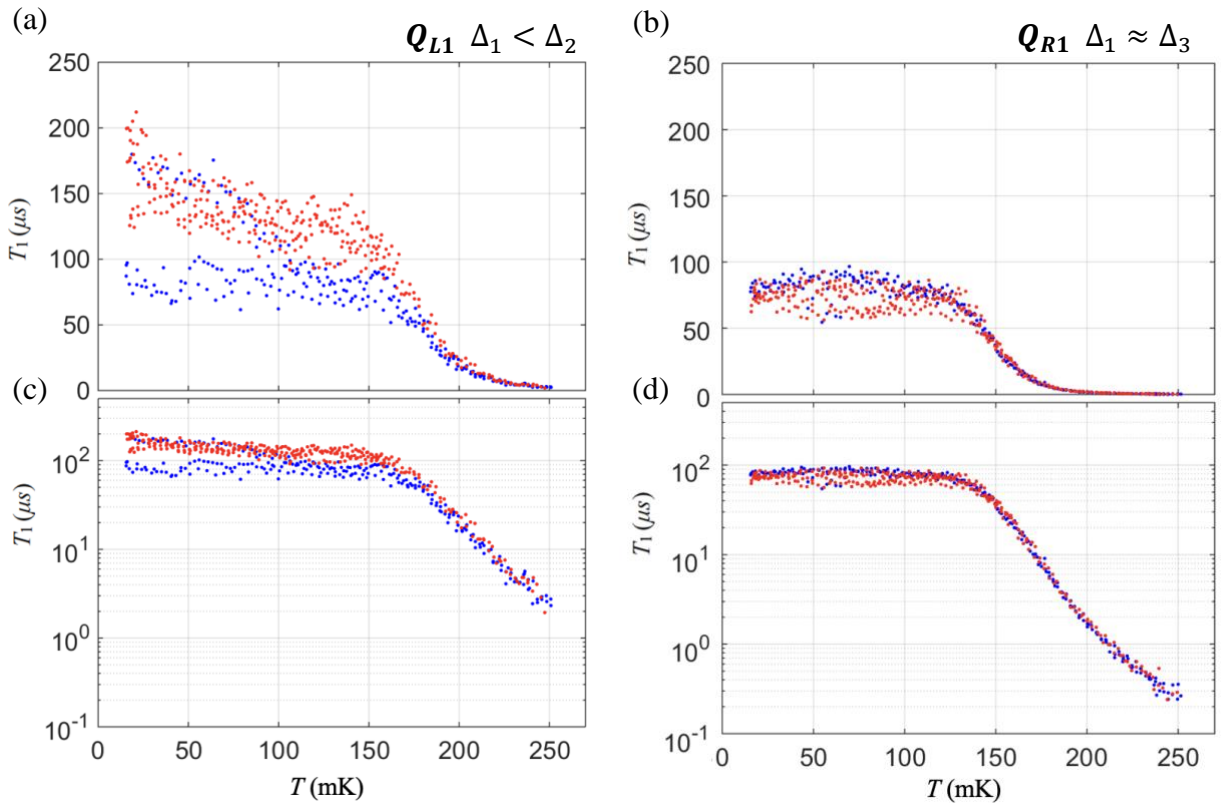


Figure 8.2: (a) Relaxation time T_1 vs temperature T of the gap engineered transmon Q_{L1} on chip SKD 102. T_1 was measured while slowly ramping the mixing chamber temperature, with different cycles indicated by red and blue points. Each point took around 5 minutes. (b) T_1 vs temperature T of the standard transmon Q_{R1} on chip SKD 102. (c) Corresponding semi-log plot of T_1 vs temperature T for transmon Q_{L1} and (d) Q_{R1} .

I discussed a quasiparticle model in Sec. 4.2 and Sec. 4.3. This model can be fit to the data in Fig. 8.3, and one sees reasonable qualitative agreement. The different fitting curves correspond to different non-equilibrium quasiparticle densities, which were used to fit the upper, middle and lower bounds of the data. At higher temperature region this reveals that the curves converge to one curve, where the loss is dominated by thermally generated quasiparticles and only depends on the

temperature. The fits give $\Delta_1 = 225.3 \mu\text{eV}$ and $\Delta_2 = 230.90 \mu\text{eV}$ for Q_{L1} and $\Delta_1 = 190.5 \mu\text{eV}$ and $\Delta_3 = 179.6 \mu\text{eV}$ for Q_{R1} . These differ from values $\Delta_1 = 200 \mu\text{eV}$, $\Delta_2 = 228 \mu\text{eV}$ and $\Delta_3 = 191 \mu\text{eV}$ that we found from direct measurements of the thin films but pretty close.

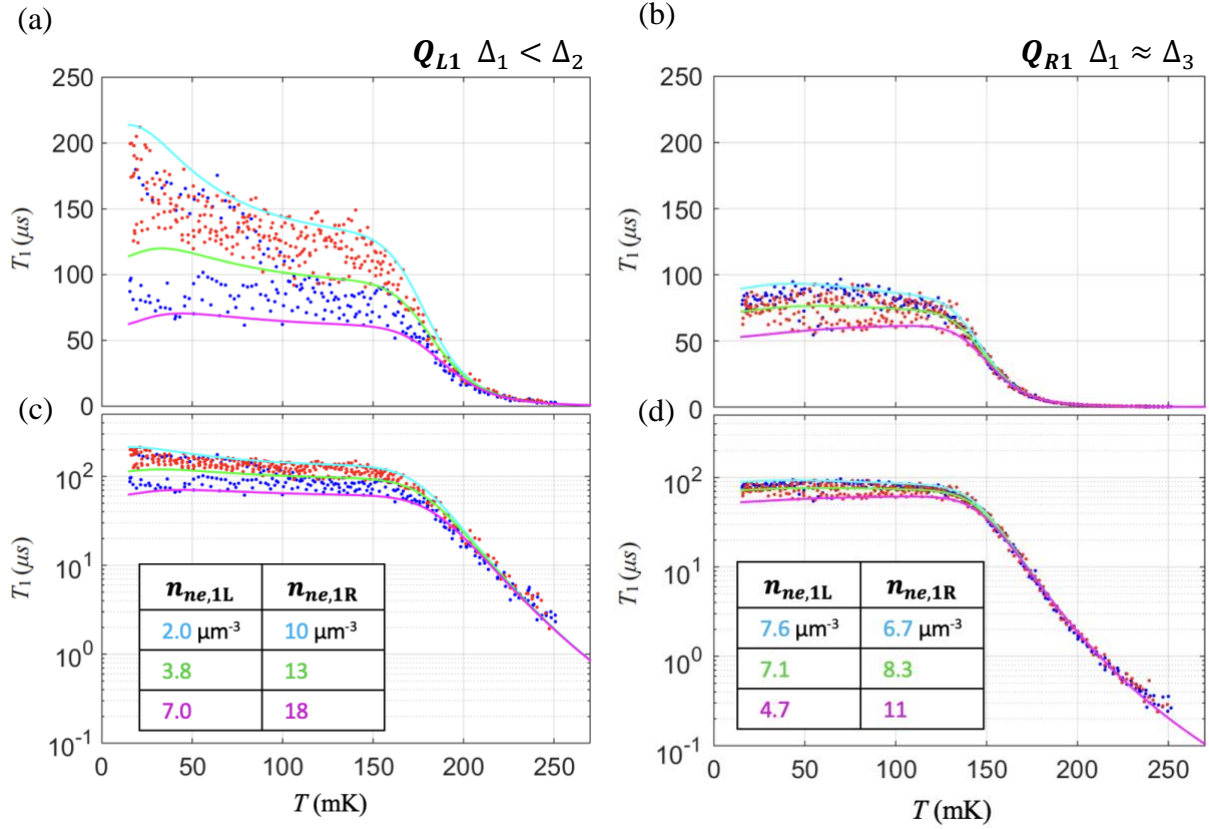


Figure 8.3: (a) Plot of T_1 vs T for (a) gap-engineered transmon Q_{L1} with fitting parameters $\Delta_1 = 225.3 \mu\text{eV}$ and $\Delta_2 = 230.90 \mu\text{eV}$ and (b) standard transmon Q_{R1} with fitting parameters $\Delta_1 = 190.5 \mu\text{eV}$ and $\Delta_3 = 179.6 \mu\text{eV}$. Red and blue points show measurements for different temperature sweeps and the cyan, green, and magenta curves are fits to a two-gap model of loss from quasiparticles with different non-equilibrium quasiparticle densities (see inset table). (c) and (d) are the semi-log plot of (a) and (b).

8.3 Fabrication and Measurements of High-Gap Low-Gap Transmons

As I discussed in Sec. 4.2, the relaxation rate of a transmon due to quasiparticles is directly related to the density of quasiparticles in the base electrode and counter electrode. The main idea of gap-engineering a transmon is that when $|\Delta_1 - \Delta_2| \gg k_B T$, the quasiparticles in the high-gap side will accumulate in the low-gap side, and if $|\Delta_1 - \Delta_2| > \hbar\omega_{ge}$, they will not be able to absorb energy from the transmon by tunneling to high gap side.

The quasiparticle model of loss that I presented in Chapter 4 also suggests that having a low-gap electrode with a larger volume will make it a more effective quasiparticle trap. Since the counter electrode is thicker than the base electrode, this suggests making the counter electrode have the lower gap. We call this arrangement a high-gap low-gap transmon.

To test this idea for improving the T_1 , I fabricated chip KL103. The overall chip layout is the same as that for the chip SKD102 (see Sec.5.1) [2]. In KL103 the base electrode was oxygen doped and the counter electrode is pure Al. Figure 8.4 illustrates the fabrication procedure. In contrast with the fabrication procedure for SKD102, I did not use a mask to cover half of the chip and the transmons have nominally identical layers. I called the left and right transmons Q_{L2} and Q_{R2} . Both transmons have nominally the same oxygen-doped base electrode with gap Δ_1 and pure Al counter electrode with gap Δ_2 . Unfortunately, I didn't co-deposit single films to directly measure the gaps, but the gap values were estimated from our test deposition results and the O₂ doping pressure test discussed in Chapter 5. The base electrode with doping has the gap Δ_1 around 257 μeV . The pure Al counter electrode has the gap Δ_2 around 200 μeV . In this case, both transmons Q_{L2} and Q_{R2} have gap differences greater than the $\hbar\omega_{ge}$. Electrical characterization revealed that the right transmon Q_{R2} had higher transition frequency at 2.8790 GHz, compared to 2.6100 GHz for the left transmon Q_{L2} .

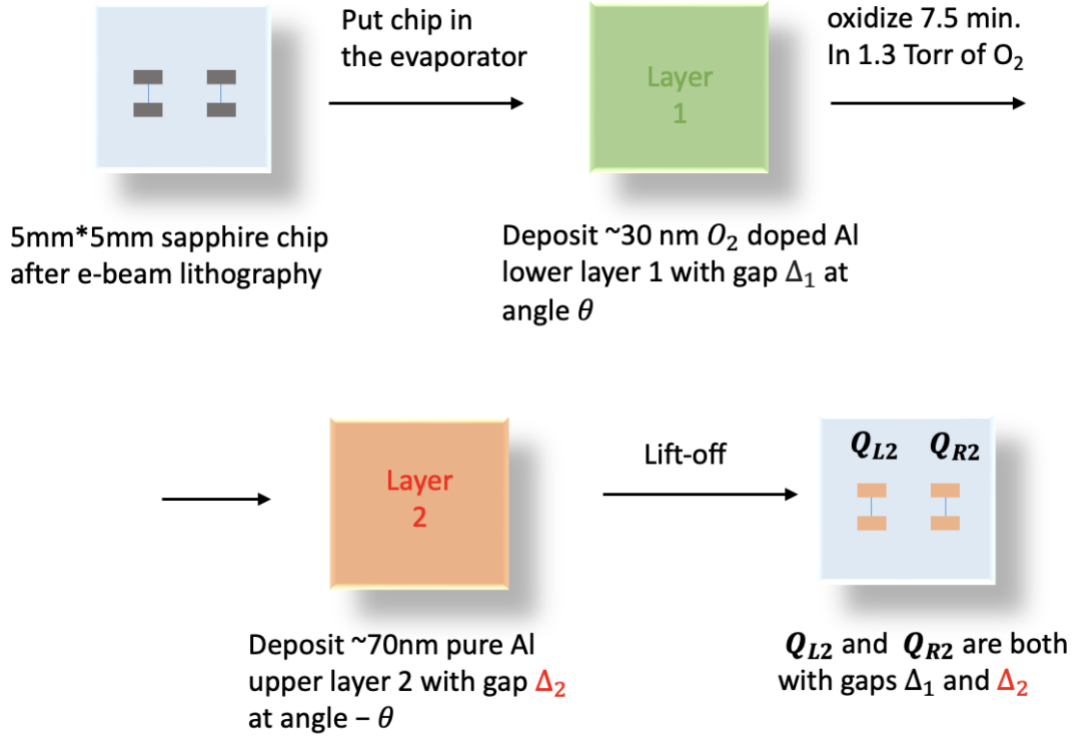
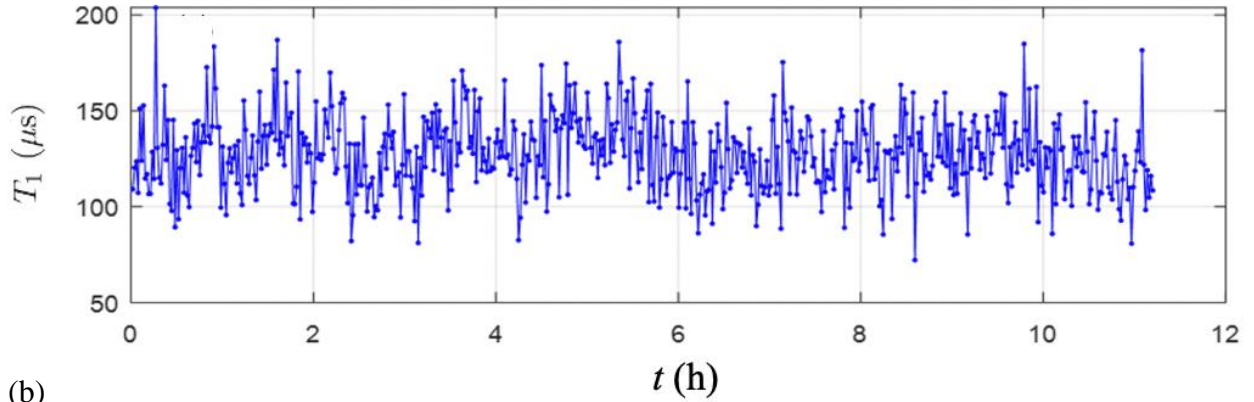


Figure 8.4: Fabrication procedure for building two transmons on chip KL103 in the same pump down. Both gap-engineered transmons have an electrode with gaps Δ_1 and a counter-electrode with gaps Δ_2 .

I performed interleaved measurements of T_1 versus t for these two devices for over 10 hours. Figure 8.5(a) shows T_1 vs t for transmon Q_{L2} and Fig. 8.5(b) shows T_1 versus t for transmon Q_{R2} . The transmons have similar T_1 and both show relatively large fluctuations between 80 μ s to 200 μ s. The left transmon Q_{L2} has a slightly longer average value T_1 . The maximums of T_1 for both devices appear to be over 200 μ s. However, I note that this was not larger than the T_1 of Q_{L1} , even though the gap difference was larger for Q_{L2} and Q_{R2} and the volume of the lower gap electrode was larger for Q_{L2} and Q_{R2} .

(a)



(b)

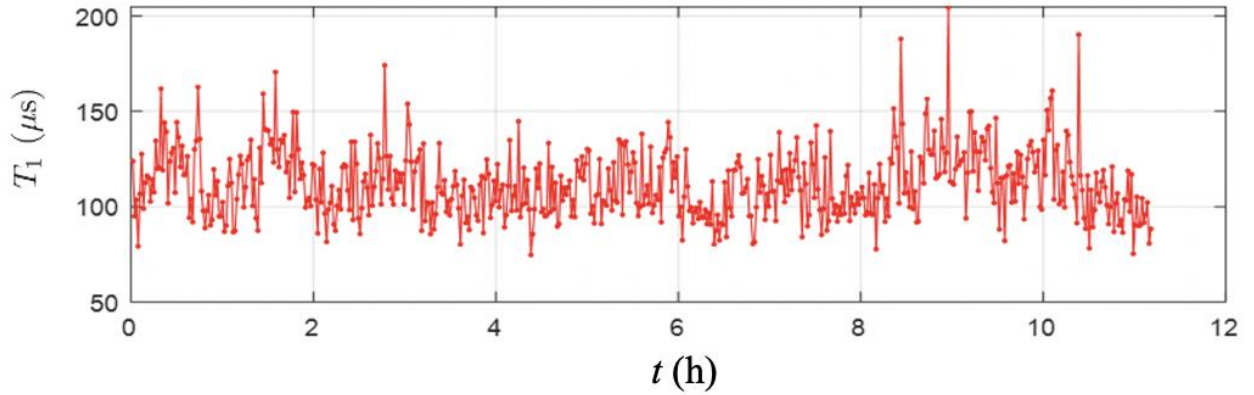


Figure 8.5: (a) T_1 vs time t data for the gap-engineered transmon Q_{L2} . (b) T_1 vs time t data for the gap-engineered transmon Q_{R2} .

8.4 Fabrication and Measurements of Transmons with Trapping Layer

It was quite remarkable that the transmons on chip KL103 didn't have longer relaxation times than transmon Q_{L1} . A possible explanation was that the quasiparticles were getting stuck in the granular Al, which would leave quasiparticles in the high gap side, which could tunnel through the junction and reduce T_1 . To examine this idea, I tried adding a low-gap trapping layer on top of the electrode and counter-electrode to trap the quasiparticles from both layers.

Figure 8.6 shows the fabrication procedure I used to build the transmons. The overall layout of chip KL109 was somewhat different from that of SKD102 and KL103. Both transmons on chip KL109 had an oxygen-doped base electrode with gap Δ_1 , a less-oxygen doped counter electrode with gap Δ_2 and a pure Al trapping layer with the lowest gap Δ_3 . I didn't have co-deposited single films to measure the gaps, but I estimated gap values of each layer from the oxygen-doping tests, which I discussed in Chapter 5. The base electrode with doping has the gap Δ_1 around 265 μeV . The less oxygen-doped counter electrode has the gap Δ_2 around 220 μeV . The pure Al capping layer has the gap Δ_3 around 200 μeV .

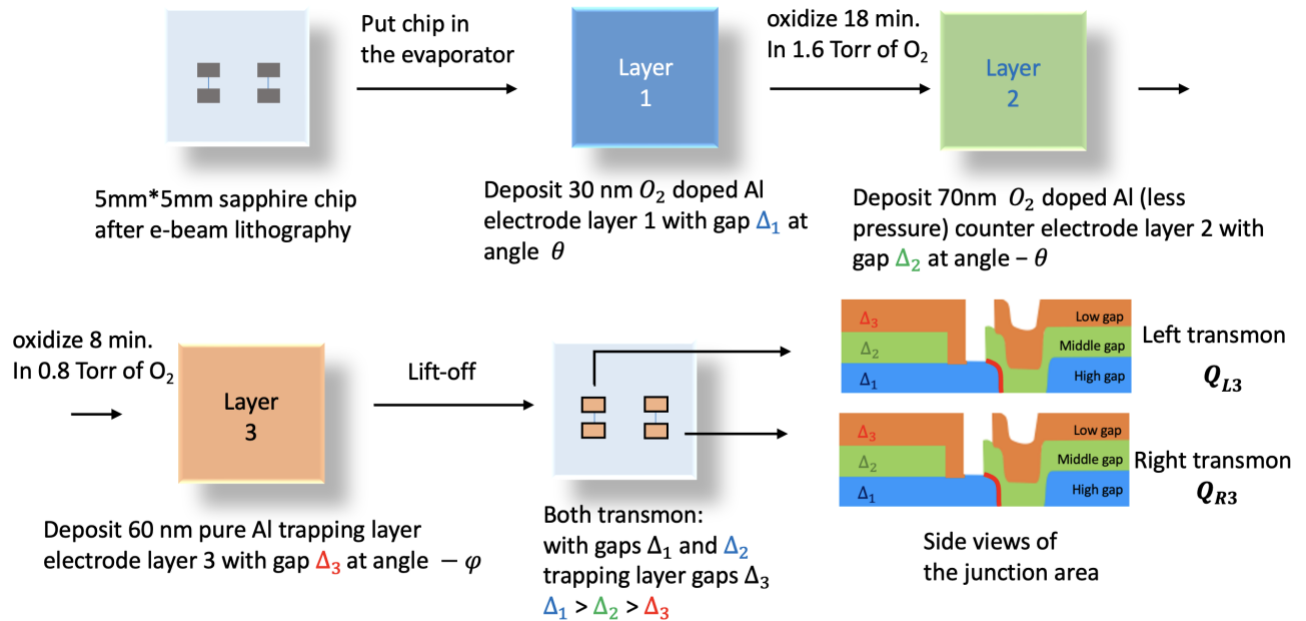
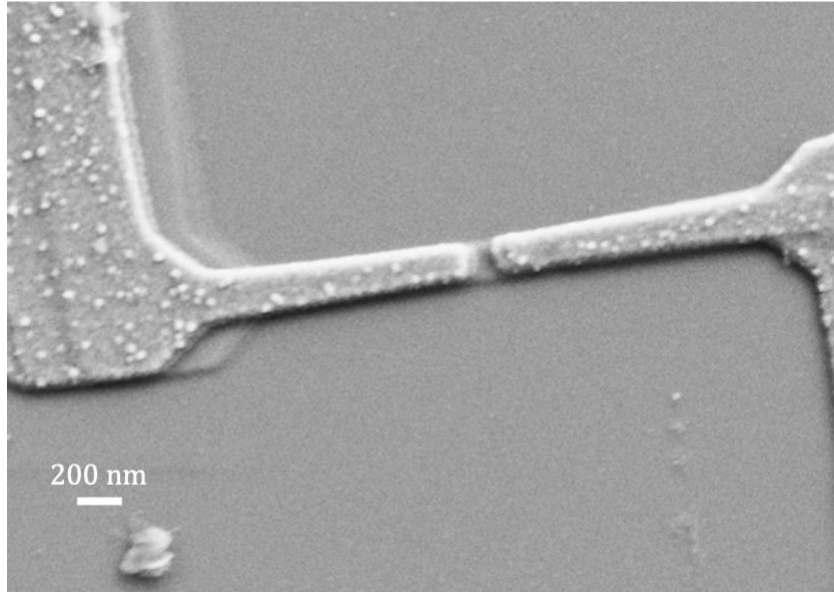


Figure 8.6: Fabrication procedure for building Q_{L3} and Q_{R3} on chip KL109. Both transmons have a triple-layer structure with gaps Δ_1 , Δ_2 and Δ_3 .

(a)



(b)

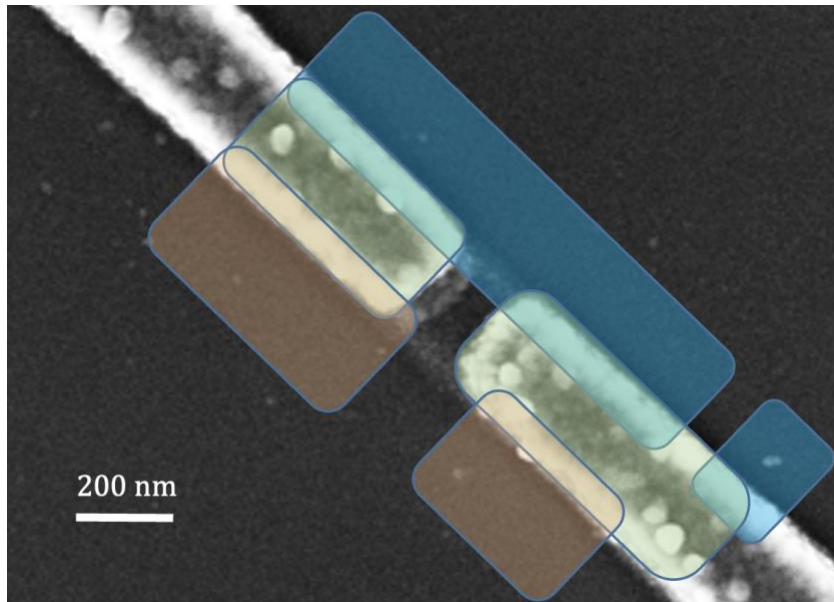


Figure 8.7: SEM image of (a) Q_{L3} junction area with triple layer structure on chip KL109. (b) Detailed view of junction area with colored layers (shifted from original location for better illustration of electrode layout): layer 1 (blue), layer 2 (green), and layer 3 (orange).

The left and right transmons on this chip were called Q_{L3} and Q_{R3} and they were deposited at the same time. When depositing the third trapping layer, I applied a slightly different angle compared to the counter electrode so it would only touch the base electrode of the left side but not the counter electrode of the right side. This guaranteed that the Josephson junction was still between the first two layers (base electrode and counter electrode). Figure 8.7 shows SEM images of one of the junctions.

The right transmon Q_{R3} had a higher transition frequency which is 2.9720 GHz. The transition frequency of the left transmon Q_{L3} was 2.1540 GHz. This was somewhat lower than the 3 GHz I was aiming for, but acceptable.

Figure 8.8 shows repeated measurements of the relaxation time T_1 of Q_{L3} and Q_{R3} at 20 mK. The measurements spanned about 12 hours and large fluctuations in T_1 were again evident. Q_{R3} tended to have a longer T_1 , which fluctuated between about 80 μ s and 120 μ s. Q_{L3} had T_1 that fluctuated between about 40 μ s and 80 μ s. The T_1 values of both devices were shorter than my other gap-engineered devices Q_{L1} , Q_{L2} and Q_{R2} .

If I compare the T_1 results for my gap engineered transmons, the device with highest gap difference gave the shortest T_1 . This was the opposite of what I expected, which means something is missing from our understanding of the device behavior. As I mentioned in the beginning of this chapter, one possible explanation could be quasiparticles get stuck in the granular Al layers so that T_1 gets worse with increased granularity. Although the third layer in devices Q_{L3} and Q_{R3} were meant to fix this problem, it did not. This may have been due to poor contact of the third layer or the fact that I used Δ_1 and Δ_2 that were even larger, producing even more granular films. If this is correct the trapping layer may not help. Another group has published results from very granular Al resonators which suggest pretty long quasiparticle trapping times in their resonators [3]. In their

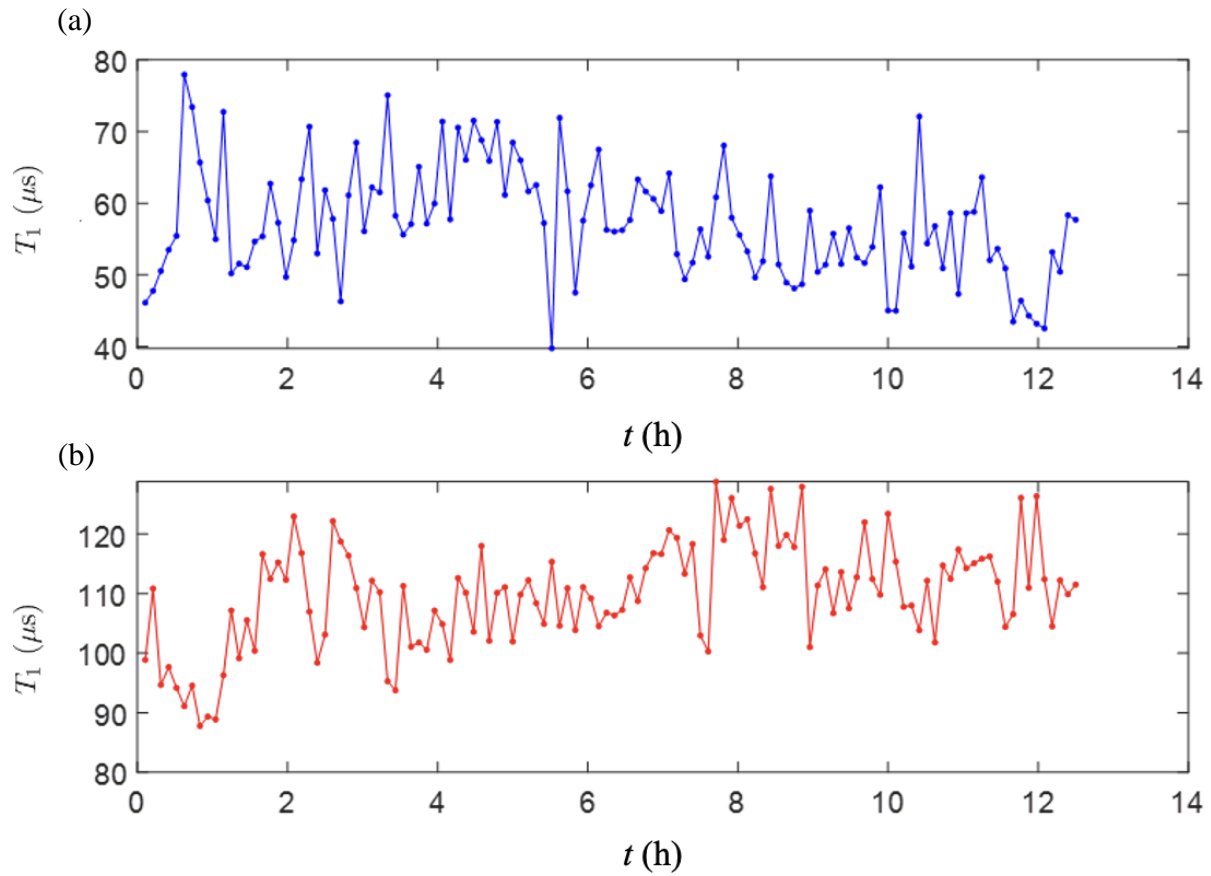


Figure 8.8(a) T_1 vs time t measurements for the gap-engineered transmon Q_{L3} , which had a trapping layer. (b) The T_1 vs time t measurements for the gap-engineered transmon Q_{R3} , which had a trapping layer.

superconducting microwave resonator, some sudden events occur (maybe due to cosmic rays) that cause a large increase in quasiparticle density. If a resonator is made of pure Al, these quasiparticles would quickly recombine (ms), and the resonator frequency would relax back to a relatively small steady state value. By contrast, very granular Al seems to recover slowly which may be due to local inhomogeneity in the gap or the presence of tunnel barriers between the grains. Whatever the source of quasiparticles, once they get stuck in a granular layer, they have a

hard time finding each other and recombining or getting out to the low-gap side. In that case, there will not be good interlayer transfer and the quasiparticles will not empty out of the high-gap side. This could leave quasiparticles to tunnel across the Josephson junction and it doesn't matter that the low-to-high gap quasiparticle tunneling is suppressed.

Another possible issue is that the model only assumed single quasiparticle tunnelling in present. If MAR is significant, then even quasiparticles trapped in the low-gap side will contribute to loss (see Sec. 4.4).

8.5 Charge Dispersion and T_1

I also performed charge dispersion measurements on Q_{R3} and tried to determine if T_1 depended on the offset charge. The offset charge changes with time and leads to frequency variations in a qubit such as Q_{R3} that shows charge dispersion. This could then lead to T_1 fluctuations if T_1 has a frequency dependence. Was this the cause of the T_1 fluctuations I was observing? To try to answer this question, we prepared the qubit state using a long low power excitation at the 2-photon frequency for the $|g\rangle - |f\rangle$ transition. Since the $|g\rangle - |f\rangle$ transition varied, this is not a conventional state excitation for direct state lifetime measurement. We then wait a delay time Δt which was varied and measure the state occupancy. From these measurements we could extract the lifetime of the $|f\rangle$ and $|e\rangle$ states as a function of the 2-photon excitation frequency.

I took spectroscopy on Q_{R3} over a day. I used a long and low power qubit pulse to avoid power broadening and measured the state using the high-power Jaynes Cummings readout [1]. Figure 8.9(a) shows spectroscopic measurements of the $|g\rangle - |e\rangle$ transition. The charge dispersion is around 0.12 MHz. Figure 8.8(b) shows the $|g\rangle - |f\rangle$ two-photon transition. The total charge dispersion for $|g\rangle - |f\rangle$ transition was around 1 MHz. Note this is a two-photon transition, this will correspond to

twice as much dispersion (2MHz) in the single photon $|e\rangle - |f\rangle$ transition. These charge dispersions are consistent with $E_c/h = 180$ MHz and the qubit Hamiltonian. Note that the $|g\rangle - |f\rangle$ transition charge dispersion is much larger than the dispersion of the $|g\rangle - |e\rangle$. With this broader charge dispersion, it is easier to identify the frequency dependence of the state lifetimes two-photon which I show next.

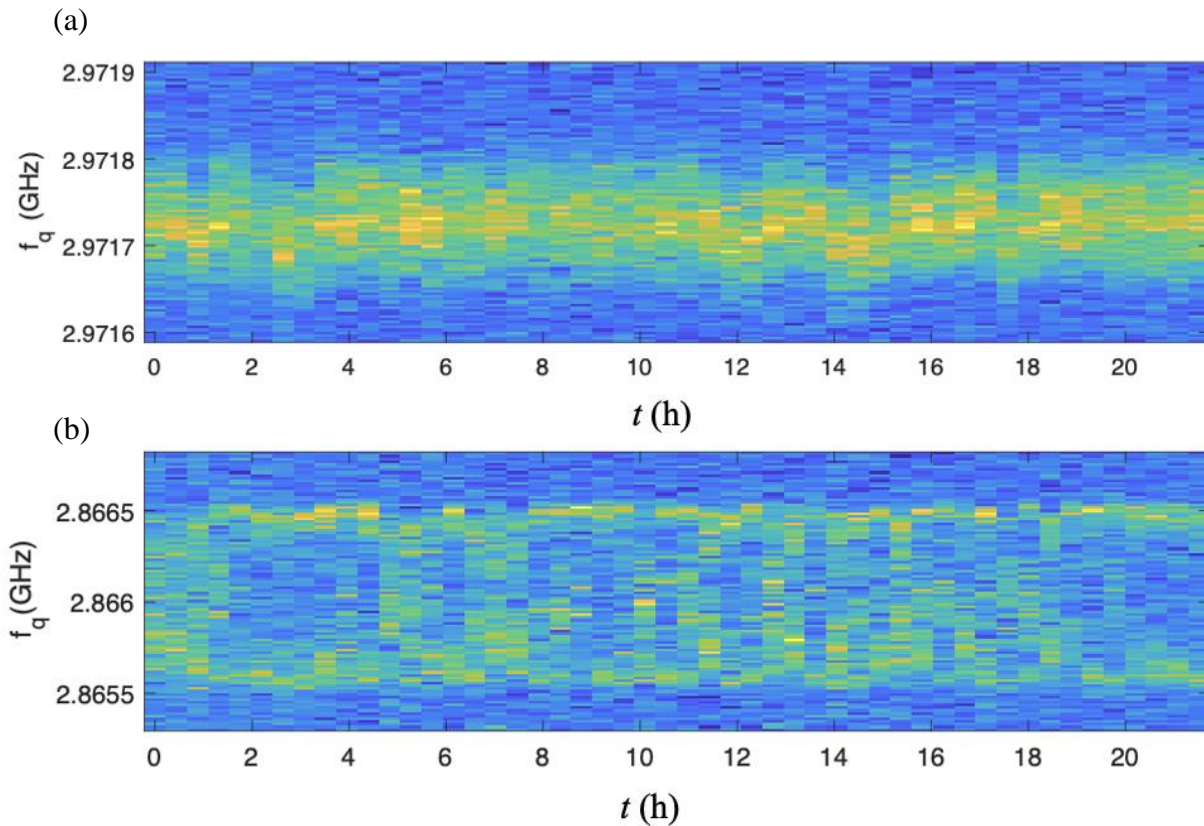


Figure 8.9: Repeated measurement of charge dispersion spectrum in transmon Q_{R3} . (a) $|g\rangle - |e\rangle$ transition versus time t and (b) charge dispersion spectrum for $|g\rangle - |f\rangle$ two photon transition.

I then performed delayed spectroscopy on the two-photon $|g\rangle - |f\rangle$ transition for Q_{R3} . I first measured the transition at 21 frequencies, which covered the dispersion range. I then measured the delayed spectrum for the 2-photon $|f\rangle - |g\rangle$ transition. This contains information on the $|f\rangle - |e\rangle$ decay and the subsequent $|e\rangle - |g\rangle$ decay. Figure 8.10 shows a general process of getting the state lifetime from the delay spectrum measurement. For the measurement in Fig. 8.9, the delay spectrum was measured at 21 frequencies and for a range of Δt values. I fit the signals from different time delay Δt to extract T_1 at each frequency in the 2-photon frequency range.

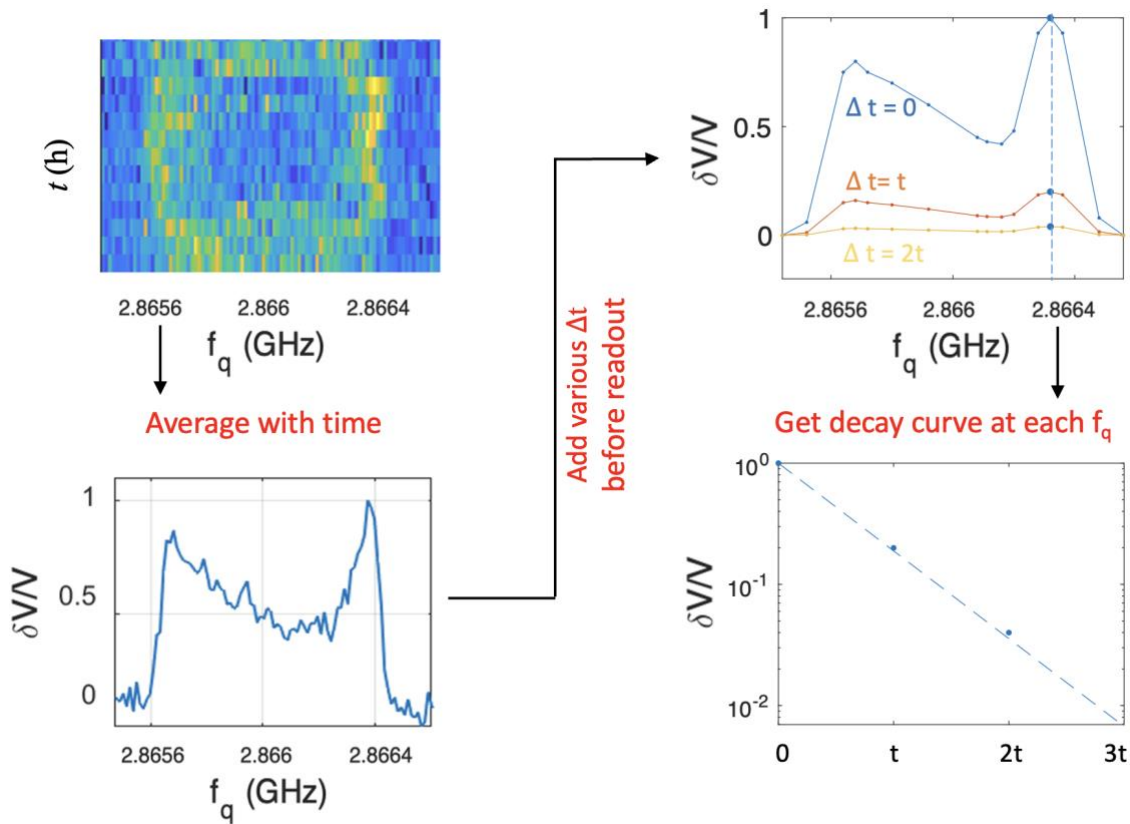


Figure 8.10: The general process of getting state lifetime from delay spectrum. First, the repeated charge dispersion spectrum is averaged at each f_q . Then I measure the spectrum with adding various Δt before the cavity readout and get averaged spectrum for each Δt . Finally, fit the amplitude from averaged spectrum with different Δt to a decay curve and get state lifetime at each f_q .

I note that in order to measure the delay spectrum, I needed to use a different cavity power to measure the state. At low readout power, we are only sensitive to the $|f\rangle$ state. In principle, this let me find the $|f\rangle$ state qubit lifetime as a function of $|g\rangle - |f\rangle$ transition frequencies. I then used the high-power readout at higher power where it was sensitive to both $|e\rangle$ and $|f\rangle$ states. From this second set I could extract the $|e\rangle$ state lifetime as a function of $|g\rangle - |f\rangle$ transition frequencies.

Figure 8.11 shows results from the delayed spectroscopy measurements. Figure 8.11(a) shows $|f\rangle$ state lifetime measurements (low readout power) with time delay from 0 μs to 50 μs . Figure 8.11(b) shows the $|e\rangle$ state lifetime measurements (high readout power) with time delay from 0 μs to 150 μs . The signals at each frequency decay with increasing time delay Δt . Note that in Fig. 8.11(b), the output is sensitive to both the $|e\rangle$ and the $|f\rangle$ state, but by longer time delay to 150 μs , most of the signals would be from the $|e\rangle$ state. Comparing the two plots, I note that the shapes are different which suggests a variation in T_1 with the 2-photon $|g\rangle - |f\rangle$ transition frequency.

Figure 8.12 shows the resulting lifetime of $|e\rangle$ and $|f\rangle$ states from the delayed spectroscopic measurement in Fig. 8.8. The red curve is the $|e\rangle$ state lifetime and the blue curve is the $|f\rangle$ state lifetime. $|e\rangle$ state lifetimes vary between 85 to 115 μs , which is similar to the direct T_1 measurement in Fig. 8.8 (b). The $|f\rangle$ state lifetime varied between 25 to 65 μs . This was short compared to $|e\rangle$ state lifetime as expected, but the strong dependence on offset charge was unexpected.

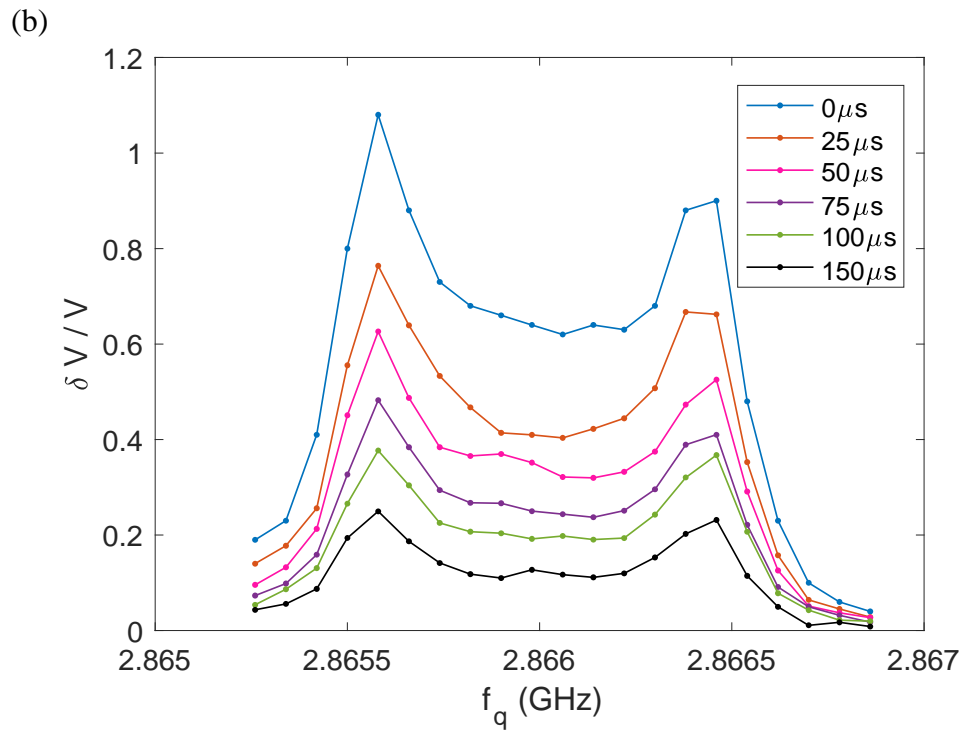
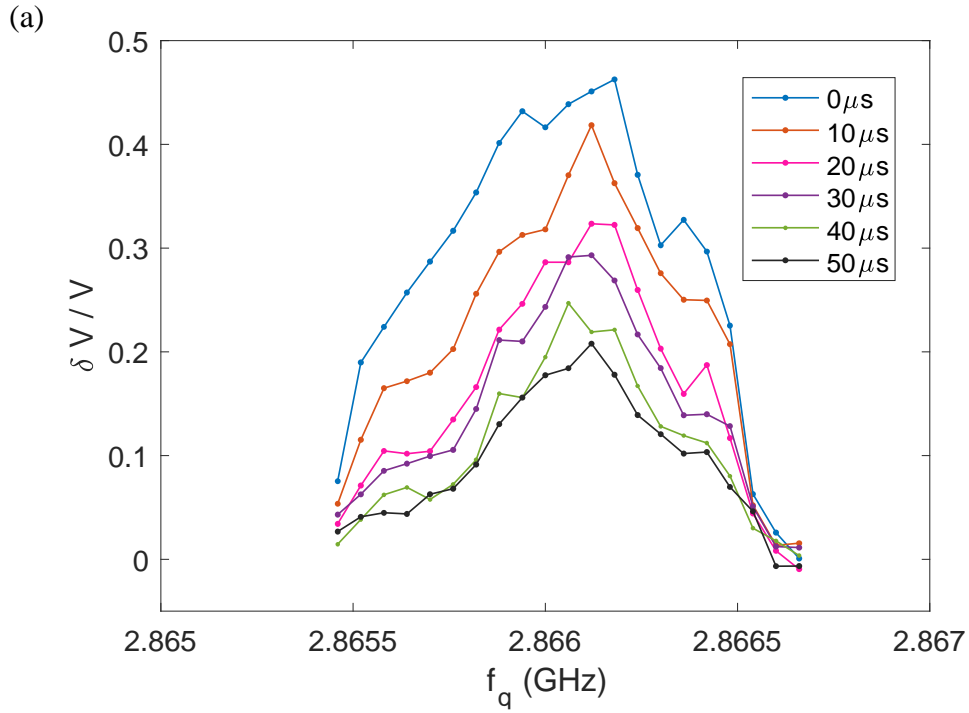


Figure 8.11: Delayed spectroscopy measurement of transmon Q_{R3} versus the 2-photon transition frequency: (a) signal from $|f\rangle - |e\rangle$ transition for delay $\Delta t = 0 - 50 \mu s$ and (b) $|e\rangle - |g\rangle$ transition with $\Delta t = 0 - 150 \mu s$.

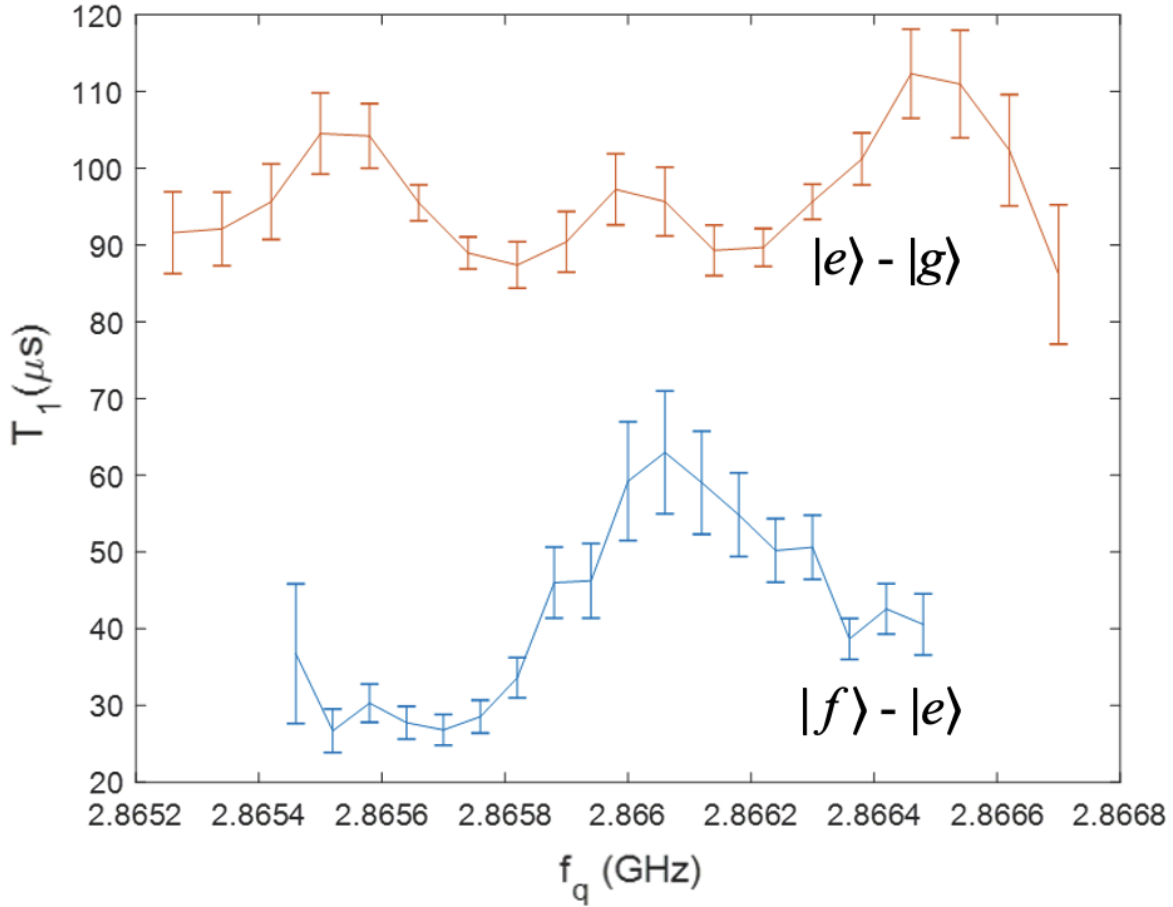


Figure 8.12: State lifetime measurement of $|f\rangle$ state and $|e\rangle$ state over the $|g\rangle - |f\rangle$ dispersive frequencies.

8.6 Summary of All the Gap-Engineered Devices and Conclusion

Table 8.1 summarizes the main parameters of all the gap-engineered transmons I made and measured (E_c/h of some devices are estimated from anharmonicity). I used five different approaches to fabricate these devices. All the chips have a design that is similar to that of SKD102, with two transmons (left and right) on one sapphire chip. Chip KL04 had two transmons, but only one was measurable. *Process 1* was used for the fabrication of chip SKD102 and is described in detail in Chapter 7. Both transmons have a pure Al base electrode, but the left transmon counter

electrode doped with oxygen and the right transmon has a counter electrode made of pure Al. I used *Process 2* to create two identical transmons with a pure Al base electrode and an oxygen-doped counter electrode. *Process 3* adds a pure 10 nm thick Al trapping layer on top of *Process 2*. *Process 4* can be thought of as the inverse of *Process 2*, with an oxygen-doped base electrode and a pure Al counter electrode. I used this for chip KL103. *Process 5* had an oxygen-doped base electrode, a counter electrode with less oxygen, and a pure Al trapping layer. I used this for chip KL109.

All devices were measured in the same Oxford refrigerator at a base temperature of 20 mK, with the chip in a 3D Al cavity. The transmons had transition frequencies between 2.15 GHz and 5.20 GHz and T_1 varied between 4.7 and 310 μ s. Figure 8.13 reveals that the maximum T_1 values increased as the transmon frequency decreased. The red line in Fig. 8.13 shows the phenomenal fit of function

$$T_1 = \frac{17ms*GHz^4}{f^4}. \quad (8.1)$$

I note that most of the transmons with $T_1 > 100 \mu$ s have transition frequencies below 3 GHz. This is much less than the cavity frequency of 6.2 GHz, which reduces the contribution of the Purcell effect. I also note that T_1 due to TLS and quasiparticles should both increase as frequency decreases, but not this rapidly. More work is needed to verify this behavior and understand its cause.

In conclusion, this chapter I mainly discuss the T_1 measurement of gap-engineered transmons. The maximum T_1 at base temperature (20 mK) was over 300 μ s. I also measured temperature dependence of T_1 from 20 mK to 250 mK (Q_{L1} and Q_{R1}). I then fit these data with non-equilibrium quasiparticle model which gives $\Delta_1 = 225.3 \mu$ eV and $\Delta_2 = 230.90 \mu$ eV for Q_{L1} and $\Delta_1 = 190.5 \mu$ eV and $\Delta_3 = 179.6 \mu$ eV for Q_{R1} , compared to measured gaps $\Delta_1 = 200 \mu$ eV, $\Delta_2 =$

228 μeV and $\Delta_3 = 191 \mu\text{eV}$. The transmons Q_{L2} , Q_{R2} , Q_{L3} and Q_{R3} with larger gaps and different electrode configurations didn't produce longer T_1 than Q_{L1} , which may be due to the granular films trapping the quasiparticles. I also discuss the lifetime measurement of Q_{R3} from delay spectrum to figure out the impact of charge dispersion on T_1 .

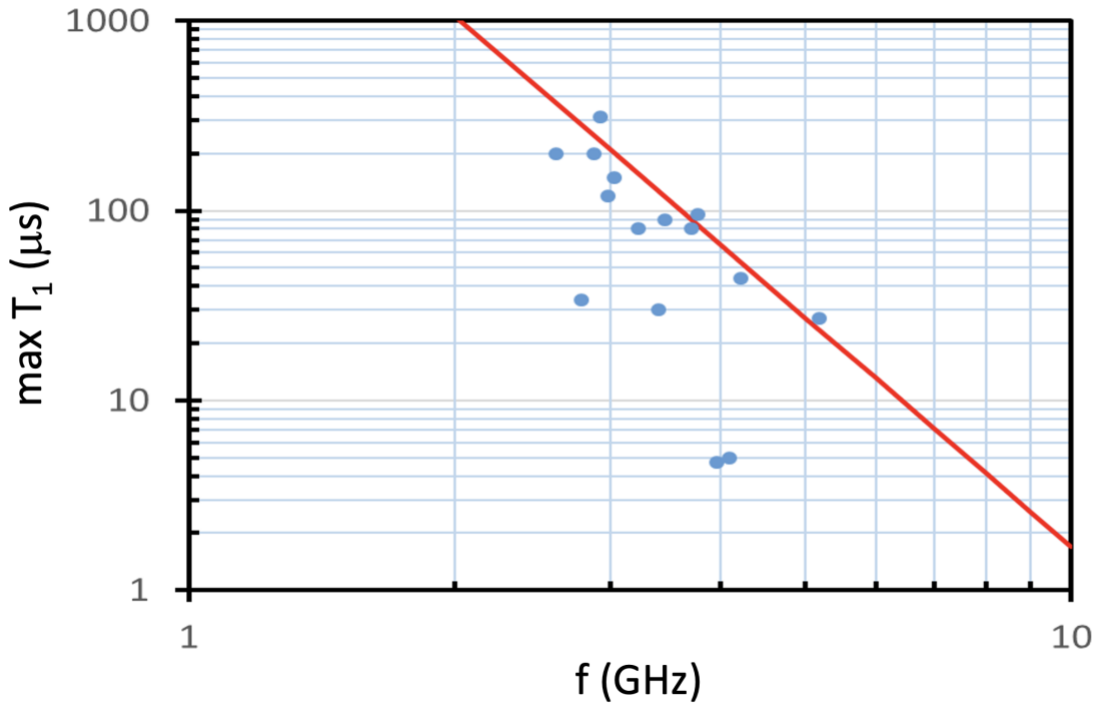


Figure 8.13: The maximum T_1 vs transmon frequency of the devices in Table 8.1. The red line is a fitting line with the power relation of T_1 proportional to f^{-4} .

Table 8.1: Parameters of the transmons

	SKD102	SKD102	KL91	KL91	KL95	KL95	KL03	KL03	KL03	KL04
Process	1	1	2	2	2	2	3	3	3	3
f_{ge} (GHz)	2.9297	3.7738	3.965	4.099	4.2254	3.2299	3.466	3.708	5.181	
hf_{ge} (μ eV)	12	16	16.8	17.4	17.9	13.9	14.7	15.7	21.4	
E_J/h (GHz)	5.5493	9.9504	11.147	11.329	12.07	7.20	7.910	9.720	20.34	
E_C/h (MHz)	224.05	198.19	193.96	204.33	204.11	206.05	214	196	178	
E_J/E_C	24.8	50.2	57.8	55.4	59.1	35.0	37.0	49.6	114.6	
Δ_1 (μ eV)	200.0	200.0	\sim 200.0	\sim 200.0	\sim 200.0	\sim 200.0	199.0	199.0	198.6	
Δ_2 (μ eV)	227.7	191.1	\sim 235.0	\sim 235.0	\sim 219.3	\sim 219.3	257	257	243.3	
$\Delta_1 - \Delta_2$ (μ eV)	27.7	-8.9	35.0	35.0	19.3	19.3	58.0	58.0	44.7	
Ω_2/Ω_1	2.75	2.32	\sim 2.33	\sim 2.33	\sim 2.33	\sim 2.33	\sim 2.33	\sim 2.33	\sim 2.33	
Max T_1 (μ s)	310	95	4.7	5	44	80	90	80	27	

Table 8.1 (continued): Parameters of the transmons

	KL02	KL02	KL103	KL103	KL102	KL102	KL109	KL109
Process	3		4		4		5	
f_{ge} (GHz)	3.400	2.784	2.6100	2.8790	3.0356	2.9806	2.1528	2.9718
hf_{ge} (μ eV)	14.4	11.8	11.1	12.2	12.9	12.6	9.2	12.6
E_J/h (GHz)	7.506	5.188	4.2901	5.588	5.8709	6.0013	2.70	5.93
E_C/h (MHz)	218	217	236.0	214.0	226.58	212.35	272	214
E_J/E_C	34.4	23.9	18.2	26.1	26.0	28.3	9.93	27.21
Δ_1 (μ eV)	201.0	201.0	~ 252.6	~ 252.6	~ 252.6	~ 252.6	~ 265.0	~ 265.0
Δ_2 (μ eV)	241	241	~ 200	~ 200	~ 200	~ 200	~ 220	~ 220
$\Delta_1 - \Delta_2$ (μ eV)	40.0	40.0	-52.6	-52.6	-52.6	-52.6	-45.0	-45.0
Ω_2/Ω_1	~ 2.33	~ 2.33	~ 2.33	~ 2.33	~ 2.33	~ 2.33	~ 2.33	~ 2.33
Max T_1 (μ s)	30	34	200	200	150	120	80	120

Chapter 9

Analysis of Relaxation Time Fluctuations

In all my transmons, T_1 fluctuated on the time scale of minutes, with a standard deviation larger than 30% of the average. In this chapter, I provide analysis of the fluctuations that reveals how they depend on time, on T_1 itself, and on the temperature. This analysis shows that for the different devices at base temperature, this fluctuation magnitude roughly scales as $T_1^{3/2}$. On the other hand, if I consider how the fluctuations in each device varies with temperature, the fluctuation magnitude appears to be proportional to T_1 . I show that this behavior is inconsistent with being caused by a fluctuating source of non-equilibrium quasiparticles, fluctuations in the two-level system dielectric loss, Poisson fluctuations in the number of quasiparticles and fluctuations in quasiparticle trapping due to changes in the number of vortices. I then propose a model in which the dissipation is due to quasiparticles and the fluctuations are produced by changes in the number of quasiparticle dissipation channels. This model appears to be consistent with the observed $T_1^{3/2}$ scaling of the fluctuations in different devices at base temperature and the linear scaling in T_1 if the temperature is swept in individual devices, including when the temperature is over 150 mK, where the loss is dominated by thermally generated quasiparticles.

9.1 T_1 Fluctuation Data

Figure 9.1(a) shows the same T_1 vs temperature T data as Fig. 8.2 for transmons Q_{L1} and Q_{R1} , but in this figure on one semi-log plot. Using this data, we determined the standard deviation of T_1 as a function of temperature by sorting the results for each device into narrow temperature bins, and then taking the standard deviation of the T_1 values in each bin.

Figure 9.1 (b) shows the resulting plot of σ_{T_1} vs T_1 for both devices. Note that in this plot, the points on the right (larger T_1 values) are at lower temperature, while the points on the left (smaller T_1 values) are at higher temperatures, where thermal quasiparticles dominate. Both devices show that σ_{T_1} is linearly proportional to T_1 , even at higher temperature. Thus the *relative* fluctuation size σ_{T_1}/T_1 appears to be constant, independent of the temperature.

The fact that σ_{T_1}/T_1 does not vary from low to high temperature suggests that a single fluctuating mechanism (the numerator) is responsible over the full range and furthermore that the same loss mechanism (the denominator) dominates over the entire range. Since we know the loss at high temperature is dominated by quasiparticle loss, this suggests that this is also the dominant loss mechanism at low temperatures. We examine this behavior further below to understand whether this qualitative observation can be verified quantitatively.

Our group and our collaborators at LPS have over the last few years acquired additional somewhat less detailed data on fluctuations in several other transmons. Some devices were measured before and after cycling to room temperature and our collaborators used a different dilution refrigerator and measurement system. Figure 9.2 shows a summary plot of σ_{T_1} vs T_1 for several of these transmons at base temperature. The large range of average T_1 may be the result of the roughly inverse relationship between qubit frequency and T_1 that we have observed, gap

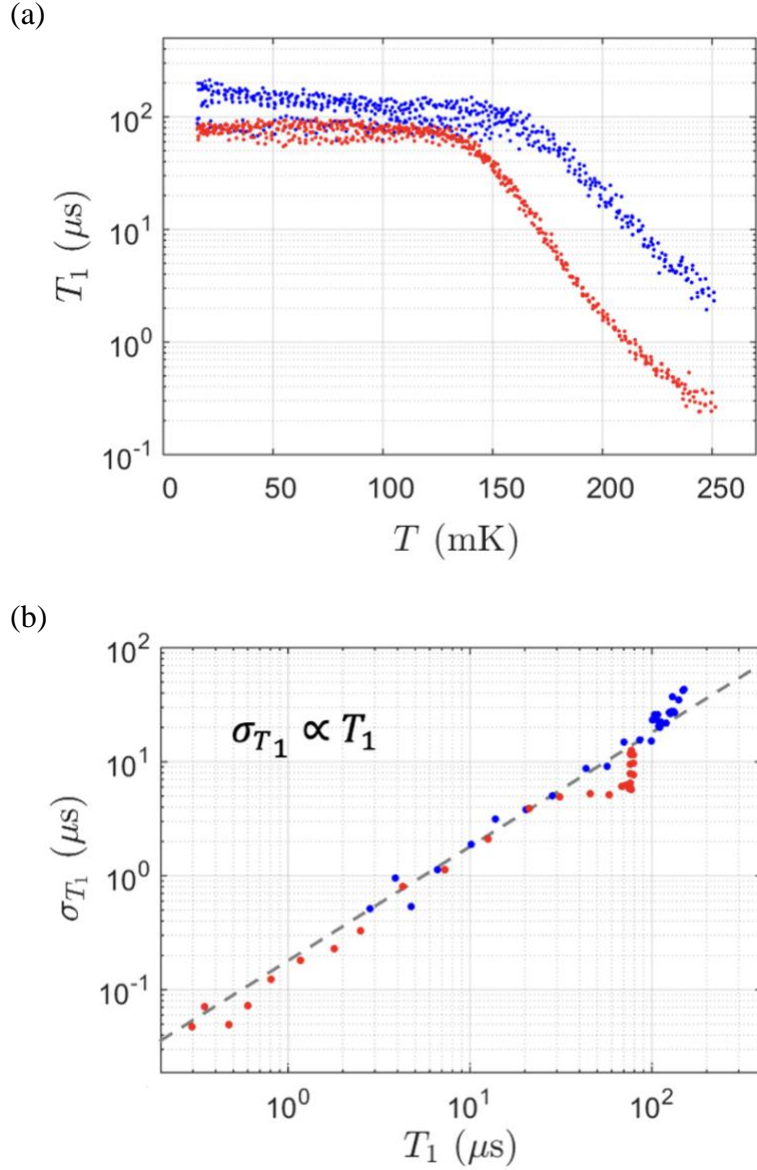


Figure 9.1: (a) Semi-log plot of relaxation time T_1 vs temperature T with results for gap-engineered transmon Q_{L1} (blue) and standard transmon Q_{R1} (red). (b) Semi-log plot of σ_{T_1} vs T_1 for gap-engineered transmon Q_{L1} (blue) and standard transmon Q_{R1} (red). For this plot, the T_1 data in (a) was divided into the temperature bins and the standard deviation was then calculated for each bin. Note that temperature decreases from left (shorter times T_1) to right (longer times T_1). Dashed line shows σ_{T_1} scales linearly with T_1 .

engineering, as well as other random variations in the devices. The straight line fit on this log-log plot shows σ_{T_1} is proportional to $T_1^{1.43}$, which is close to $T_1^{3/2}$. Needless to say, this is surprising not only because these are many different devices and the T_1 -axis covers about 2 and a half decades, but also because the exponent is not 1, which was the exponent seen when plotting σ_{T_1} vs T_1 for each single transmon when its temperature was swept. A group from Fermi Lab also found similar power law relations of σ_{T_1} is proportional to $T_1^{1.5}$ [1].

I note that the point for Q_2^* is an outlier. When we first measured this device, the mixing chamber shield was not coated with SiC. Thus, this device was measured under different and much noisier conditions from the others. Because of this, it showed a significant excess excited state population at base temperature and short T_1 . Our group measured the same chip two additional times after the can was coated with SiC and the corresponding points fall in line with the other measurements.

At first sight, it is hard to see what could account for these exponents being different, but in the next section I present a simple model that yields a possible explanation of this behavior.

9.2 Model for Fluctuations in Quasiparticle Dissipation Channels

In order to understand the unusual behavior of the fluctuations in T_1 described above, I consider a simple model of in which the relaxation rate of a transmon scales with the product of the number N_q of quasiparticles in one electrode of the device's junction and the number N_c of quasiparticle dissipation channels that are active in the junction. We can think of a dissipation channel as a relatively high-transparency atomic-scale region in the tunnel junction barrier through which only quasiparticles can tunnel and cause loss. Variations in the transparency of the channels, due to random charge noise for example, could cause variations in the channel conductance,

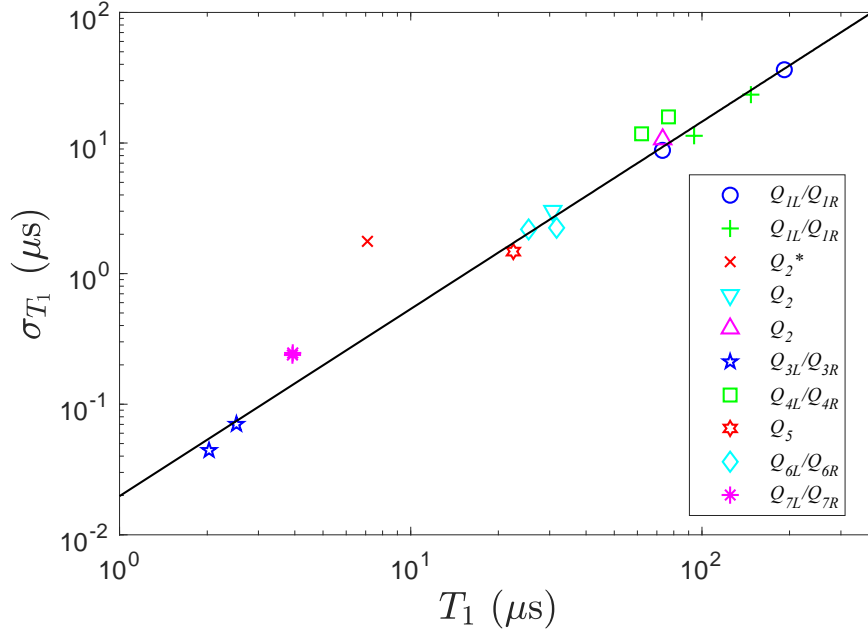


Figure 9.2: Plot of σ_{T_1} vs T_1 for different transmons at the base temperature of 20 mK. The transmons have different resonant frequencies, from 2.7 GHz to 5.2 GHz, and different layer configurations (see Table 8.1). The straight line is a power law fit showing $\sigma_{T_1} \propto T_1^{1.43}$. Q_{1R} , Q_{1L} , and Q_2 were measured more than one time on different runs of the refrigerator and with different cavities.

impacting the loss. It is important to note that we typically do not see corresponding large fluctuations in the transmon's transition frequency. This means that the fluctuating channels do not affect the tunneling of pairs and must only impact the quasiparticle tunneling. This is somewhat unusual or unexpected and why we refer to them as quasiparticle dissipation channels. Kim *et al.* [2] have reported simulations of electron tunneling through Al/AIO_x/Al junctions and they seem

to show channels. This suggests that channels are inherent to Al/AlO_x/Al junctions, at least as I fabricated them.

In this situation, the relaxation rate of the transmon can be written as

$$\frac{1}{T_1} = \frac{N_c N_q}{A} + \frac{1}{T_\gamma}, \quad (9.1)$$

where $1/T_\gamma$ is the relaxation rate due to all other processes (Purcell effect, direct coupling to the input/output lines, two level systems, etc.) and the factor A may in general depend on other system parameters such as the temperature T , the gaps Δ_1 and Δ_2 of the electrodes, and the volume of the electrodes, as well as the device's capacitance C and the junction's tunneling resistance R_n . The relaxation time T_1 will then obey

$$T_1 = \frac{A}{N_c N_q + \frac{A}{T_\gamma}}. \quad (9.2)$$

I now assume that the number of dissipation channels N_c undergoes slow fluctuations (over times much longer than it takes us to measure T_1) with a Poisson distribution, so that the standard deviation of N_c obeys

$$\sigma_{N_c} = \sqrt{N_c}. \quad (9.3)$$

Here N_c should be taken as the average number of channels.

From Eqs. (9.2) and (9.3), the resulting fluctuations in T_1 will have a standard deviation given by

$$\sigma_{T_1} = \left| \frac{\partial T_1}{\partial N_c} \right| \sigma_{N_c} = \frac{AN_q}{\left(N_c N_q + \frac{A}{T_\gamma}\right)^2} \sqrt{N_c} = \frac{T_1^2 N_q \sqrt{N_c}}{A}. \quad (9.4)$$

In the limit $T_\gamma \gg A/N_c N_q$, i.e. the relaxation rate due to the quasiparticles is much larger than the relaxation due to all other processes, then

$$T_1 \approx \frac{A}{N_c N_q}, \quad (9.5)$$

and the standard deviation in T_1 reduces to

$$\sigma_{T_1} \approx \frac{A}{N_c^2 N_q} \sqrt{N_c} \approx \frac{T_1 \sqrt{N_c}}{N_c} = T_1 \sqrt{N_c} \quad (9.6)$$

In this limit, I can then write

$$\left(\frac{T_1}{\sigma_{T_1}} \right)^2 \approx N_c, \quad (9.7)$$

where N_c should again be taken as the average number of channels. Note that the left side of Eq. (9.7) is just the inverse of the relative size of the fluctuations squared. As we noted, the relative size of the fluctuations in T_1 in our device appears to be temperature independent, and this is consistent with Eq. (9.7) if the number of fluctuating channels N_c does not depend on temperature.

According to Eq. (9.7), the fraction $(T_1/\sigma_{T_1})^2$ gives the average number of fluctuating dissipation channels. If N_c and the fluctuations in N_c are temperature independent, then varying the temperature will just change the number of quasiparticles, which will change T_1 of a device, and the fluctuations would then obey

$$\sigma_{T_1} = \frac{T_1}{\sqrt{N_c}}, \quad (9.8)$$

with N_c being a temperature-independent constant. This gives a linear dependence of σ_{T_1} on T_1 . This is consistent with the Fig. 9.1 (b), which shows σ_{T_1} for a single device as the temperature T is varied. We thus see that the simple model explains why the relative size of the fluctuations is temperature independent and why this persists into the thermal quasiparticle limit.

I note that Eq. (9.8) can also be written in the form

$$\sigma_{T_1} \approx \frac{A}{N_c^2 N_q} \sqrt{N_c} = \frac{A}{N_c^{\frac{3}{2}} N_q} = T_1^{3/2} \sqrt{\frac{N_q}{A}}. \quad (9.9)$$

Consider now a collection of transmons that are all at the same temperature and have the same non-equilibrium quasiparticle number N_q and factor A , but different numbers of dissipation channels N_c and relaxation times T_1 . Clearly this would only be roughly true for the devices included in Fig. 9.2, which were measured in different systems and had a range of parameters. Nevertheless, when measuring different devices, Eq. (9.9) implies that we should expect to see σ_{T_1} scaling with $T_1^{3/2}$, which is similar to the observed scaling. I emphasize that while this does not prove that the model is the correct explanation of the phenomenon, it does demonstrate that the scaling of σ_{T_1} with T_1 seen in Fig. 9.1 (when T_1 is varied by sweeping T in individual devices) is not inconsistent with the scaling of σ_{T_1} with $T_1^{3/2}$, seen in Fig. 9.2 (when T_1 of different devices is measured at the same temperature) [3].

9.3 Ruling Out Other Sources of Fluctuations

Although the above model is quite simple, it is not trivial. We can see this by considering the behavior caused by other potential sources of the fluctuations, which do not reproduce the behavior we observe in the T_1 fluctuations.

First, consider a fluctuating external source of non-equilibrium quasiparticles. Of course, I mentioned above that such a source is not consistent with the uncorrelated fluctuations in T_1 that we saw in two transmons that were on the same chip. To see why, note again in this case I can write the relaxation rate as

$$\frac{1}{T_1} = \frac{N_{qp}}{A} + \frac{1}{T_\gamma}, \quad (9.10)$$

where A is a constant, N_{qp} is the total number of quasiparticles, and $1/T_\gamma$ is the relaxation rate due to all other processes. The relaxation time can then be written as

$$T_1 = \frac{A}{N_{qp} + \frac{A}{T_1}}. \quad (9.11)$$

The total number of quasiparticles will in general include those from thermal generation and the external source. As I discussed in Chapter 4, if I ignore recombination and assume quasiparticles are lost by trapping, then we can write

$$N_{qp} = N_{neqp} + N_{eq}, \quad (9.12)$$

where N_{eq} is the number of thermally generated quasiparticles in one electrode of the transmon and N_{neqp} is the number of quasiparticles that were generated by the external source. If N_{neqp} undergoes fluctuations with standard deviation σ_{neqp} , the resulting fluctuations in T_1 are

$$\sigma_{T_1} = \left| \frac{\partial T_1}{\partial n_{neqp}} \right| \sigma_{neqp} = \frac{A}{\left(N_{qp} + \frac{A}{T_1}\right)^2} \sigma_{neqp} = \frac{T_1^2}{A} \sigma_{neqp}. \quad (9.13)$$

For different devices run in the same system at the same temperature, we might expect similar factors A and σ_{neqp} , and we would then see scaling of σ_{T_1} as T_1^2 for different devices at all temperatures. This is not consistent with the observed dependence seen in Fig. 9.2. Note also, if we measure T_1 versus T in a single device, Eq. (9.13) implies that we should expect to see scaling of σ_{T_1} as T_1^2 , which is not observed. Eq. (9.13) also implies that if we sweep the temperature of a device and measure $(T_1/\sigma_{T_1})^2$, we should see that it scales inversely with T_1^2 . This is not observed.

In the Chapter 8, Figure 8.3 shows results from fitting the maximum T_1 vs T curve, the minimum T_1 vs T curve and the middle T_1 vs T curve using a detailed model for loss due to quasiparticles in a transmon with electrodes with different gaps. This model was described in Sec.4.2 and Sec. 4.3. The model includes non-equilibrium generation of quasiparticles as well as thermal generation. However, examination of the higher temperature region reveals that the curves converge to one curve; at high temperatures the loss is dominated by thermally generated

quasiparticles and only depends on the temperature. Thus at temperatures where thermal quasiparticles dominate the loss, fluctuations in the number of non-equilibrium quasiparticles is relatively un-important, and this contradicts the observed behavior. We note that this same argument can be used to rule out fluctuations in the number of quasiparticles due to fluctuations in the quasiparticle trapping rate.

Next consider what happens if there are fluctuations in the dielectric loss due to fluctuating two-level systems. I can again write the total relaxation rate as

$$\frac{1}{T_1} = \frac{N_c N_q}{A} + \frac{1}{T_\gamma}, \quad (9.14)$$

but this time I will suppose that $1/T_\gamma$ is a fluctuating relaxation rate due to TLS dielectric loss. I then find

$$\sigma_{T_1} = \left| \frac{\partial T_1}{\partial T_\gamma} \right| \sigma_{T_\gamma} = \frac{A^2}{\left(N_c N_q + \frac{A}{T_\gamma} \right)^2} \frac{\sigma_{T_\gamma}}{T_\gamma^2} = \frac{T_1^2}{T_\gamma^2} \sigma_{T_\gamma}. \quad (9.15)$$

If T_γ and σ_{T_γ} are temperature-independent, at least in the temperature range of interest, then Eq. (9.15) implies that we would expect to see σ_{T_1} scaling as T_1^2 when we sweep the temperature of a device. This is not what is observed. Equation (9.15) also implies that:

$$\left(\frac{T_1}{\sigma_{T_1}} \right)^2 = \frac{T_\gamma^4}{\sigma_{T_\gamma}^2 T_1^2} \quad (9.16)$$

Since T_1 varies with temperature due to thermal quasiparticles, this implies that the right hand side will *not* be independent of temperature, and that instead the relative size of the fluctuations will decrease with increasing temperature. This is quite plausible behavior, but it is not observed in our devices.

9.4 Conclusion

In conclusion, we measured large temporal fluctuations in the relaxation time T_1 of Al/AlO_x/Al transmons. While we have not identified their origin, weak correlations between qubits on the same chip suggest a local source. Characterizing the dependence of the fluctuation magnitude σ_{T_1} on T_1 puts further constraints on the nature of the source. In an individual device, T_1 can be shortened by increasing the temperature and generating thermal quasiparticles. In this case, we saw $\sigma_{T_1} \propto T_1$ up to 250 mK, where the total loss is sure to be dominated by quasiparticles. Alternatively, different devices studied at 20 mK showed a wide range of T_1 , due to differences in the intrinsic device properties or measurement environment. In this case, we found $\sigma_{T_1} \propto T_1^{1.43}$. Neither of these results seemed to depend on gap engineering of the electrodes. We presented a simple model that showed this behavior is consistent with a fluctuating number of quasiparticle “dissipation channels,” and inconsistent with a fluctuating external source of quasiparticles or two-level systems. Further work will be needed to find and eliminate the significant loss fluctuations in these devices.

Chapter 10

Conclusions

To conclude, I fabricated Al/AlO_x/Al transmons with gap-engineering, mounted the devices in a 3D cavity and measured their relaxation time T_1 . The best gap-engineered device had a maximum T_1 that exceeded 300 μ s. I also measured T_1 repeatedly and obtained T_1 fluctuation data at different temperatures. Based on the observed behaviors, I postulated that the T_1 fluctuations were due to fluctuations in the number of quasiparticle dissipation channels.

In Chapter 4, I discussed the impact of non-equilibrium quasiparticles on transmon relaxation. I introduced a model for quasiparticle-induced loss in transmons and how this loss would vary with temperature. Notably, this model can predict a significant T_1 rise as T is reduced if the two electrodes of a transmon have different gaps and the difference of the gaps is larger than hf_{ge} . In this case, tunneling of single quasiparticle from the low-gap side to the high-gap side can be suppressed. Other conditions for seeing this effect are that there must be: i) a mechanism generating non-equilibrium quasiparticles, ii) a relatively low quasiparticle trapping rate to allow sufficient quasiparticle accumulation in the low gap region at low temperatures, and iii) an absence of other loss mechanisms producing substantially larger loss. I also discussed how multiple Andreev reflection (MAR) effects can significantly modify these conditions and reduce T_1 .

Chapter 5 is dedicated to the design and fabrication of the transmon chip SKD102 . This chip had two transmons with thin-film electrodes of pure Al and counter-electrodes made with either pure Al or oxygen-doped Al. The superconducting energy gap of each layer was set by the oxygen during that layer deposition, and the layer's thickness. In Chapter 6, I describe the

experimental apparatus and procedures that I used to measure the transmons, including how I found T_1 , T' , T_2 and T_2^* .

In Chapter 7 I discussed the basic characterization of the two transmons on device SKD102. Such characterization of a qubit is essential before one can perform qubit manipulation or gate operations. Device parameters such as the qubit transition frequency and coherence time, tend to drift with time and shift slightly between cooldowns. In the first cooldown, I found that the gap-engineered transman had a much longer T_1 than the non-gap-engineering transmon, even though they were on the same chip.

In Chapter 8, I described my measurements of T_1 as a function of time and temperature for the two transmons on chip SKD102. At 20 mK, the gap-engineered device on this chip showed T_1 variations between about 100 μs and 300 μs , while the un-doped device on the same chip showed T_1 variations between about 50 and 100 μs . The fluctuations in T_1 in the two devices were uncorrelated. These were remarkably large T_1 fluctuations. I also discussed and compared the T_1 measurements from chips KL103 and KL109, which had different transmon electrode configurations. All the devices had long T_1 , but not as long as expected given the gap differences. It is possible that this discrepancy was due to quasiparticles getting stuck in the granular Al layers, which might cause T_1 to get worse with increased granularity, as I observed. Further work should focus on lower electrode gap, so the film is less granular and better understanding of MAR.

Chapter 9 focused on the T_1 fluctuations and a model to explain the fluctuation behavior. For the different devices made by our group and our collaborators, this fluctuation magnitude appears to roughly scale as a power law of T_1 with an exponent near 1.5. With increasing temperature, T_1 decreases due to a higher density of thermally generated quasiparticles. For each individual device measured up to 250 mK, the fluctuation magnitude appears to be proportional to

T_1 . I presented a model of quasiparticle dissipation channels that reproduces both observed scaling relationships. Finally, I noted that the scaling power laws of T_1 are not consistent with fluctuations in two-level-system dielectric loss or fluctuations in the density of non-equilibrium quasiparticles.

Bibliography

Chapter 1

- [1] P. Benioff, "The computer as a physical system: A microscopic quantum mechanical Hamiltonian model of computers as represented by Turing machines", *J. of Stat. Phys.*, **22** 5(1980).
- [2] R. Landauer, "Irreversibility and heat generation in the computing process", *IBM journal of research and development*, **5**, 3 (1961).
- [3] Y. Manin, "Computable and non-computable", *Sovetskoye Radio*, **128** (1980).
- [4] R. P. Feynman, "La nature de la physique", *Le Seuil* (1980).
- [5] K. Igeta, and Y. Yamamoto, "Quantum mechanical computers with single atom and photon fields. International Quantum Electronics Conference", *Optical Society of America* (1988).
- [6] D. Deutsch and R. Jozsa, "Rapid solution of problems by quantum computation", *Proceedings of the Royal Society of London. Series A: Mathematical and Physical Sciences*, **439**, 1907 (1992).
- [7] P. W. Shor, "November. Algorithms for quantum computation: discrete logarithms and factoring", 35th annual symposium on foundations of computer science (1994).
- [8] C. Monroe, D. M. Meekhof, B. E. King, W. M. Itano, and D. J. Wineland, "Demonstration of a Fundamental Quantum Logic Gate," *Phys. Rev. Lett.* **75**, 4714 (1995).
- [9] J. I. Cirac and P. Zoller, "Preparation of macroscopic superpositions in many-atom systems", *Phys. Rev. A*, **50**, 4 (1994).
- [10] A. Imamoglu, D. D. Awschalom, G. Burkard, D. P. DiVincenzo, D. Loss, M. Sherwin, and A. Small, "Quantum Information Processing Using Quantum Dot Spins and Cavity QED," *Phys. Rev. Lett.* **83**, 4204 (1999).

- [11] Y. Nakamura, Y. A. Pashkin, and J. S. Tsai, "Coherent control of macroscopic quantum states in a single-Cooper-pair box," *Nature* **398**, 786 (1999).
- [12] M. H. Devoret and R. J. Schoelkopf, "Superconducting circuits for quantum information: an outlook", *Science* **339**, 1169 (2013).
- [13] E. Knill, R. Laflamme, and G. J. Milburn, "A scheme for efficient quantum computation with linear optics", *Nature*, **409**, 6816 (2001).
- [14] M. D. Reed, L. DiCarlo, S. E. Nigg, L. Sun, L. Frunzio, S. M. Girvin and R. J. Schoelkopf, "Realization of three-qubit quantum error correction with superconducting circuits", *Nature*, **482**, 7385 (2012).
- [15] T. H. Taminiau, J. Cramer, T. van der Sar, V. V. Dobrovitski, and R. Hanson, "Universal control and error correction in multi-qubit spin registers in diamond", *Nature nanotechnology*, **9**, 3 (2014).
- [16] N. Ofek, A. Petrenko, R. Heeres, P. Reinhold, Z. Leghtas, B. Vlastakis, Y. Liu, L. Frunzio, , S. M. Girvin, L. Jiang and M. Mirrahimi, "Extending the lifetime of a quantum bit with error correction in superconducting circuits", *Nature*, **536** 7617 (2016).
- [17] J. M. Gambetta, J. M. Chow and M. Steffen, "Building logical qubits in a superconducting quantum computing system", *Npj Quan. Info.*, **3** 1 (2017).
- [18] M. Mosca, "Cybersecurity in an Era with Quantum Computers", *IEEE Security Privacy*; **16**, 5 (2018).
- [19] Y. Cao et al., "Quantum Chemistry in the Age of Quantum Computing", *Chem. Rev.*, **119**, 19 (2019).
- [20] M. Buzzi, M. Först, R. Mankowsky, A. Cavalleri, "Probing Dynamics in Quantum Materials with Femtosecond X-rays", *Nat. Rev. Mater.*, **3** (2018).

- [21] R. Hulet, E. Hilfer, D. Kleppner, "Inhibited Spontaneous Emission by a Rydberg Atom", *Phys. Rev. Lett.* **55**, 2137 (1985).
- [22] Z. Kim, B. Suri, V. Zaretsky, S. Novikov, K. D Osborn, A. Mizel, F. C Wellstood, B. S Palmer, "Decoupling a Cooper-Pair Box to Enhance the Lifetime to 0.2 ms", *Phys. Rev. Lett.* **106**, 120501 (2011).
- [23] R. F. Voss and R. A. Webb, "Macroscopic Quantum Tunneling in 1- μm Nb Josephson Junctions," *Phys. Rev. Lett.* **47**, 265 (1981).
- [24] M. H. Devoret, J. M. Martinis, and J. Clarke, "Measurements of Macroscopic Quantum Tunneling out of the Zero-Voltage State of a Current-Biased Josephson Junction," *Phys. Rev. Lett.* **55**, 1908 (1985).
- [25] J. M. Martinis, M. H. Devoret, and J. Clarke, "Energy-Level Quantization in the Zero-Voltage State of a Current-Biased Josephson Junction," *Phys. Rev. Lett.* **55**, 1543 (1985).
- [26] T. A. Fulton, P. L. Gammel, D. J. Bishop, L. N. Dunkleberger, and G. J. Dolan, "Observation of combined Josephson and charging effects in small tunnel junction circuits," *Phys. Rev. Lett.* **63**, 1307 (1989).
- [27] M. Büttiker, "Zero-current persistent potential drop across small-capacitance Josephson junctions," *Phys. Rev. B.*, **36**, 3548 (1987).
- [28] C. D. Tesche, "Can a noninvasive measurement of magnetic flux be performed with superconducting circuits?" *Phys. Rev. Lett.* **64**, 2358 (1990).
- [29] R. Rouse, S. Han, and J. E. Lukens, "Observation of Resonant Tunneling between Macroscopically Distinct Quantum Levels", *Phys. Rev. Lett.* **75**, 1614 (1995).

- [30] J. Koch, M. Y. Terri, J. Gambetta, A. A. Houck, D. I. Schuster, J. Majer, A. Blais, M. H. Devoret, S. M. Girvin and , R. J. Schoelkopf, "Charge-insensitive qubit design derived from the Cooper pair box", *Phys. Rev. A*, **76**, 4 (2007).
- [31] C. Choi, *IBM Unveils 433-Qubit Osprey Chip*, IEEE Spectrum (2022).
(<https://spectrum.ieee.org/ibm-quantum-computer-osprey>).

Chapter 2

- [1] S. Haroche, and J. M. Raimond, *Exploring the quantum: atoms, cavities, and photons*. Oxford university press (2006).
- [2] B. Sarabi, A. N. Ramanayaka, A. L. Burin, F. C. Wellstood and K. D. Osborn, "Projected dipole moments of individual two-level defects extracted using circuit quantum electrodynamics", *Phys. Rev. Lett.*, **116**, 16 (2016).
- [3] J. J. Sakurai and J. Napolitano, *Modern Quantum Mechanics, 2nd ed.*, Pearson Education Inc., (2011).
- [4] B. D. Josephson, "The discovery of tunnelling supercurrents.", *Rev of Mod Phys.*, **46**, 2 (1974).
- [5] B. D. Joesphson, "Possible new effects in superconductive tunneling", *Phys. Lett.*, **1**, 7 (1962).
- [6] M. Tinkham, *Introduction to Superconductivity, 2nd Edition*, McGraw Hill, New York, (1996).
- [7] N. A. Court, A. J. Ferguson, and R. G. Clark, "Energy gap measurement of nanostructured aluminium thin films for single Cooper-pair devices," *Supercond. Sci. Tech.* **21**, 015013 (2008).
- [8] V. Bouchiat, D. Vion, P. Joyez, D. Esteve, and M. H. Devoret, "Quantum coherence with a single Cooper pair," *Physica Scripta 1998*, **165** (1998).
- [9] M. H. Devoret and J. M. Martinis, "Superconducting qubits, in Quantum Entanglement and Information Processing", *Elsevier, New York, NY*, (2003).

- [10] J. M. Martinis, "Superconducting phase qubits," *Quantum Info Process*, **8**, 81-103 (2009).
- [11] E. M. Purcell, H. C. Torrey, and R. V. Pound, "Resonance absorption by nuclear magnetic moments in a solid", *Phys. Rev.*, **69**, 1-2 (1946).
- [12] J. Koch, T. M. Yu, J. Gambetta, A. A. Houck, D. I. Schuster, J. Majer, A. Blais, M. H. Devoret, S. M. Girvin, and R. J. Schoelkopf, "Charge-insensitive qubit design derived from the Cooper pair box", *Phys. Rev. A* **76**, 042319 (2007).
- [13] S. M. Girvin, M. H. Devoret and R. J. Schoelkopf, "Circuit QED and engineering charge-based superconducting qubits", *Physica Scripta*, **137** (2009).
- [14] J. Bardeen, L. N. Cooper, and J. R. Schrieffer, "Theory of superconductivity," *Phys. Rev.* **108**, 1175 (1957).
- [15] J. A. Schreier, A. A. Houck, J. Koch, D. I. Schuster, B. R. Johnson, J. M. Chow, J. M. Gambetta, J. Majer, L. Frunzio, M. H. Devoret, S. M. Girvin, and R. J. Schoelkopf, "Suppressing charge noise decoherence in superconducting charge qubits", *Phys. Rev. B* **77**, 180502 (2008).
- [16] H. Paik, D. I. Schuster, L. S. Bishop, G. Kirchmair, G. Catelani, A. P. Sears, B. R. Johnson, M. J. Reagor, L. Frunzio, L. I. Glazman, S. M. Girvin, M. H. Devoret, and R. J. Schoelkopf, "Observation of high coherence in Josephson junction qubits measured in a three-dimensional circuit QED architecture", *Phys. Rev. Lett.* **107**, 240501 (2011).
- [17] X. Y. Jin, A. Kamal, A. P. Sears, T. Gudmundsen, D. Hover, J. Miloshi, R. Slattery, F. Yan, J. Yoder, T. P. Orlando and S. Gustavsson, "Thermal and residual excited-state population in a 3D transmon qubit", *Phys. Rev. Lett.*, **114**, 24 (2015).
- [18] V. B. Braginsky, Y. I. Vorontsov and K. S. Thorne, "Quantum nondemolition measurements", *Science*, **209**, 4456 (1980).

- [19] H. Paik, A. Mezzacapo, M. Sandberg, D. T. McClure, B. Abdo, A. D. Córcoles, O. Dial, D. F. Bogorin, B. Plourde, M. Steffen and A. W. Cross, “Experimental demonstration of a resonator-induced phase gate in a multiqubit circuit-qed system”, *Phys. Rev. Lett.*, **117**, 25 (2016).
- [20] E. T. Jaynes and F. W. Cummings, “Comparison of quantum and semiclassical radiation theories with application to the beam maser”, *Proceedings of the IEEE*, **51**, 1 (1963).
- [21] D. A. Steck, *Quantum and Atom Optics*, revision 0.12.0 (2017). <http://steck.us/teaching>.
- [22] L. S. Bishop, *Circuit Quantum Electrodynamics*. PhD dissertation (Yale University, 2010).
- [23] E. K. Irish, “Generalized rotating-wave approximation for arbitrarily large coupling”, *Phys. Rev. Lett.*, **99**, 17 (2007).
- [24] I. I. Rabi, “Space quantization in a gyrating magnetic field”, *Phys. Rev.*, **51** 8 (1937).
- [25] J. Fuchs, *Affine Lie algebras and quantum groups: An Introduction, with applications in conformal field theory*. Cambridge university press (1995).
- [26] B. Suri, *Transmon Qubits Coupled to Superconducting Lumped Element Resonators*. PhD dissertation (University of Maryland, 2015).
- [27] M. H. Devoret and R. J. Schoelkopf, “Superconducting circuits for quantum information: an outlook”, *Science*, **339** 6124 (2013).
- [28] W. D. Oliver and P. B. Welander, “Materials in superconducting quantum bits”, *MRS bulletin*, **38**, 10 (2013).
- [29] E. M. Purcell, H. C. Torrey and R. V. Pound, “Resonance absorption by nuclear magnetic moments in a solid”, *Phys. Rev.*, **69**, 1-2 (1946).
- [30] H. Paik and K. D. Osborn, “Reducing quantum-regime dielectric loss of silicon nitride for superconducting quantum circuits”, *Appl. Phys. Lett.*, **96**, 7 (2010).

- [31] J. M. Martinis, M. Ansmann and J. Aumentado, “Energy decay in superconducting Josephson-junction qubits from nonequilibrium quasiparticle excitations”, *Phys. Rev. Lett.*, 103, 9 (2009).
- [32] R. J. Schoelkopf, A. A. Clerk, S. M. Girvin, K. W. Lehnert and M. H. Devoret, “Quantum noise in mesoscopic physics”, *NATO Science Series in Mathematics* (2003).
- [33] A. A. Houck, J. A. Schreier, B. R. Johnson, J. M. Chow, J. Koch, J. M. Gambetta, D. I. Schuster, L. Frunzio, M. H. Devoret, S. M. Girvin and R. J. Schoelkopf, “Controlling the spontaneous emission of a superconducting transmon qubit”, *Phys. Rev. Lett.*, **101**, 8 (2008).
- [34] D. Esteve, M. H. Devoret and J. M. Martinis, “Effect of an arbitrary dissipative circuit on the quantum energy levels and tunneling of a Josephson junction”, *Phys. Rev. B*, **34**, 1 (1986).
- [35] P. Dirac, *The quantum theory of the emission and absorption of radiation. Proceedings of the Royal Society of London. Series A, Containing Papers of a Mathematical and Physical Character*, 114, 76 (1927).
- [36] E. A. Sete, J. M. Martinis and A. N. Korotkov, “Quantum theory of a bandpass Purcell filter for qubit readout”, *Phys. Rev. A*, **92**, 1 (2015).
- [37] J. M. Martinis, K. B. Cooper, R. McDermott, M. Steffen, M. Ansmann, K. D. Osborn, K. Cicak, S. Oh, D. P. Pappas, R. W. Simmonds and C. Y. Clare, “Decoherence in Josephson qubits from dielectric loss”, *Phys. Rev. Lett*, **95**, 21 (2005).
- [38] D. P. Pappas, M. R. Vissers, D. S. Wisbey, J. S. Kline and J. Gao, “Two level system loss in superconducting microwave resonators”, *IEEE Transactions on Applied Superconductivity*, **21**, 3 (2011).
- [39] S. Gustavsson, F. Yan, G. Catelani, J. Bylander, A. Kamal, J. Birenbaum, D. Hover, D. Rosenberg, G. Samach, A. P. Sears and S. J. Weber, “Suppressing relaxation in superconducting qubits by quasiparticle pumping”, *Science*, **354**, 6319 (2016).

- [40] Y. Y. Chen, P. Zhang, W. Zheng, Z. Wu and H. Zhai, “Many-body echo”, *Phys. Rev. A* **102**, 1 (2020).
- [41] G. Catelani, J. Koch, L. Frunzio, R. J. Schoelkopf, M. H. Devoret and L. I. Glazman, “Quasiparticle relaxation of superconducting qubits in the presence of flux”, *Phys. Rev. Lett*, **106**, 7 (2011).
- [42] C. Wang, Y. Y. Gao, I. M. Pop, U. Vool, C. Axline, T. Brecht, R. W. Heeres, L. Frunzio, M. H. Devoret, G. Catelani and L. I. Glazman, “Measurement and control of quasiparticle dynamics in a superconducting qubit”, *Nature communications*, **5**, 1 (2014).
- [43] D. Rogovin and D. J. Scalapino, “Fluctuation phenomena in tunnel junctions”, *A. of Phys.*, **88**, 1 (1974).
- [44] A. P. Sears, *Extending coherence in superconducting qubits: from microseconds to milliseconds*. PhD dissertation (Yale University, 2013).
- [46] D. J. Van Harlingen, T. L. Robertson, B. L. T. Plourde, P. A. Reichardt, T. A. Crane and J. Clarke, “Decoherence in Josephson-junction qubits due to critical-current fluctuations”, *Phys. Rev. B* **70**, 6 (2004).
- [47] R. P. Budoyo, *Effects of Optical Illumination on Superconducting Quantum Devices*, PhD dissertation (University of Maryland, 2015).
- [47] M. J. Reagor, *Superconducting Cavities for Circuit Quantum Electrodynamics*. PhD dissertation (Yale University, 2015).
- [48] A. A. Clerk and D. W. Utami, “Using a qubit to measure photon-number statistics of a driven thermal oscillator”, *Phys. Rev. A* **75**, 4 (2007).
- [49] R. R. Ernst, "Principles of Nuclear Magnetic Resonance in One and Two Dimensions", *Clarendon* (1990)

[50] E. L. Hahn, "Spin Echoes", *Phys. Rev.*, **80**, 580 (1950).

Chapter 3

[1] J. Bardeen, L. N. Cooper, and J. R. Schrieffer, "Microscopic theory of superconductivity," *Phys. Rev.*, **106**, 162 (1957).

[2] J. Bardeen, L. N. Cooper, and J. R. Schrieffer, "Theory of superconductivity," *Phys. Rev.*, **108**, 1175 (1957).

[3] L. N. Cooper, "Bound electron pairs in a degenerate Fermi gas," *Phys. Rev.*, **104**, 1189 (1956).

[4] M. Tinkham, *Introduction to Superconductivity, 2nd Edition*, McGraw Hill, New York, (1996).

[5] N. N. Bogoliubov, "A new method in the theory of superconductivity. i," *Sov. Phys. JETP*, **34** (1958).

[6] V. L. Ginzburg, "On superconductivity and superfluidity as well as on the physical minimum at the beginning of the 21st century," *ChemPhysChem*, **5**, 930 (2004).

[7] V. L. Ginzburg and L. D. Landau, "On the theory of superconductivity," *Sov. Phys. JETP*, **20**, 1064 (1950).

[8] R. W. Cohen and B. Abeles, "Superconductivity in Granular Aluminum Films", *Phys. Rev.*, **168**, 444 (1968).

[9] M. Strongin, R. S. Thompson, O. F. Kammerer, and J. E. Crow, "Destruction of Superconductivity in Disordered Near-Monolayer Films", *Phys. Rev. B*, **1**, 1078 (1970).

[10] C. C. Chi and J. Clarke, "Enhancement of the energy gap in superconducting aluminum by tunneling extraction of quasiparticles", *Phys. Rev. B*, **20**, 4465 (1979).

[7] C. T. Black, D. C. Ralph, and M. Tinkham, "Spectroscopy of the Superconducting Gap in Individual Nanometer-Scale Aluminum Particles", *Phys. Rev. Lett.*, **76**, 688 (1996).

[8] N. A. Court, A. J. Ferguson, and R. G. Clark, "Energy gap measurement of nanostructured aluminium thin films for single Cooper-pair device", *Supercond. Sci. Technol.*, **21**, 015013 (2008).

Chapter 4

[1] J. Bardeen, L. N. Cooper, and J. R. Schrieffer, "Microscopic theory of superconductivity", *Phys. Rev.*, **106**, 162 (1957).

[2] J. Bardeen, L. N. Cooper, and J. R. Schrieffer, "Theory of superconductivity," *Phys. Rev.*, **108**, 1175 (1957).

[3] L. N. Cooper, "Bound electron pairs in a degenerate fermi gas", *Phys. Rev.*, **104**, 1189 (1956).

[4] M. Tinkham, *Introduction to Superconductivity, 2nd Edition*, McGraw Hill, New York, (1996).

[5] C. S. Owen and D. J. Scalapino, "Superconducting state under the influence of external dynamic pair breaking", *Phys. Rev. Lett.*, **28**, 24 (1972).

[6] J. Aumentado, M. W. Keller, J. M. Martinis, and M. H. Devoret, "Nonequilibrium Quasiparticles and $2e$ Periodicity in Single-Cooper-Pair Transistors", *Phys. Rev. Lett.*, **92**, 066802 (2004).

[7] J. M. Martinis, M. Ansmann, and J. Aumentado, "Energy Decay in Superconducting Josephson-Junction Qubits from Nonequilibrium Quasiparticle Excitations", *Phys. Rev. Lett.*, **103**, 097002 (2009).

- [8] R. Barends, J. Wenner, M. Lenander, Y. Chen, R. C. Bialczak, J. Kelly, E. Lucero, P. O'Malley, M. Mariantoni, D. Sank, H. Wang, T. C. White, Y. Yin, J. Zhao, A. N. Cleland, J. M. Martinis, and J. J. A. Baselmans, "Minimizing quasiparticle generation from stray infrared light in superconducting quantum circuits", *Appl. Phys. Lett.*, **99**, 113507 (2011).
- [9] M. Bal, M. H. Ansari, J.-L. Orgiazzi, R. M. Lutchyn, and A. Lupascu, "Dynamics of parametric fluctuations induced by quasiparticle tunneling in superconducting flux qubits", *Phys. Rev. B*, **91**, 195434 (2015).
- [10] R. Barends, J. Wenner, M. Lenander, Y. Chen, R. C. Bialczak, J. Kelly, E. Lucero, P. O'Malley, M. Mariantoni, D. Sank and H. Wang, "Minimizing quasiparticle generation from stray infrared light in superconducting quantum circuits", *Appl. Phys. Lett.*, **99**, 11 (2011).
- [11] S. Krinner, S. Storz, P. Kurpiers, P., Magnard, J. Heinsoo, R. Keller, J. Luetolf, C. Eichler and A. Wallraff, "Engineering cryogenic setups for 100-qubit scale superconducting circuit systems", *EPJ Quantum Technology*, **6**, 1 (2019).
- [12] B. G. Christensen, C. D. Wilen, A. Opremcak, J. Nelson, F. Schlenker, C. H. Zimonick, L. Faoro, L. B. Ioffe, Y. J. Rosen, J. L. DuBois and B. L. T. Plourde, "Anomalous charge noise in superconducting qubits", *Phys. Rev. B*, **100**, 14(2019).
- [13] J. Gao, J. Zmuidzinas, A. Vayonakis, P. Day, B. Mazin and H. Leduc, "Equivalence of the effects on the complex conductivity of superconductor due to temperature change and external pair breaking", *J. of Low Temp. Phys.*, **151**, 1-2 (2008).
- [14] C. S. Owen and D. J. Scalapino, "Superconducting state under the influence of external dynamic pair breaking", *Phys. Rev. Lett.*, **28**, 24 (1972).
- [15] W. H. Parker, "Modified heating theory of nonequilibrium superconductors", *Phys. Rev. B*, **12**, 9 (1975).

- [16] R. Zhang, *Loss in superconducting quantum device from non-equilibrium quasiparticles and inhomogeneity in energy gap*, PhD dissertation (University of Maryland, 2020).
- [17] T. Yamamoto, Y. Nakamura, Y. A. Pashkin, O. Astafiev and J. S. Tsai, “Parity effect in superconducting aluminum single electron transistors with spatial gap profile controlled by film thickness”, *Appl. Phys. Lett.*, **88**, 21 (2006).
- [18] A. J. Ferguson, F. E. Hudson and R. G. Clark, “Microsecond resolution of quasiparticle tunneling in the single-Cooper-pair transistor”, *Phys. Rev. Lett.*, **97**, 10 (2006).
- [19] B. S. Palmer, C. A. Sanchez, A. Naik, M. A. Manheimer, J. F. Schneiderman, P. M. Echternach and F. C. Wellstood, “Steady-state thermodynamics of nonequilibrium quasiparticles in a Cooper-pair box”, *Phys. Rev. B*, **76**, 5 (2007).
- [20] J. Koch, T. M. Yu, J. Gambetta, A. A. Houck, D. I. Schuster, J. Majer, A. Blais, M. H. Devoret, S. M. Girvin, and R. J. Schoelkopf, "Charge-insensitive qubit design derived from the Cooper pair box", *Phys. Rev. A*, **76**, 042319 (2007).
- [21] R. J. Schoelkopf, A. A. Clerk, S. M. Girvin, K. W. Lehnert, and M. H. Devoret, “Quantum noise in mesoscopic physics”, *NATO Science Series in Mathematics* (2003).
- [22] D. Rogovin and D. J. Scalapino, “Fluctuation phenomena in tunnel junctions”, *Ann. of Phys.*, **86**, 1 (1974).
- [23] T. A. Fulton and G. J. Dolan, “Observation of single-electron charging effects in small tunnel junctions”, *Phys. Rev. Lett.*, **59**, 1 (1987).
- [24] R. W. Cohen and B. Abeles, “Superconductivity in granular aluminum films”, *Phys. Rev.*, **168**, 2 (1968).
- [25] M. Strongin, R. S. Thompson, O. F. Kammerer and J. E. Crow, “Destruction of superconductivity in disordered near-monolayer films”, *Phys. Rev. B*, **1**, 3 (1970).

- [26] C. C. Chi and J. Clarke, "Enhancement of the energy gap in superconducting aluminum by tunneling extraction of quasiparticles", *Phys. Rev. B*, **20**, 11 (1979).
- [27] C. T. Black, D. C. Ralph and M. Tinkham, "Spectroscopy of the superconducting gap in individual nanometer-scale aluminum particles", *Phys. Rev. Lett.*, **76**, 4 (1996).
- [28] C. S. Owen and D. J. Scalapino "Superconducting state under the influence of external dynamic pair breaking", *Phys. Rev. Lett.*, **28**, 24 (1972).
- [29] J. M. Martinis, K. B. Cooper, R. McDermott, M. Steffen, M. Ansmann, K. D. Osborn, K. Cicak, S. Oh, D. P. Pappas, R. W. Simmonds and C. Y. Clare, "Decoherence in Josephson qubits from dielectric loss", *Phys. Rev. Lett.*, **95**, 21(2005).
- [30] H. Paik and K. D. Osborn, "Reducing quantum-regime dielectric loss of silicon nitride for superconducting quantum circuits", *Appl. Phys. Lett.*, **96**, 7 (2010).
- [31] D. P. Pappas, M. R. Vissers, D. S. Wisbey, J. S. Kline and J. Gao, "Two level system loss in superconducting microwave resonators", *IEEE Trans. on Appl. Superc.*, **21**, 3 (2011).
- [32] A. Andreev, "The thermal conductivity of the intermediate state in superconductors," *Sov. Phys. JETP* **19**, 1228 (1964).
- [33] G. E. Blonder, M. Tinkham, and T. M. Klapwijk, "Transition from metallic to tunneling regimes in superconducting microconstrictions: Excess current, charge imbalance, and supercurrent conversion," *Phys. Rev. B*, **25**, 4515 (1982).
- [34] D. Averin and A. Bardas, "ac Josephson effect in a single quantum channel," *Phys. Rev. Lett.*, **75**, 1831 (1995).
- [35] E. Bratus, V. Shumeiko, and G. Wendin, "Theory of subharmonic gap structure in superconducting mesoscopic tunnel contacts," *Phys. Rev. Lett.*, **74**, 2110 (1995).

- [36] J. Cuevas, A. Martin-Rodero, and A. L. Yeyati, "Hamiltonian approach to the transport properties of superconducting quantum point contacts," *Phys. Rev. B*, **54**, 7366 (1996).
- [37] G. B. Arnold, "Superconducting tunneling without the tunneling Hamiltonian. ii. Subgap harmonic structure," *J. of Low Temp. Phys.* **68**, 1 (1987).
- [38] W.Liao, *Investigation of tunneling in superconductors using a millikelvin scanning tunneling microscope*, PhD dissertation (University of Maryland, 2019).

Chapter 5

- [1] H. Paik, D. I. Schuster, L. S. Bishop, G. Kirchmair, G. Catelani, A. P. Sears, B. R. Johnson, M. J. Reagor, L. Frunzio, L. I. Glazman, S. M. Girvin, M. H. Devoret, and R. J. Schoelkopf, "Observation of high coherence in Josephson junction qubits measured in a three-dimensional circuit QED architecture", *Phys. Rev. Lett.* **107**, 240501 (2011).
- [2] A. P. Place, L. V. Rodgers, P. Mundada, B. M. Smitham, M. Fitzpatrick, Z. Leng and A. A. Houck, "New material platform for superconducting transmon qubits with coherence times exceeding 0.3 milliseconds". *Nature communications*, **12**, 1779 (2021).
- [3] I. M. Pop, K. Geerlings, G. Catelani, R. J. Schoelkopf, L. I. Glazman and M. H. Devoret, "Coherent suppression of electromagnetic dissipation due to superconducting quasiparticles." *Nature*, **508**, 7496 (2014).
- [4] V. B. Braginsky, Y. I. Vorontsov and K. S. Thorne, "Quantum nondemolition measurements.", *Science*, **209**, 4456 (1980).
- [5] E. M. Purcell, H. C. Torrey and R. V. Pound, "Resonance absorption by nuclear magnetic moments in a solid", *Phys. Rev.*, **69**, 1-2 (1946).

- [6] G. J. Dolan(1977-09-01). "Offset masks for lift-off photo processing". *Appl. Phys. Lett.*, **31**, 5 (1977).
- [7] C. Ballard, *Variable qubit-qubit coupling via a tunable lumped-element resonator*, PhD dissertation (University of Maryland, 2018).
- [8] M. J. Reagor, *Superconducting Cavities for Circuit Quantum Electrodynamics*. PhD dissertation (Yale University, 2015).
- [9] EZ Form, Non-Magnetic Connectors SubMiniature version A (SMA) feedthrough connectors, <https://www.ezform.com/docs/Non-Mag.pdf>.
- [10] http://headwayresearch.com/chucks/ec_chucks.htm
- [11] <http://microchem.com/pdf/PMGI-Resists-data-sheetV-rhcredit-102206.pdf>
- [12] http://microchem.com/pdf/PMMA_Data_Sheet.pdf
- [13] <http://cmnst.ncku.edu.tw/ezfiles/23/1023/img/127/s1800seriesDataSheet.pdf>
- [14] http://www.nanophys.kth.se/nanophys/facilities/dicingsaw/Dicing_Saw_Manual.pdf
- [15] https://www.mchemical.co.jp/en/products/departments/mcc/specialtychem/product/1201151_7976.html
- [16] <https://www.raith.com/products/eline-plus.html>
- [17] http://microchem.com/products/images/uploads/MF_CD_26_Data_Sheet.pdf
- [18] <https://rdmathis.com/product/micro-electronic-sources-25/>
- [19] http://assets.fluke.com/manuals/8xiii_sieng0200.pdf
- [20] <https://www.digikey.com/catalog/en/partgroup/963e/20357>
- [21] M. Strongin, R. S. Thompson, O. F. Kammerer, and J. E. Crow, "Destruction of Superconductivity in Disordered Near-Monolayer Films", *Phys. Rev. B*, **1**, 1078 (1970).

- [22] C. C. Chi and J. Clarke, “Enhancement of the energy gap in superconducting aluminum by tunneling extraction of quasiparticles”, *Phys. Rev. B*, **20**, 4465 (1979).
- [23] C. T. Black, D. C. Ralph, and M. Tinkham, “Spectroscopy of the Superconducting Gap in Individual Nanometer-Scale Aluminum Particles”, *Phys. Rev. Lett.*, **76**, 688 (1996).
- [24] N. A. Court, A. J. Ferguson, and R. G. Clark, “Energy gap measurement of nanostructured aluminium thin films for single Cooper-pair device”, *Supercond. Sci. Technol.* **21**, 015013 (2008).

Chapter 6

- [1] <https://nanoscience.oxinst.com/products/cryofree-dilution-refrigerators/triton>
- [2] T. O. Klaassen et al., *IEEE Tenth Ann. Int. Conf. on Ter. Elec.* 7503105 (2002).
- [3] <http://www.microstock-inc.com/products.htm>
- [4] <http://xmacorp.com/pages/cryo>
- [5] <http://www.klmicrowave.com/>
- [6] https://wiki.kip.uni-heidelberg.de/KIPwiki/images/c/cb/PAMTECH_cryogenic_isolators.pdf
- [7] <http://www.caltechmicrowave.org/amplifiers>
- [8] <https://www.part2go.com/rf-microwave/directional-hybrid-couplers/6-to-12ghz/mac-c3205-06-microwave-rf-directional-coupler-4-8-ghz-06db-couplingtested.html>
- [9] <https://nardamiteq.com/viewmodel.php?model=AMF-3F-04000800-07-10P>
- [10] R. P. Budoyo, *Effects of Optical Illumination on Superconducting Quantum Devices*, PhD dissertation (University of Maryland, 2015).

- [11] A. J. Przybysz, *Reducing decoherence in dc SQUID phase qubits*. PhD dissertation (University of Maryland, 2010).
- [12] Keysight Technologies (formerly Agilent), www.keysight.com.
- [13] Stanford Research Systems, www.thinksrs.com.
- [14] D. C. Noll et al., *IEEE Trans. on Med. Imag.* **10**, 2 (1991).
- [15] National Instruments, www.ni.com.
- [16] S. Novikov, *Raman coherence effects in a superconducting Jaynes-Cummings system*, PhD thesis (University of Maryland, College Park, MD, 2015).

Chapter 7

- [1] <https://www.keysight.com/en/pdx-x202237-pn-E8257D/psg-analog-signalgenerator-100-khz-to-67-ghz?cc=US&lc=eng>
- [2] L. S. Bishop, *Circuit Quantum Electrodynamics*. PhD dissertation (Yale University, 2010).
- [3] I. I. Rabi, “Space quantization in a gyrating magnetic field.”, *Phys. Rev.*, **51**, 8 (1937).
- [4] P. Meystre and M. Sargent III, *Elements of Quantum Optics, 3rd ed.*, SpringerVerlag Berlin Heidelberg (1999).
- [5] B. Suri, *Transmon Qubits Coupled to Superconducting Lumped Element Resonators*, PhD dissertation (University of Maryland, 2015).
- [6] N. F. Ramsey, “A molecular beam resonance method with separated oscillating fields.”, *Phys. Rev.*, **78**, 6 (1950).
- [7] A. Abragam, *Principles of Nuclear Magnetism*, A Clarendon Press Publication, Oxford University Press, (1983).

Chapter 8

- [1] M. D. Reed, L. DiCarlo, B. R. Johnson, L. Sun, D. I. Schuster, L. Frunzio and R. J. Schoelkopf, “High-fidelity readout in circuit quantum electrodynamics using the Jaynes-Cummings nonlinearity”, *Phys. Rev. Lett.*, **105**, 17 (2010).
- [2] K. Li, S. K. Dutta, Z. Steffen, D. Poppert, S. Keshvari, J. Bowser, B. S. Palmer, C. J. Lobb and F. C. Wellstood, “Long-lived transmons with different electrode layouts,” *MRS Advances*, **7**, 13-14 (2022).
- [3] L. Grünhaupt, N. Maleeva, S. T. Skacel, M. Calvo, F. Levy-Bertrand, A. V. Ustinov and I. M. Pop, “Loss mechanisms and quasiparticle dynamics in superconducting microwave resonators made of thin-film granular aluminum.” *Phys. Rev. Lett.*, **121**, 11 (2018).

Chapter 9

- [1] <https://arxiv.org/pdf/2304.13257.pdf>
- [2] Kim, C. E., Ray, K. G., & Lordi, V. (2020). A density-functional theory study of the Al/AlOx/Al tunnel junction. *Journal of applied physics*, 128(15).
- [3] K. Li, S. K. Dutta, Z. Steffen, B. S. Palmer, C. J. Lobb and F. C. Wellstood, “Power-Law scaling of relaxation time fluctuations in transmon qubits”, *IEEE Trans. on Appl. Superc.*, **33**, 5 (2023).